Fast Methods for Inverse Wave Scattering Problems

by

Jung Hoon Lee

B.S. in Electrical Engineering
Korea Advanced Institute of Science and Technology, Republic of Korea, 1999
M.S. in High Performance Computation for Engineered Systems
National University of Singapore, Singapore, 2001
M.S. in Electrical Engineering and Computer Science
Korea Advanced Institute of Science and Technology, Republic of Korea, 2002

Submitted to the Department of Electrical Engineering and Computer Science
in partial fulfillment of the requirements for the degree of

Doctor of Philosophy in Electrical Engineering and Computer Science

at the

MASSACHUSETTS INSTITUTE OF TECHNOLOGY

September 2008

Author .....
Department of Electrical Engineering and Computer Science
June 16, 2008

Certified by .....
Jacob White
Professor
Thesis Supervisor

Accepted by .....
Terry P. Orlando
Chair, Department Committee on Graduate Students

Fast Methods for Inverse Wave Scattering Problems

by

Jung Hoon Lee

Submitted to the Department of Electrical Engineering and Computer Science
on June 16, 2008, in partial fulfillment of the
requirements for the degree of
Doctor of Philosophy in Electrical Engineering and Computer Science

Abstract

Inverse wave scattering problems arise in many applications including computerized/diffraction tomography, seismology, diffraction/holographic grating design, object identification from radar singals, and semiconductor quality control. Efficient algorithms exist for some inverse wave scattering problems in the low- and high-frequency regime or with weak scatterers. However, inverse wave scattering problems in the resonance regime with strong scatterers still pose many challenges.

This thesis proposes algorithms for inverse wave scattering problems in the resonance regime with strong scatterers. These problems are part of, for instance, grating design, object identification, and semiconductor quality control. The proposed methods are (a) a spectrally convergent Nyström method for periodic structures in 2-D; (b) a fast Jacobian approximation method accompanying a Nyström method; (c) a fast and accurate method for evaluating the potential integrals in the 3-D mixed-potential integral operator with the Rao-Wilton-Glisson basis function; and (d) optimization with parameterized reduced-order models. The Nyström method and the method to evaluate the potential integrals accelerate scattered field evaluations by solving integral equations efficiently. The Jacobian approximation method and optimization with parameterized reduced-order models efficiently couple algorithms to evaluate scattered fields due to a guess of the scatterer and optimization methods to improve the guess.

The Nyström and the Jacobian approximation methods are used to identify the parameters characterizing a periodic dielectric grating in 2-D. The method to evaluate the potential integrals and optimization with parameterized reduced-order models are applied to the problem of identifying simple discrete geometries in 3-D.

Thesis Supervisor: Jacob White
Title: Professor

Acknowledgments

When I entered graduate school in 1999, a senior student in my group told me that my time as a graduate student was well-spent if I had one of the followings: (a) an adviser I personally liked; (b) thesis topic I enjoyed; and (c) friends I liked to work with. Looking back, I had the rare luck of having all three.

I met my adviser, Professor Jacob White, in Singapore in 2000, and I became quickly captivated by his personality and passion to teach and learn. I would not be who I am, personally and professionally, without his help. I would like to thank Professor Luca Daniel and Professor Pablo Parrilo for their generous time, advice, and help while I was working on this thesis. Generous funding by KFAS (Korea Foundation for Advanced Studies), Singapore-MIT Alliance, MARCO/IFC, and DARPA gave me an opportunity to enjoy this field of research, which I will persue for the years to come.

At MIT, I have met great people and enjoyed working with them. Chadwick Collins who runs our offices has always been a great help. Working with Zung-Sun Choi and Professor Carl Thompson on electromigration was a fun and rewarding experience. I have learned about integral equations and fast solvers while interacting with Zhenhai Zhu, David Willis, Jaydeep Bardhan, Shihhsien Kuo, Carlos Pinto Coelho, Homer Reid, Lei Zhang, and Tarek Moselhy. Professor Luca Daniel, Dmitry Vasilyev, Kin Sou, Bradly Bond, and Tarek Moselhy helped me understand model order reduction; and Professor Pablo Parrilo, Kin Sou, Almir Mutapcic, and Professor Stephen Boyd gave me help on optimization. James Geraci, Carlos Pinto Coelho, Homer Reid, and Steve Leibman taught me proper programming, and I enjoyed coding with them. Finally, Professor Jae S. Lim and my mentor Dr. Yehuda Avniel gave me invaluable advice on what Ph.D. is and how to manage work and, more importantly, life.

When I was leaving for MIT, my mentor at KAIST told me that I should try to enjoy every moment of my life even though it might seem difficult. It would have been impossible to do so without the help of my friends. Seongwhan Cho practically took care of me when I first came to MIT, and Xin Hu and Anne Vithayathil taught me many things about life in the United States. Jae Jeen Choi, Euiheon Chung, Seongmoo Heo, Seung-Hun Jeon, Chulmin Joo, Jungwon Kim, Yoon-Jung Kim, Jaewook Lee, Daehyun Lim, Min Park, and Chanryeol Rhyou are like older brothers and sister to me; I will cherish the time we spent

together and the chat we had (about science, engineering, Ph.D., marriage, and life in general) over a cup of coffee. I had a great time with many people including those whom I met at Sidney and Pacific. Some of them gave me a life other than research, and others were great sources of information and inspiration. I would like to thank Jihwan Choi, Hyemin Chung, Jerin Gu, Tairin Hahn, Kuk-Hyun Han, Sangmok Han, Eun-Jong Hong, Jungwoo Joh, Sunhyung Kang, Adlar Kim, Bo Kim, Boguk Kim, Byungsub Kim, Jinkuk Kim, Woo Sik Kim, Yongwook Kim, Choonghyun Lee, Dongkun Lee, Jung Eun Lee, Sang-il Lee, Youjin Lee, Jungkeun Lim, Laura Proctor, Surapap Rayanakorn, Kyungbum Ryu, Gookwon Suh, and many others.

Ever since I can remember, I have had a chronic skin problem; life at MIT would have been even more stressful without the help of people at the MIT medical. I would like to thank Karen Ayoub, Dr. Davis Farvolden, Judy Leonard, Dr. Debby Lin, Barbara Starr, and Deb Tiernan for patiently treating me for the last seven years. Thanks to them, I can now enjoy the beach at Cape Cod.

Finally, my deepest love goes to my family: grandmother, father, mother, parents-in-law, and my little brothers and sisters back in South Korea and my lovely wife Seha Kim with whom I made may happy memories at MIT. They have been patiently waiting for me to find my own way and have given me unconditional love and support throughout. This thesis would not exist without their help. Thank you so much, and I love you!

Contents

List of Figures

Chapter 1

Introduction

1.1 Motivation

In an inverse wave scattering problem, an unknown scatterer is identified by measuring the scattered field. Inverse wave scattering problems arise in many applications including image reconstruction from x-ray and ultrasonic measurements [1, 2, 3, 4, 5, 6], seismic analysis for geophysics and oil-field exploration [7, 8, 9, 10, 11, 12, 13], object identification in addition to its location and velocity from radar signals [14, 15]. An inverse wave scattering problem is also a part of a widely used quality control method for semiconductor fabrication [16, 17, 18, 19, 20, 21, 22, 23].

The difficulty of an inverse wave scattering problem strongly depends on the relative size of the scatterer to the source wavelength [3, 5, 24]. For high-frequency problems where the source wavelength is much shorter than the size of the scatterer, the wave propagates mostly in a straight line, and geometrical optics and acoustics approximations are possible [3, 25]. Such an approximation leads to efficient solution methods based on the Fourier slice theorem, and they are widely used in computerized tomography [5, 6]. Low-frequency problems, where the source wavelength is much longer than the size of the scatterer, become inverse diffusion problems [3, 25]. These problems are not easy since they are highly ill-posed. Nevertheless, efficient methods exist [3, 26]. Furthermore, solvers to analyze diffusion problems are easier to develop and more efficient than those to analyze wave problems [27, 28, 29, 30, 31], making it easier to couple the solvers to an optimization algorithm and solve an inverse diffusion problem.

The difficulty of inverse wave scattering problems also depends on the type of the scat-

terer. If the wavelength is comparable to the size of the scatterer, the problem is in the resonance regime. Inverse wave scattering problems in the resonance regime is known to be difficult since diffraction of waves can no longer be ignored. But, the Born or Rytov approximation is possible for certain scatterers [2, 4, 5]; such approximations lead to problems similar to high-frequency problems, and efficient algorithms based on the Fourier diffraction theorem exist [2, 3, 4, 5].

Unfortunately, many inverse wave scattering problems are not high or low in frequency, nor is it possible to apply the Born or Rytov approximation. Higher frequency, or shorter wavelength, sources are almost always preferred to lower frequency ones since they provide higher resolution [5, 6]. But, the choice of source may be limited by other considerations. For instance, a higher frequency source may not be available when the quality of the source deteriorates in high frequencies [32, 33], or it has adverse effect to the scatterer, such as x-rays in medical applications [5].

Inverse wave scattering problems in the resonance regime are interesting as there are many applications in semiconductor quality control [16, 17, 18, 19, 20, 21, 22, 23], designing gratings for spectral analysis [34, 35, 36], and object identification from radar signals [14, 15]. These problems are solved iteratively in many cases by combining two parts [37, 38, 39]: the forward analysis that evaluates the scattered fields due to the source and a guess of the scatterer, and the inverse analysis that improves the guess. Hence, a guess of the scatterer is iteratively improved until the computed scattered field due to the guess matches the measured field.

The inverse wave scattering problem in the resonance regime is challenging in many ways. First, a highly efficient forward algorithm suitable for repeated evaluation is difficult to develop. Analytic solutions for wave scattering problems exist only for simple scatterers [40] such as spheres, ellipsoids, and infinitely long cylinders. Numerical methods have to be employed for scatterers of practical interest [41, 42, 43, 44, 45, 46] and can be computationally expensive. A single forward analysis may take from minutes to days for large and complicated 3-D structures.

The optimization problem corresponding to the inverse analysis is non-convex and ill-posed in most cases. If an optimization problem is non-convex, finding a global minimum is practically impossible, and a local optimization algorithm may perform poorly [47, 48]. Even worse, the optimization problem is ill-posed: a small change in data can lead to a

large change in the solution [49, 50, 28]. Therefore, some form of prior information has to be incorporated to recover the solution in a reliable manner [49, 51, 52].

Finally, efficient coupling of the forward and inverse analyses poses challenges. Most efficient optimization algorithms require derivatives of the objective function (and the constraints) [47, 53, 54], but derivatives may be hard to evaluate if the forward analysis solves partial differential or integral equations numerically. Closed form formulae for the derivatives, in most cases, do not exist, and numerical approximations have to be made [55, 54, 56].

In this thesis, techniques to accelerate the forward analysis and to couple forward and inverse analyses efficiently are proposed, and they are applied to inverse electromagnetic wave scattering problems in the resonance regime. The contributions are (a) a spectrally convergent Nyström method for periodic structures in 2-D; (b) a fast Jacobian approximation method accompanying a Nyström method; (c) a novel method for evaluating the potential integrals in the 3-D mixed-potential integral operator with the Rao-Wilton-Glisson basis function; and (d) optimization with parameterized reduced-order models. The proposed Nyström and Jacobian approximation methods are used to identify parameters characterizing a periodic dielectric grating in 2-D. The proposed method for potential integrals and optimization with parameterized reduced-order models are used to identify some simple discrete geometries in 3-D.

1.2 Thesis Outline

In the next chapter, the necessary background for integral equations for dielectric scattering in 2-D and 3-D is presented. Other than the subsection on equivalence principles that tries to elucidate the connection between equivalence principles and underlying mathematical principles, the chapter is a summary of existing literature.

In chapter 3 and 4, methods for dielectric scattering in 2-D are described. In chapter 3, the existing spectrally convergent Nyström methods in 2-D are extended to periodic problems. By retaining the spectral convergence, only a small number of quadrature points are necessary for the forward analysis. The periodic extension works for continuously periodic structures, such as surface gratings, as well as discretely periodic structures, such as photonic crystals consisting of discrete pillars. The proposed method for continuously periodic structures separates additional singularities due to the periodic sources in the neighboring

periods and integrates the singularities with the proposed modified Fejér quadrature. In addition, the proposed method can analyze structures with periods much larger than the wavelength by evaluating the separated singularities in a numerically stable manner.

In chapter 4, a fast method to approximate the Jacobian for a shape optimization problem is proposed. The Jacobian is evaluated approximately using the properties of the underlying Nyström method and the chain rule. As a result, the cost of the Jacobian approximation is directly proportional to the number of quadrature points and independent to the number of optimization variables under certain assumptions. Combined with a spectrally convergent Nyström method, the cost of the Jacobian approximation is kept small even for problems with many optimization variables.

Nyström methods are hard to generalize to problems in 3-D, and projection methods, such as collocation and Galerkin methods, are popular alternatives. Unfortunately, projection methods for surface integral equations have their own shortcomings, and the next two chapters address some of them.

Chapter 5 presents a novel method to evaluate the potential integrals in the 3-D mixed-potential integral operator if the Rao-Wilton-Glisson basis function is used to approximate the surface currents. These potential integrals are difficult to evaluate since the 3-D Green's function is singular. The proposed method first turns the area integral over a flat triangular panel into line integrals over the panel edges using Gauss' theorem. Then, faster convergence of the line integrals is achieved by a change of variable motivated by a complex-domain mapping. Therefore, the proposed method can evaluate nearby- and singular-potential integrals accurately and efficiently.

Projection methods tend to converge more slowly than Nyström methods, resulting in a larger system of linear equations to solve for each forward analysis. A method to decouple the forward and inverse analyses is proposed in chapter 6, which uses a parameterized reduced-order model as a proxy for the original forward analysis. The parameterized reduced-order model is algorithmically constructed by multiple forward analyses and the polynomial-fit parameterized moment matching before the inverse problem is solved. The resulting parameterized reduced-order model can be evaluated repeatedly for small computational cost and can replace the original model for small changes in the optimization variables. Furthermore, the Jacobian evaluation is trivial due to the structure of the reduced-order model. Some improvements to the polynomial-fit parameterized moment

matching are proposed for scattering problems, together with a graphical method to identify the moment matching condition for the projection matrix.

Finally, the contributions, their limitations, and possible improvements are summarized in chapter 7.

1.3 Summary of the Novel Contributions

A number of new contributions are made related to the Nyström method. The singularity separation for periodic Green's function in section 3.2 and the parameterization in section 3.3 are novel contributions to the literature. Even though many modified Clenshaw-Curtis and Fejér quadratures exist, the method proposed in section 3.4 for the logarithmic singularity has never been introduced up to the author's knowledge. The fast Jacobian evaluation method in section 4.3 is new, where the development of the method is inspired by the isoparametric approach for shape optimization problems [56].

Two improvements for evaluating potential integrals are proposed. One is the dimension reduction in section 5.3 to turn the surface integral over a flat triangular panel into line integrals over its edges, and the other is a change of variable in section 5.4 to improve the convergence of the resulting line integrals.

Finally, three methods are proposed to create a parameterized reduced-order model for dielectric scattering. First is the moment matching graph in section 6.3 to find the projection matrix for moment matching. The other two in section 6.4 approximate and transform the original dielectric scattering model such that the moment matching graph can be applied.

Chapter 2

Background in the Maxwell's Equations and Integral Formulations

This chapter summarizes the necessary background in Maxwell's equations and integral equations. The only novel contribution is the presentation of equivalence principles as interpretations to the underlying mathematical principles and their generalization to the Laplace and Helmholtz equations in subsection 2.2.2. The rest is mainly a summary of the existing literature on the Maxwell's equations and integral equations.

Section 2.1 shows the relation between the Maxwell's equations and the scalar Helmholtz equation. The Maxwell's equations are known to be difficult to solve, and decomposing them into scalar Helmholtz equations greatly simplifies the problem.

The solution to the scalar Helmholtz equations with the Sommerfeld radiation condition at infinity is shown in section 2.2. A source formulation with only equivalent charges is used for 2-D dielectric scattering analysis, resulting in a mixture of first-kind and second-kind integral equations. Even though second-kind integral equations are preferred for numerical reasons [57, 28], the disadvantage of the mixed first- and second-kind equations is compensated by a spectrally convergent Nyström method proposed in chapter 3.

Equivalence principles are commonly used in Electromagnetics to transform a problem with a piecewise homogeneous medium into equivalent problems with homogeneous media [58, 59, 25, 60]. Even though these principles are interpretations of some mathematical

properties of the governing Maxwell's equations and the associated boundary value problems, the connection is not well explained elsewhere except in [58] for one type of equivalence principles. In subsection 2.2.2, equivalence principles are grouped into two types depending on the underlying mathematical principle and generalized to the scalar Helmholtz equation. Similar interpretation and classification can be made for the Maxwell's equations and the Laplace equation using the mathematical properties in [61, 62, 27, 28].

Section 2.3 presents the 3-D mixed-potential integral operator as the solution to the Maxwell's equations with the Silver-Müller radiation condition at infinity. Then, the PM-CHW [59, 63, 64] formulation, consisting of only second-kind integral equations is presented for the 3-D dielectric scattering.

2.1 Simplifying the Maxwell's Equations

The Maxwell's equations in the most general form are known to be difficult to solve. Fortunately, there are special cases where the Maxwell's equations are simplified to scalar Helmholtz equations. In this section, two of the well-known cases are presented in detail: the 2-D Maxwell's equations and the mixed potential formulation for the 3-D Maxwell's equations. Other cases, such as the 1-D Maxwell's equations and Maxwell's equations in sourceless homogeneous medium, can be found in [65, 66, 67].

The main subject of the this section is the time-harmonic Maxwell's equations with angular frequency ω. Using the $e^{j\omega t}$ convention, for instance $\mathcal{E}(\mathbf{r},t) = \mathrm{Re}\{\mathbf{E}(\mathbf{r})e^{j\omega t}\}$, the time-harmonic Maxwell's equations are

$$\begin{aligned} \nabla \times \mathbf{E} &= -j\omega\mathbf{B} - \mathbf{M} \\ \nabla \times \mathbf{H} &= j\omega\mathbf{D} + \mathbf{J} \\ \nabla \cdot \mathbf{D} &= \rho_e \\ \nabla \cdot \mathbf{B} &= \rho_m \end{aligned} \tag{2.1}$$

with both the electric and (fictitious) magnetic currents $\mathbf{J}$ and $\mathbf{M}$, respectively; $\mathbf{E}$ and $\mathbf{H}$ are electric and magnetic fields, $\mathbf{D}$ and $\mathbf{B}$ are the electric and magnetic flux densities. The electric and (fictitious) magnetic charges, ρ_e and ρ_m respectively, are necessary to ensure

the conservation of charge given by

$$\begin{aligned} \nabla \cdot \mathbf{M} &= -j\omega\rho_m \\ \nabla \cdot \mathbf{J} &= -j\omega\rho_e. \end{aligned} \tag{2.2}$$

Note that the negative sign in front of $\mathbf{M}$ in (2.1) helps us to recover the conservation law. Introducing both the electric and (fictitious) magnetic currents makes all the equations independent, and the resulting symmetry in the equations enables duality arguments as shown in subsection 2.1.2.

2.1.1 The Maxwell's Equations in 2-D

If the medium and the sources are invariant in one direction, the problem is considered 2-D, and the invariant direction is denoted as the z direction in this thesis. The invariance in the z direction implies that the z-direction derivatives of all the quantities in the Maxwell's equations are zero. For instance,

$$\nabla \times \mathbf{E} = \begin{vmatrix} \hat{x} & \hat{y} & \hat{z} \\ \frac{\partial}{\partial x} & \frac{\partial}{\partial y} & 0 \\ E_x & E_y & E_z \end{vmatrix} = \frac{\partial E_z}{\partial y}\hat{x} - \frac{\partial E_z}{\partial x}\hat{y} + (\frac{\partial E_y}{\partial x} - \frac{\partial E_z}{\partial y})\hat{z}.$$

For a *homogeneous isotropic* medium with $\mathbf{D} = \epsilon\mathbf{E}$ and $\mathbf{B} = \mu\mathbf{H}$ for permittivity ϵ and permeability μ, (2.1) with (2.2) replacing the Gauss' laws simplifies to

$$\begin{aligned} \frac{\partial E_z}{\partial y} &= -j\omega\mu H_x - M_x \\ -\frac{\partial E_z}{\partial x} &= -j\omega\mu H_y - M_y \\ \frac{\partial E_y}{\partial x} - \frac{\partial E_x}{\partial y} &= -j\omega\mu H_z - M_z \\ \frac{\partial H_z}{\partial y} &= j\omega\epsilon E_x + J_x \\ -\frac{\partial H_z}{\partial x} &= j\omega\epsilon E_y + J_y \\ \frac{\partial H_y}{\partial x} - \frac{\partial H_x}{\partial y} &= j\omega\epsilon E_z + J_z \\ \frac{\partial M_x}{\partial x} + \frac{\partial M_y}{\partial y} &= -j\omega\rho_m \\ \frac{\partial J_x}{\partial x} + \frac{\partial J_y}{\partial y} &= -j\omega\rho_e \end{aligned}$$

These equations can be grouped into two completely decoupled sets of equations [65, 25]: one with E_z, H_y, and H_z fields,

$$\begin{aligned} \frac{\partial E_z}{\partial y} &= -j\omega\mu H_x - M_x \\ -\frac{\partial E_z}{\partial x} &= -j\omega\mu H_y - M_y \\ \frac{\partial H_y}{\partial x} - \frac{\partial H_x}{\partial y} &= j\omega\epsilon E_z + J_z \\ \frac{\partial M_x}{\partial x} + \frac{\partial M_y}{\partial y} &= -j\omega\rho_m, \end{aligned} \tag{2.3}$$

and the other with H_z, E_y, and E_z,

$$\begin{aligned} \frac{\partial H_z}{\partial y} &= j\omega\epsilon E_x + J_x \\ -\frac{\partial H_z}{\partial x} &= j\omega\epsilon E_y + J_y \\ \frac{\partial E_y}{\partial x} - \frac{\partial E_x}{\partial y} &= -j\omega\mu H_z - M_z \\ \frac{\partial J_x}{\partial x} + \frac{\partial J_y}{\partial y} &= -j\omega\rho_e. \end{aligned} \tag{2.4}$$

The set of equations (2.3) defines the E-polarization problem[1]. For the E-polarization problem, E_z is found by solving the scalar Helmholtz equation

$$\begin{aligned} \nabla^2 E_z + \omega^2\mu\epsilon E_z &= j\omega\mu J_z - \frac{\partial M_x}{\partial y} + \frac{\partial M_y}{\partial x} \\ \frac{\partial M_x}{\partial x} + \frac{\partial M_y}{\partial y} &= -j\omega\rho_m \end{aligned} \tag{2.5}$$

with a suitable boundary condition. Once E_z is found, the corresponding $\mathbf{H}$ is, or more precisely H_x and H_y are, evaluated from

$$\mathbf{H} = \frac{-1}{j\omega\mu}(\nabla \times (0, 0, E_z) + \mathbf{M}) \Leftrightarrow \begin{cases} H_x = \dfrac{-1}{j\omega\mu}(\dfrac{\partial E_z}{\partial y} + M_x) \\ H_y = \dfrac{1}{j\omega\mu}(\dfrac{\partial E_z}{\partial x} - M_y) \end{cases}. \tag{2.6}$$

The tangential $\mathbf{H}$ component to a surface with normal direction $\hat{\mathbf{n}}$ is frequently used to enforce the continuity of the tangential fields. One way to evaluate the tangential $\mathbf{H}$ at a

[1]It is also called the transverse magnetic problem.

sourceless point is

$$\begin{aligned}\hat{\mathbf{n}} \times \mathbf{H} =& \frac{1}{j\omega\mu}[n_x \frac{\partial E_z}{\partial x} + n_y \frac{\partial E_z}{\partial y}]\hat{z} \\ =& \frac{1}{j\omega\mu} \frac{\partial E_z}{\partial \hat{\mathbf{n}}} \hat{z},\end{aligned} \tag{2.7}$$

which is used in subsection 2.2 to derive the integral equations.

To solve the H-polarization problem[2] defined by (2.4), H_z is found by solving a similar scalar Helmholtz equation

$$\begin{aligned}\nabla^2 H_z + \omega^2 \mu\epsilon H_z = j\omega\epsilon M_z - \frac{\partial J_x}{\partial y} + \frac{\partial J_y}{\partial x} \\ \frac{\partial J_x}{\partial x} + \frac{\partial J_y}{\partial y} = -j\omega\rho_e,\end{aligned} \tag{2.8}$$

with a suitable boundary condition. Then, the corresponding $\mathbf{E}$ and the tangential $\mathbf{E}$ component at a sourceless point with surface normal direction $\hat{\mathbf{n}}$ are

$$\mathbf{E} = \frac{1}{j\omega\epsilon}(\nabla \times (0, 0, H_z) - \mathbf{J}) \Leftrightarrow \begin{cases} E_x = \frac{1}{j\omega\epsilon}(\frac{\partial H_z}{\partial y} - J_x) \\ E_y = \frac{-1}{j\omega\epsilon}(\frac{\partial H_z}{\partial x} + J_y) \end{cases} \tag{2.9}$$

and

$$\hat{\mathbf{n}} \times \mathbf{E} = \frac{-1}{j\omega\epsilon} \frac{\partial H_z}{\partial \hat{\mathbf{n}}} \hat{z},$$

respectively.

2.1.2 The Mixed-Potential Formulation for the Maxwell's Equation in 3-D

In order to simplify the derivation, the linearity of the Maxwell's equations is exploited. The Maxwell's equations in (2.1) are decomposed into two sets of equations where only one

[2]It is also called the transverse electric problem.

of the current sources is present:

$$\begin{aligned} \nabla \times \mathbf{E}^e &= -j\omega \mathbf{B}^e \\ \nabla \times \mathbf{H}^e &= j\omega \mathbf{D}^e + \mathbf{J} \\ \nabla \cdot \mathbf{D}^e &= \rho_e \\ \nabla \cdot \mathbf{B}^e &= 0 \end{aligned} \tag{2.10}$$

and

$$\begin{aligned} \nabla \times \mathbf{E}^m &= -j\omega \mathbf{B}^m - \mathbf{M} \\ \nabla \times \mathbf{H}^m &= j\omega \mathbf{D}^m \\ \nabla \cdot \mathbf{D}^m &= 0 \\ \nabla \cdot \mathbf{B}^m &= \rho_m \end{aligned} \tag{2.11}$$

where the solution to (2.1) is the linear superposition of the two solutions, e.g., $\mathbf{E} = \mathbf{E}^e + \mathbf{E}^m$.

The solution to (2.10) is found in the following, and that of (2.11) is found by duality. As the first step, the electric vector potential $\mathbf{A}$ is introduced to satisfy $\nabla \cdot \mathbf{B} = 0$ trivially by defining $\mathbf{B} = \nabla \times \mathbf{A}$:

$$\begin{array}{l|l} \nabla \times \mathbf{E}^e = -j\omega \mathbf{B}^e & \\ \nabla \times \mathbf{H}^e = j\omega \mathbf{D}^e + \mathbf{J} & \\ \nabla \cdot \mathbf{D}^e = \rho_e & \\ & \mathbf{B}^e = \nabla \times \mathbf{A} \end{array}$$

In order to show the role of the potentials more clearly, the left column shows the original equations that remain, and the right shows the equations with potentials that replace the original. Substituting $\mathbf{B}^e = \nabla \times \mathbf{A}$ into $\nabla \times \mathbf{E}^e = -j\omega \mathbf{B}^e$, the scalar potential ϕ_e is defined to trivially satisfy $\nabla \times (\mathbf{E} + j\omega \mathbf{A}) = 0$:

$$\begin{array}{l|l} & \mathbf{E}^e = -j\omega \mathbf{A} - \nabla \phi_e \\ \nabla \times \mathbf{H}^e = j\omega \mathbf{D}^e + \mathbf{J} & \\ \nabla \cdot \mathbf{D}^e = \rho_e & \\ & \mathbf{B}^e = \nabla \times \mathbf{A} \end{array}$$

The negative sign in front of $\nabla\phi_e$ ensures that the electric field lines point from a positive charge to a negative charge, consistent with the electrostatics [68, 69].

Assuming *homogeneous isotropic* media with $\mathbf{D} = \epsilon\mathbf{E}$ and $\mathbf{B} = \mu\mathbf{H}$ for permittivity ϵ and permeability μ and substituting the equations in the right column to those in the left give

$$\begin{aligned} \mathbf{E}^e &= -j\omega\mathbf{A} - \nabla\phi_e \\ \nabla^2\mathbf{A} + \omega^2\mu\epsilon\mathbf{A} &= -\mu\mathbf{J} + (\nabla\cdot\mathbf{A} + j\omega\mu\epsilon\phi_e) \\ \nabla^2\phi_e + j\omega\nabla\cdot\mathbf{A} &= -\rho_e/\epsilon \\ \mathbf{B}^e &= \nabla\times\mathbf{A}. \end{aligned} \tag{2.12}$$

There are more unknowns than the equations in (2.12) since $\mathbf{B} = \nabla\times\mathbf{A}$ does not uniquely specify $\mathbf{A}$, and $\nabla\cdot\mathbf{A}$ can be any value [69]. Nevertheless, all the $\mathbf{E}$ and $\mathbf{B}$ satisfying (2.12) for different $\mathbf{A}$ and ϕ_e are the same.

The potentials can be made unique if $\nabla\cdot\mathbf{A}$ is constrained. There are more than one way to do this since the absolute values of the potentials are of no interest. One popular method is the Lorenz gauge condition [69, 25],

$$\nabla\cdot\mathbf{A} = -j\omega\mu\epsilon\phi_e, \tag{2.13}$$

which gives

$$\begin{aligned} \nabla^2\mathbf{A} + \omega^2\mu\epsilon\mathbf{A} &= -\mu\mathbf{J} \\ \nabla^2\phi_e + \omega^2\mu\epsilon\phi_e &= -\rho_e/\epsilon \end{aligned} \tag{2.14}$$

to find the potentials. These equations decouples into scalar Helmholtz equations in the Cartesian coordinates and are easily solved with a suitable boundary condition, as it will be shown in section 2.3. Once the potentials $\mathbf{A}$ and ϕ_e are found, the associated fields are evaluated from

$$\begin{aligned} \mathbf{E}^e &= -j\omega\mathbf{A} - \nabla\phi_e \\ \mathbf{H}^e &= \frac{1}{\mu}\nabla\times\mathbf{A}. \end{aligned}$$

The remaining (2.11) can be solved by duality. Starting from (2.10), the substitutions[3]

$$\begin{array}{cccc} \mathbf{E} \to \mathbf{H} & \mathbf{D} \to \mathbf{B} & \mathbf{J} \to \mathbf{M} & \rho_e \to \rho_m \\ \mathbf{H} \to -\mathbf{E} & \mathbf{B} \to -\mathbf{D} & \mathbf{M} \to -\mathbf{J} & \rho_m \to \rho_e \end{array} \tag{2.15}$$

result in (2.11). This means that the solutions for $\mathbf{E}$ and $\mathbf{H}$ in (2.11) can be found from those for $\mathbf{H}$ and $\mathbf{E}$ in (2.10), respectively.

Of course, one can solve (2.11) by repeating the same steps as for (2.10) while defining potentials $\mathbf{F}$ and ϕ_m as

$$\begin{aligned} \mathbf{D}^m &= -\nabla \times \mathbf{F} \\ \mathbf{H}^m &= -j\omega\mathbf{F} - \nabla\phi_m. \end{aligned}$$

The result is $\mathbf{F}$ and ϕ_m satisfying

$$\begin{aligned} \nabla^2\mathbf{F} + \omega^2\mu\epsilon\mathbf{F} &= -\epsilon\mathbf{M} \\ \nabla^2\phi_m + \omega^2\mu\epsilon\phi_m &= -\rho_m/\mu \end{aligned} \tag{2.16}$$

and the fields are evaluated from

$$\begin{aligned} \mathbf{E}^m &= \frac{-1}{\epsilon}\nabla \times \mathbf{F} \\ \mathbf{H}^m &= -j\omega\mathbf{F} - \nabla\phi_m. \end{aligned}$$

2.2 Integral Equations for the 2-D Dielectric Scattering

2.2.1 Solution to the 2-D Boundary Value Problem

The partial differential operators (2.5) and (2.8) are useful to determine the sources $\mathbf{J}$ and $\mathbf{M}$ from the fields $\mathbf{E}$ and $\mathbf{H}$[4], but not the other way around. Integral operators are used to evaluate the fields from the sources.

In fact, the integral operators are the inverse of the partial differential operators with a suitable boundary condition. Suppose we want to find ϕ satisfying the boundary value problem with

$$\nabla^2\phi(\mathbf{r}) + k^2\phi(\mathbf{r}) = -\rho(\mathbf{r})$$

[3]Note that there are more than one way to establish duality, and other substitutions can be found in [25].
[4]This has to be done with care as pointed out in [70], page 162.

and the Sommerfeld radiation condition at infinity for a known source distribution ρ. The solution to this problem is given by [65]

$$\phi(\mathbf{r}) = \int \rho(\mathbf{r}')G(\mathbf{r},\mathbf{r}')\mathrm{d}\mathbf{r}'. \tag{2.17}$$

where the Green's function, or the fundamental solution, G is the solution to the boundary value problem with a point source δ at $\mathbf{r}'$ for ρ. If the boundary value problem is solved without any additional condition, the solution is

$$G(\mathbf{r},\mathbf{r}') = \frac{1}{4j}H_0^{(2)}(k||\mathbf{r}-\mathbf{r}'||) \tag{2.18}$$

where $H_0^{(2)}$ is the zeroth order Hankel function of the second kind. If the periodicity of ρ in one direction is considered, G is the 2-D Green's function for periodic structures in one direction as it will be shown in Chapter 3. The domain of integration for (2.17) encloses the entire source distribution for non-periodic charge distributions and one period of the source distribution for periodic ones.

2.2.2 Equivalence Principle

For a given problem, equivalent problems maintain the same fields as the given problem in some part of the domain, called the domain of interest [25, 60]. The fields outside the domain of interest can be anything for the equivalent problems. Equivalent problems are useful to reduce the complexity of the original problem if the fields in the domain of interest is only necessary. Furthermore, they are the cornerstone for developing integral equations for scattering and radiation in piecewise homogeneous media [59, 71, 72, 63, 73].

Equivalence principles systematically introduce equivalent sources and alter the media to construct equivalent problems. It is an idea known mostly for the Maxwell's equations [58, 25, 60], but it can be easily generalized to the Laplace and scalar Helmholtz equations. This subsection develops the equivalence principles for the scalar Helmholtz equation.

Equivalence principles are interpretations of mathematical principles and are categorized into two types. The first type is the interpretation of the Green's second identity [58]. Suppose ϕ satisfies the scalar Helmholtz equation $\nabla^2\phi + k^2\phi = 0$ for some wavenumber k in an open exterior domain Ω_0 containing infinity. With Sommerfeld radiation condition at

infinity, the Green's second identity gives [50]

$$\int_{\partial\Omega_0} \phi(\mathbf{r}') \frac{\partial G(\mathbf{r},\mathbf{r}')}{\partial \hat{\mathbf{n}}(\mathbf{r}')} - \frac{\partial \phi(\mathbf{r}')}{\partial \hat{\mathbf{n}}(\mathbf{r}')} G(\mathbf{r},\mathbf{r}') \mathrm{d}\mathbf{r}' = \begin{cases} \phi(\mathbf{r}), & \mathbf{r} \in \Omega_0 \\ 0, & \mathbf{r} \in \Omega_0^c \end{cases} \tag{2.19}$$

where $\hat{\mathbf{n}}(\mathbf{r}')$ is the normal derivative pointing into Ω_0 at $\mathbf{r}'$, and Ω_0^c is the complement of Ω_0. This means that if charge and dipole given by

$$\begin{aligned} \rho(\mathbf{r}) =& -\frac{\partial \phi(\mathbf{r})}{\partial \hat{\mathbf{n}}(\mathbf{r})} \\ \psi(\mathbf{r}) =& \phi(\mathbf{r}) \end{aligned} \tag{2.20}$$

are specified over $\partial\Omega_0$, the original field is maintained in Ω_0. Hence, the new problem with (2.20) on $\partial\Omega_0$ is equivalent to the original problem in Ω_0.

The distinguishing features of the first type are (a) the field in Ω_0^c is automatically zero; and (b) the equivalent sources are directly related to the original field ϕ by (2.20). The type-one equivalence principle in Electromagnetics is sometimes called extinction principle due to the zero field outside of the domain of interest [25], and integral equations based on the type-one equivalence principle are called the field formulations [59]. Equations similar to (2.19) exist for the Maxwell's equations [62] as well as the Laplace equation [27, 28], and type-one equivalence principles can be derived for these equations as well. Some type-one integral equations in Electromagnetics are shown in [25, 60] and will be used in subsection 2.3.2.

The second type relies on two mathematical principles: uniqueness principle for the fields and the existence of a solution to some boundary value problems. The uniqueness principle relates the field in the volume Ω_0 to the field on the boundary $\partial\Omega_0$. For instance, the uniqueness theorems of the scalar Helmholtz equation in section 3.3 of [50] state that the field in Ω_0 is uniquely determined if ϕ or its normal derivative is specified over $\partial\Omega_0$, and the Sommerfeld radiation condition is given at infinity.

Then, the equivalent sources to support the same field on $\partial\Omega_0$ is found by solving a boundary value problem, and the existence of solutions to the boundary value problem [27, 28, 50, 61] determines what combinations of sources are possible. For the scalar Helmholtz equation, charge and dipole sources, independently, can support arbitrary ϕ on $\partial\Omega_0$ as shown in section 3.4 of [50]. Furthermore, both charge ρ and dipole ψ related by $\rho = -j\alpha\psi$ for $\alpha \mathrm{Re}\{k\} \geq 0$ can support any ϕ on $\partial\Omega_0$ as shown in section 3.6 of [50].

If type-two equivalence principles are applied, (a) the field in Ω_0^c can be any value and determined by the choice of equivalent sources (charge or dipole) and boundary value problem to solve (support ϕ or $\partial\phi/\partial\hat{\mathbf{n}}$); and (b) no direct connection, such as (2.20), exists between ϕ and the sources. Integral equations in Electromagnetics based on the type-two equivalence principles are called source formulations [60]. Similar uniqueness principles and existence theorems for solutions to boundary value problems exist for the Maxwell's equations [61, 25] and the Laplace equation [27, 28].

Regardless of the type, the media in Ω_0^c can be chosen arbitrarily by choosing the Green's function for the Green's second identity or the boundary value problem. If the homogeneous Green's function is used, the medium in Ω_0^c becomes the same as Ω_0; such a choice is popular since the homogeneous Green's function is well known and easy to evaluate, but other choices are also possible [71, 72, 73, 74].

Consider an example shown in Figure 2-1. Suppose a source distribution ρ^i non-zero in

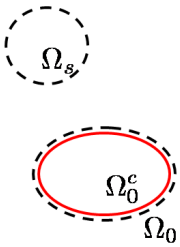

Figure 2-1: Example for type-one and type-two equivalence principles.

Ω_s supports a nonzero field

$$\phi(\mathbf{r}) = \int_{\Omega_s} G(\mathbf{r}, \mathbf{r}')\rho^i(\mathbf{r}')\mathrm{d}\mathbf{r}'$$

in a homogeneous medium. A fictitious boundary $\partial\Omega_0$ is drawn such that Ω_0 contains Ω_s and infinity, and equivalent sources are specified on $\partial\Omega_0$ to create an equivalent problem.

Consider the type-one equivalent principle. Since $\nabla^2\phi + k^2\phi = \rho^i$, (2.19) becomes [62]

$$\int_{\partial\Omega_0} \phi(\mathbf{r}')\frac{\partial G(\mathbf{r}, \mathbf{r}')}{\partial\hat{\mathbf{n}}(\mathbf{r}')} - \frac{\partial\phi(\mathbf{r}')}{\partial\hat{\mathbf{n}}(\mathbf{r}')}G(\mathbf{r}, \mathbf{r}')\mathrm{d}\mathbf{r}' + \phi(\mathbf{r}) = \begin{cases} \phi(\mathbf{r}), & \mathbf{r} \in \Omega_0 \\ 0, & \mathbf{r} \in \Omega_0^c. \end{cases} \tag{2.21}$$

The equivalent sources are nonzero and given by (2.20), and the overall effect of ρ^i, ρ, and ψ supports the same ϕ in Ω_0 and zero field in Ω_0^c. In other words, the field due to ρ and ψ

are zero in Ω_0, despite ρ and ψ being non-zero, and $-\phi$ in Ω_0^c.

To create an equivalent problem with a type-two equivalent principle using only ρ,

$$\int_{\partial\Omega_0} \rho(\mathbf{r}')G(\mathbf{r},\mathbf{r}')\mathrm{d}\mathbf{r}' + \int_{\Omega_s} \rho^i(\mathbf{r}')G(\mathbf{r},\mathbf{r}')\mathrm{d}\mathbf{r}' = \phi(\mathbf{r}), \quad \mathbf{r} \in \partial\Omega_0$$

has to be solved for ρ, and the existence of ρ is guaranteed by one of the existence theorems for the corresponding boundary value problem [50]. The solution for ρ is simply zero; ρ^i and ρ together supports the same ϕ in Ω_0, and the field in Ω_0^c happens to be the same as ϕ.

2.2.3 Integral Equations for the 2-D Dielectric Scattering

Consider a dielectric scatter in free space as shown in Figure 2-2. The outside Ω_0 and

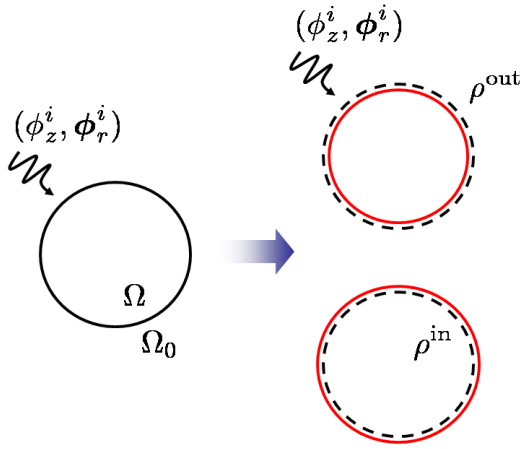

Figure 2-2: Equivalence principle for a source formulation.

inside Ω media are characterized by $(\epsilon^{\text{out}}, \mu^{\text{out}})$ and $(\epsilon^{\text{in}}, \mu^{\text{in}})$, respectively, and the wave number is determined by $k = \omega\sqrt{\epsilon\mu}$; ϕ stands for the scattered E_z for the E-polarization and H_z for the H-polarization. The dielectric scatterer is illuminated by an incident wave pair $(\phi_z^i, \boldsymbol{\phi}_r^i)$, which are E_z^i and $(H_x^i, H_y^i, 0)$ for the E-polarization and H_z^i and $(E_x^i, E_y^i, 0)$ for the H-polarization.

Green's functions for inhomogeneous media are known for simple inhomogeneities, such as a sphere in a homogeneous medium [69] and planar-stratified media [67]. For arbitrary piecewise homogeneous medium, the Green's function is nearly impossible to find and, mostly likely, hard to evaluate even if it can be found. Therefore, a method to formulate the problem with known Green's functions is necessary.

The problem of finding the Green's function for an arbitrary medium can be avoided for a piecewise homogeneous medium if equivalence principle is used [25, 60], and a source formulation [59] based on equivalent charges alone is used for the 2-D dielectric scattering. As a result, the equivalent sources do not have an interpretation in terms of the field, and the formulation has both the first- and second-kind integral equations. Even though the second-kind integral equations are preferred to the first-kind for various (numerical) reasons [57, 28], the shortcoming is compensated by the spectrally convergent Nyström method that will be proposed in chapter 3.

First, the original problem with an inhomogeneous medium is decomposed into two equivalent problems with homogeneous media and equivalent sources as shown in Figure 2-2. An exterior equivalent problem is constructed by (a) placing a line of unknown charge ρ^{out} just inside Ω; and (b) replacing the medium of Ω with that of Ω_0. Using (2.17), the field ϕ^{out} due to ρ^{out} is given by

$$\phi^{\text{out}}(\mathbf{r}) = \int_{\partial\Omega} \rho^{\text{out}}(\mathbf{r}')G^{\text{out}}(\mathbf{r},\mathbf{r}')\mathrm{d}\mathbf{r}'$$

where G^{out} is the Green's function for the homogeneous medium characterized by $(\epsilon^{\text{out}}, \mu^{\text{out}})$, and $\partial\Omega$ is the boundary of Ω.

Similarly, an interior equivalent problem is constructed by (a) placing a line of unknown charge ρ^{in} just outside Ω; and (b) replacing the medium of Ω_0 with that of Ω. The field ϕ^{in} due to ρ^{in} is

$$\phi^{\text{in}}(\mathbf{r}) = \int_{\partial\Omega} \rho^{\text{in}}(\mathbf{r}')G^{\text{in}}(\mathbf{r},\mathbf{r}')\mathrm{d}\mathbf{r}'$$

where G^{in} is the Green's function for the homogeneous medium characterized by $(\epsilon^{\text{in}}, \mu^{\text{in}})$.

With proper choice of ρ^{out} and ρ^{in}, the equivalence principle ensures that

$$\begin{cases} \phi^{\text{out}}(\mathbf{r}) = \phi(\mathbf{r}), & \mathbf{r} \in \Omega_0 \\ \phi^{\text{in}}(\mathbf{r}) = \phi(\mathbf{r}), & \mathbf{r} \in \Omega \end{cases}$$

where ϕ is the scattered field of the original problem [60, 25]. This is why they are called exterior and interior equivalent problems. The values of ϕ^{out} in Ω and ϕ^{in} in Ω_0 are unknown since the equivalence principle is type-two.

In order to find the unknown equivalent sources, continuity of the original scattered field

ϕ and the jump in its normal derivative across $\partial\Omega$ is used. This gives

$$\int_{\partial\Omega} \rho^{\text{out}}(\mathbf{r}')G^{\text{out}}(\mathbf{r},\mathbf{r}')\mathrm{d}\mathbf{r}' + \phi_z^i(\mathbf{r}) = \int_{\partial\Omega} \rho^{\text{in}}(\mathbf{r}')G^{\text{in}}(\mathbf{r},\mathbf{r}')\mathrm{d}\mathbf{r}', \quad \mathbf{r}\in\partial\Omega \tag{2.22}$$

and

$$\begin{aligned} &\alpha^{\text{out}}\frac{\partial}{\partial\hat{\mathbf{n}}(\mathbf{r})}\int_{\partial\Omega}\rho^{\text{out}}(\mathbf{r}')G^{\text{out}}(\mathbf{r},\mathbf{r}')\mathrm{d}\mathbf{r}' + \hat{z}\cdot\hat{\mathbf{n}}\times\boldsymbol{\phi}_r^i(\mathbf{r}) \\ &= \alpha^{\text{in}}\frac{\partial}{\partial\hat{\mathbf{n}}(\mathbf{r})}\int_{\partial\Omega}\rho^{\text{in}}(\mathbf{r}')G^{\text{in}}(\mathbf{r},\mathbf{r}')\mathrm{d}\mathbf{r}', \quad \mathbf{r}\in\partial\Omega \end{aligned} \tag{2.23}$$

where $\hat{\mathbf{n}}(\mathbf{r})$ is the outward normal to $\partial\Omega$ at $\mathbf{r}$. The scaling factors α^{out} and α^{in} are $1/j\omega\mu^{\text{out}}$ and $1/j\omega\mu^{\text{in}}$, respectively, for the E-polarization problem, and $-1/j\omega\epsilon^{\text{out}}$ and $-1/j\omega\epsilon^{\text{in}}$ for the H-polarization problem[5].

Once the equivalent charges are found, it can be used to compute the fields everywhere using (2.17) and (2.6) or (2.9), depending on E- or H-polarization, with a proper choice of the Green's function.

2.3 Integral Equations for the 3-D Dielectric Scattering

2.3.1 Solution to the 3-D Boundary Value Problem

Consider (2.14) with the Silver-Müller radiation boundary condition at infinity. Solving (2.14) for $\mathbf{A}$ and ϕ_e componentwize in the Cartesian coordinates with the corresponding radiation condition at infinity gives

$$\mathbf{A}(\mathbf{r}) = \mu\int \mathbf{J}(\mathbf{r}')G(\mathbf{r},\mathbf{r}')\mathrm{d}\mathbf{r}'$$

and

$$\phi_e(\mathbf{r}) = \frac{1}{\epsilon}\int \rho_e(\mathbf{r}')G(\mathbf{r},\mathbf{r}')\mathrm{d}\mathbf{r}'$$

with the Green's function for the homogeneous media [69, 25]

$$G(\mathbf{r},\mathbf{r}') = \frac{e^{-jk||\mathbf{r}-\mathbf{r}'||}}{4\pi||\mathbf{r}-\mathbf{r}'||}.$$

[5]It is sometimes more convenient to use the intrinsic impedance $\eta = \sqrt{\mu/\epsilon}$ instead of ϵ and μ. With the intrinsic impedance, $\alpha = 1/k\eta$ and $\alpha = -\eta/k$ for the E- and H-polarization problems, respectively.

Therefore, the solution to (2.10) is

$$\begin{aligned}\mathbf{E}^e(\mathbf{r}) &= -j\omega\mu \int \mathbf{J}(\mathbf{r}')G(\mathbf{r},\mathbf{r}')\mathrm{d}\mathbf{r}' - \frac{1}{\epsilon}\nabla \int \rho_e(\mathbf{r}')G(\mathbf{r},\mathbf{r}')\mathrm{d}\mathbf{r}', \\ \mathbf{H}^e(\mathbf{r}) &= \nabla \times \int \mathbf{J}(\mathbf{r}')G(\mathbf{r},\mathbf{r}')\mathrm{d}\mathbf{r}'.\end{aligned} \tag{2.24}$$

Similarly, the solutions to (2.16) are

$$\mathbf{F}(\mathbf{r}) = \epsilon \int \mathbf{M}(\mathbf{r}')G(\mathbf{r},\mathbf{r}')\mathrm{d}\mathbf{r}'$$

and

$$\phi_m(\mathbf{r}) = \frac{1}{\mu}\int \rho_m(\mathbf{r}')G(\mathbf{r},\mathbf{r}')\mathrm{d}\mathbf{r}',$$

and the solution to (2.11) is

$$\begin{aligned}\mathbf{E}^m(\mathbf{r}) &= -\nabla \times \int \mathbf{M}(\mathbf{r}')G(\mathbf{r},\mathbf{r}')\mathrm{d}\mathbf{r}' \\ \mathbf{H}^m(\mathbf{r}) &= -j\omega\epsilon \int \mathbf{M}(\mathbf{r}')G(\mathbf{r},\mathbf{r}')\mathrm{d}\mathbf{r}' - \frac{1}{\mu}\nabla \int \rho_m(\mathbf{r}')G(\mathbf{r},\mathbf{r}')\mathrm{d}\mathbf{r}',\end{aligned}$$

which can also be obtained by applying the substitution rules (2.15) to (2.24).

Combining the results, the electric and magnetic fields due to both the electric and the magnetic currents are

$$\begin{aligned}\mathbf{E}(\mathbf{r}) = -j\omega\mu \int \mathbf{J}(\mathbf{r}')G(\mathbf{r},\mathbf{r}')\mathrm{d}\mathbf{r}' - \frac{1}{\epsilon}\nabla \int \rho_e(\mathbf{r}')G(\mathbf{r},\mathbf{r}')\mathrm{d}\mathbf{r}' - \\ \nabla \times \int \mathbf{M}(\mathbf{r}')G(\mathbf{r},\mathbf{r}')\mathrm{d}\mathbf{r}',\end{aligned} \tag{2.25}$$

and

$$\begin{aligned}\mathbf{H}(\mathbf{r}) = -j\omega\epsilon \int \mathbf{M}(\mathbf{r}')G(\mathbf{r},\mathbf{r}')\mathrm{d}\mathbf{r}' - \frac{1}{\mu}\nabla \int \rho_m(\mathbf{r}')G(\mathbf{r},\mathbf{r}')\mathrm{d}\mathbf{r}' + \\ \nabla \times \int \mathbf{J}(\mathbf{r}')G(\mathbf{r},\mathbf{r}')\mathrm{d}\mathbf{r}'.\end{aligned} \tag{2.26}$$

Before closing the subsection, we show that (2.25) and (2.26) are related by a vector identity.

Lemma 1. *Suppose V is an open bounded set, and a continuously differentiable $\mathbf{X}(\mathbf{r})$ is*

nonzero only for $\mathbf{r}$ *in* V*. If the Green's function satisfies the Helmholtz equation*

$$\nabla^2 G(\mathbf{r}, \mathbf{r}') + k^2 G(\mathbf{r}, \mathbf{r}') = -\delta(\mathbf{r} - \mathbf{r}')$$

and has the additional property

$$\nabla G(\mathbf{r}, \mathbf{r}') = -\nabla' G(\mathbf{r}, \mathbf{r}'),$$

then

$$\nabla \times \nabla \times \int_V \mathbf{X}(\mathbf{r}') G(\mathbf{r}, \mathbf{r}')\, d\mathbf{r}' = \nabla \int_V [\nabla' \cdot \mathbf{X}(\mathbf{r}')] G(\mathbf{r}, \mathbf{r}')\, d\mathbf{r}' + k^2 \int_V \mathbf{X}(\mathbf{r}') G(\mathbf{r}, \mathbf{r}')\, d\mathbf{r}'$$

holds for $\mathbf{r}$ *not in* V*.*

Proof. Using the vector identity $\nabla \times \nabla \times \mathbf{a} = \nabla\nabla \cdot \mathbf{a} - \nabla^2 \mathbf{a}$,

$$\nabla \times \nabla \times \int_V \mathbf{X}(\mathbf{r}') G(\mathbf{r}, \mathbf{r}') \mathrm{d}\mathbf{r}' = \nabla [\nabla \cdot \int_V \mathbf{X}(\mathbf{r}') G(\mathbf{r}, \mathbf{r}') \mathrm{d}\mathbf{r}'] - \nabla^2 \int_V \mathbf{X}(\mathbf{r}') G(\mathbf{r}, \mathbf{r}') \mathrm{d}\mathbf{r}'. \tag{2.27}$$

Applying the vector identity $\nabla \cdot (a\mathbf{b}) = \nabla a \cdot \mathbf{b} + a \nabla \cdot \mathbf{b}$ to the first term in (2.27),

$$\begin{aligned} \nabla \cdot \int_V \mathbf{X}(\mathbf{r}') G(\mathbf{r}, \mathbf{r}') \mathrm{d}\mathbf{r}' &= \int_V \nabla G(\mathbf{r}, \mathbf{r}') \cdot \mathbf{X}(\mathbf{r}') \mathrm{d}\mathbf{r}' \\ &= -\int_V \nabla' G(\mathbf{r}, \mathbf{r}') \cdot \mathbf{X}(\mathbf{r}') \mathrm{d}\mathbf{r}' \\ &= \int_V [\nabla' \cdot \mathbf{X}(\mathbf{r}')] G(\mathbf{r}, \mathbf{r}') \mathrm{d}\mathbf{r}'. \end{aligned}$$

Next, the vector identity $\nabla^2(a\mathbf{b}) = (\nabla^2 a)\mathbf{b} + a(\nabla^2 \mathbf{b})$[6] is applied to the second term in (2.27), which gives

$$\begin{aligned} \nabla^2 \int_V \mathbf{X}(\mathbf{r}') G(\mathbf{r}, \mathbf{r}') \mathrm{d}\mathbf{r}' &= \int_V \mathbf{X}(\mathbf{r}') [\nabla^2 G(\mathbf{r}, \mathbf{r}')] \mathrm{d}\mathbf{r}' \\ &= -k^2 \int_V \mathbf{X}(\mathbf{r}') G(\mathbf{r}, \mathbf{r}') \mathrm{d}\mathbf{r}'. \end{aligned}$$

□

[6]The Laplacian operators have to be interpreted properly as either scalar or vector Laplacian operator.

Starting from (2.25),

$$\begin{aligned}\mathbf{H}(\mathbf{r}) &= \frac{-1}{j\omega\mu}\nabla\times\mathbf{E}(\mathbf{r}) \\ &= \nabla\times\int\mathbf{J}(\mathbf{r}')G(\mathbf{r},\mathbf{r}')\mathrm{d}\mathbf{r}' + \frac{1}{j\omega\mu}\nabla\times\nabla\times\int\mathbf{M}(\mathbf{r}')G(\mathbf{r},\mathbf{r}')\mathrm{d}\mathbf{r}',\end{aligned}$$

and applying Lemma 1 and the conservation law gives

$$\begin{aligned}\mathbf{H}(\mathbf{r}) = \nabla\times\int\mathbf{J}(\mathbf{r}')G(\mathbf{r},\mathbf{r}')\mathrm{d}\mathbf{r}'+ \\ \frac{1}{j\omega\mu}\nabla\int[\nabla'\cdot\mathbf{M}(\mathbf{r}')]G(\mathbf{r},\mathbf{r}')\mathrm{d}\mathbf{r}' + \frac{k^2}{j\omega\mu}\int\mathbf{M}(\mathbf{r}')G(\mathbf{r},\mathbf{r}')\mathrm{d}\mathbf{r}' \\ = -j\omega\epsilon\int\mathbf{M}(\mathbf{r}')G(\mathbf{r},\mathbf{r}')\mathrm{d}\mathbf{r}' - \frac{1}{\mu}\nabla\int\rho_m(\mathbf{r}')G(\mathbf{r},\mathbf{r}')\mathrm{d}\mathbf{r}'+ \\ \nabla\times\int\mathbf{J}(\mathbf{r}')G(\mathbf{r},\mathbf{r}')\mathrm{d}\mathbf{r}'.\end{aligned}$$

Of course, duality is an easier way to arrive at the same result.

2.3.2 Integral Equations for the 3-D Dielectric Scattering

Consider a 3-D dielectric scatterer illuminated by incident electric and magnetic fields $(\mathbf{E}^i, \mathbf{H}^i)$ as shown in Figure 2-3. Similar to the 2-D case in section 2.2, Ω is the scatterer

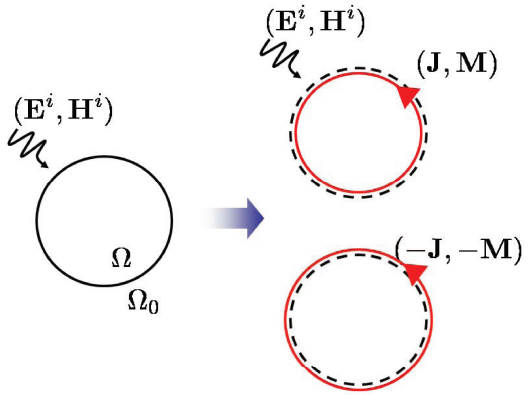

Figure 2-3: Equivalence principle for the PMCHW formulation.

characterized by $(\epsilon^{\text{in}}, \mu^{\text{in}})$, and Ω_0 is the outside medium characterized by $(\epsilon^{\text{out}}, \mu^{\text{out}})$.

PMCHW formulation is a well-known field formulation based on the extinction principle [59, 63, 64]. In order to create the exterior equivalent problem, the equivalent electric and

magnetic currents are defined as

$$\begin{aligned}\mathbf{J} =& \hat{\mathbf{n}} \times (\mathbf{H} + \mathbf{H}^i) \\ \mathbf{M} =& -\hat{\mathbf{n}} \times (\mathbf{E} + \mathbf{E}^i)\end{aligned}$$

where $\hat{\mathbf{n}}$ is the outward normal of $\partial\Omega$, and $\mathbf{E}$ and $\mathbf{H}$ are the unknown scattered electric and magnetic fields. The choice of equivalent currents comes from the Green's second identity and ensures that the resulting total fields are zero in Ω. The direction of the sources have to be flipped to create the interior equivalent problem; this leads to zero total fields in Ω_0.

The integral equations are found by enforcing tangential field continuity across $\partial\Omega$. For the simplicity of notation, suppose $\mathbf{E}^{\text{out}}(\mathbf{r};\mathbf{J},\mathbf{M})$ and $\mathbf{H}^{\text{out}}(\mathbf{r};\mathbf{J},\mathbf{M})$ are the electric and magnetic fields at $\mathbf{r}$ for the isotropic homogeneous medium characterized by $(\epsilon^{\text{out}}, \mu^{\text{out}})$ due to the source $\mathbf{J}$ and $\mathbf{M}$; $\mathbf{E}^{\text{in}}(\mathbf{r};\mathbf{J},\mathbf{M})$ and $\mathbf{H}^{\text{in}}(\mathbf{r};\mathbf{J},\mathbf{M})$ are defined in a similar manner. Then, the tangential field continuity translates to

$$\begin{aligned}\left[\mathbf{E}^{\text{out}}(\mathbf{r};\mathbf{J},\mathbf{M}) + \mathbf{E}^i(\mathbf{r})\right]_{\tan} &= \left[\mathbf{E}^{\text{in}}(\mathbf{r};-\mathbf{J},-\mathbf{M})\right]_{\tan}, \quad \mathbf{r} \in \partial\Omega \\ \left[\mathbf{H}^{\text{out}}(\mathbf{r};\mathbf{J},\mathbf{M}) + \mathbf{H}^i(\mathbf{r})\right]_{\tan} &= \left[\mathbf{H}^{\text{in}}(\mathbf{r};-\mathbf{J},-\mathbf{M})\right]_{\tan}, \quad \mathbf{r} \in \partial\Omega\end{aligned} \tag{2.28}$$

where $[\cdot]_{\tan}$ indicates that the tangential components are taken, for instance, by evaluating the outer product with $\hat{\mathbf{n}}$. From (2.25) and (2.26), $\mathbf{E}(\mathbf{r};\mathbf{J};\mathbf{M})$ and $\mathbf{H}(\mathbf{r};\mathbf{J},\mathbf{M})$ are

$$\begin{aligned}\mathbf{E}(\mathbf{r};\mathbf{J},\mathbf{M}) = -jk\eta \int \mathbf{J}(\mathbf{r}')G(\mathbf{r},\mathbf{r}')\mathrm{d}\mathbf{r}' + \frac{\eta}{jk}\nabla \int [\nabla'_s \cdot \mathbf{J}(\mathbf{r}')]G(\mathbf{r},\mathbf{r}')\mathrm{d}\mathbf{r}' - \\ \nabla \times \int \mathbf{M}(\mathbf{r}')G(\mathbf{r},\mathbf{r}')\mathrm{d}\mathbf{r}' \\ \mathbf{H}(\mathbf{r};\mathbf{J},\mathbf{M}) = -j\frac{k}{\eta} \int \mathbf{M}(\mathbf{r}')G(\mathbf{r},\mathbf{r}')\mathrm{d}\mathbf{r}' + \frac{1}{jk\eta}\nabla \int [\nabla'_s \cdot \mathbf{M}(\mathbf{r}')]G(\mathbf{r},\mathbf{r}')\mathrm{d}\mathbf{r}' + \\ \nabla \times \int \mathbf{J}(\mathbf{r}')G(\mathbf{r},\mathbf{r}')\mathrm{d}\mathbf{r}'\end{aligned} \tag{2.29}$$

where $\eta = \sqrt{\mu/\epsilon}$ is the intrinsic impedance, and ∇'_s is the surface gradient for sheets of current [65].

Once the unknown equivalent currents $\mathbf{J}$ and $\mathbf{M}$ are found, the field can be evaluated everywhere using $\mathbf{E}(\mathbf{r};\mathbf{J},\mathbf{M})$ and $\mathbf{H}(\mathbf{r};\mathbf{J},\mathbf{M})$ with $-\mathbf{J}$ and $-\mathbf{M}$ for inside and $\mathbf{J}$ and $\mathbf{M}$ for outside. For more details about the PMCHW formulation, refer to [59, 63, 64] and the references therein.

Chapter 3

Nyström Method for Periodic Structures in 2-D

Scattering by periodic structures has applications in many practically important devices. A classic expample is gratings used to analyze the spectrum of light [75, 34, 35, 36]. Gratings are also used as test structures to check and maintain the quality of the semiconductor fabrication process [16, 17, 18, 19, 20, 21, 22, 23]. Photonic crystals are a relatively new addition to the list, and they are used to manipulate the flow of light as the flow of electrons are controlled by semiconductors [76].

Analysis of periodic structures requires specialized methods. Truncation of the structures can save memory and computing power, but it often leads to incorrect results [77]. Furthermore, truncated structures may still be too large for most conventional methods to analyze, as it will be demonstrated in section 3.6.

Finite-difference and finite-element methods with periodic boundary conditions can solve guided wave problems effectively by discretizing one period [75, 78, 79, 42, 80, 81, 82, 83, 84], but it is difficult to apply them to scattering problems since the radiation boundary condition at infinity needs a special treatment [85, 86, 87, 88, 89, 90, 91, 44, 42]. Rigorous coupled wave analysis is a mode expansion-type method and solves scattering problems by periodic structures [34, 35, 36]. The method is well suited for analyzing gratings, but it is unsuitable for a forward analysis algorithm to solve a inverse wave scattering problem; the intermediate eigenvalue decomposition step makes the Jacobian evaluation difficult.

A surface integral equation method with a specialized Green's function incorporating

periodicity is one of the best methods to analyze scattering due to periodic structures [75, 92, 93, 77, 94], especially, as a part of an inverse wave analysis. The method exactly incorporates the infinite periodicity of the scatterer as well as the radiation boundary condition at infinity, and only the boundaries of scatterers in a single period have to be discretized. Furthermore, there is an efficient method to approximate the Jacobian as it will be shown in chapter 4.

This chapter presents a spectrally convergent Nyström method for 2-D structures infinitely periodic in one direction. Similar methods for 2-D structures without periodicity are well established for open arcs [95, 96, 97, 98, 99, 100] as well as scatterers with closed boundaries [101, 50, 28]. The authors know of no spectrally convergent Nyström method for periodic structures in 2-D; the existing methods for periodic structures solve the surface integral equations with projection methods [93, 77, 94].

Spectrally convergent Nyström methods cleverly combine: (a) singularity separation; (b) parameterization of the boundary; and (c) spectrally convergent numerical integration scheme for singular weight functions, in order to approximate integral operators with spectral accuracy. The convergence of the integral operator approximation and that of the solution to the integral equation are closely related. Roughly speaking, the solution of an integral equation converges spectrally if the numerical approximations to the integral operators converge spectrally under some mild additional technical assumptions. Formal convergence theory can be found in chapter 10 and 12 of [28] (general theory) and in [102, 101, 97, 98] (specific integral equations).

The method described herein varies slightly depending on how the boundary of the scatterer is parameterized since the type of parameterization affects the singular function that can be integrated numerically with spectral accuracy. The non-periodic parameterization suitable to describe an open boundary, such as a single period of a surface grating, is considered in this chapter. The method for periodic parameterization commonly used for closed boundaries is shown in Appendix A.

First, a numerically stable method to evaluate the 2-D Green's function for infinitely periodic structures in one direction is summarized in section 3.1. For brevity, the 2-D Green's function for infinitely periodic structures in one direction is called the *periodic Green's function* for the rest of the thesis. Then, a spectrally convergent Nyström method for the monopole and the normal derivative of the monopole operators is developed in the subsequent sections: singularity separation in section 3.2, parameterization in subsection 3.3,

and spectrally convergent numerical quadratures for unit and singular weight functions in section 3.4. The resulting discretized integral operators and the discretization of integral operators are given in section 3.5. Finally, the accuracy and the rate of convergence of the proposed method are demonstrated in section 3.6.

3.1 Evaluation of the Periodic Green's Function

The periodic Green's function is known to be difficult to evaluate. The series in the naive form converges too slowly and cannot be truncated easily [92, 93, 103, 104]. Many transformations to improve the convergence of the series have been proposed, including the integral representations, lattice sums, and Ewald methods [92].

In this section, the Ewald methods in the existing literature are summarized. The Ewald methods are preferred to other transformations since the singularities can be easily separated from the smooth part, which is an important for constructing a spectrally convergent Nyström method in the subsequent sections. The "naive" form is presented in subsection 3.1.2, and an alternative form that avoids numerical overflow is given in subsection 3.1.3.

3.1.1 Definition

Consider a scatterer infinitely periodic in x with period T, illuminated by an incident field

$$\phi^i(x, y) = e^{jk(\beta x + \cos\theta^i y)}.$$

with incident angle θ^i and $\beta = k \sin\theta^i$. It is known that the the scattered field ϕ for the given problem is *quasi-periodic* [75, 93, 105],

$$\phi(x + T, y) = e^{-j\beta T}\phi(x, y).$$

There are several ways to prove quasi-periodicity: [75] presents a proof based on uniqueness of the solution for perfectly conducting and dielectric scatterer; and [105] shows an integral equation based argument for perfectly conducting scatterers. The quasi-periodicity is a direct result of geometric periodicity, and a more general proof based on symmetry and group theory is shown in [76].

Quasi-periodic fields can be represented with the periodic Green's function. The periodic Green's function yields the field everywhere due to point sources periodic in x with period T and with incremental phase shift of β for each period [104]:

$$G(\mathbf{r},\mathbf{r}') = \sum_{m=-\infty}^{\infty} e^{-jm\beta T}\frac{1}{4j}H_0^{(2)}(kR_m) \tag{3.1}$$

where $R_m = \sqrt{[x-(x'+mT)]^2+(y-y')^2}$. This naive form is difficult to evaluate since the terms decay slowly, and the series cannot be truncated with a few terms [92, 93, 103, 104]. An alternative derivation of the periodic Green's function starting from the boundary value problem can be found in [93].

3.1.2 The Ewald Representation

The Ewald method transforms (3.1) to improve the convergence of the series. Using the spectral representation of the Hankel function [92, 93, 104, 77]

$$G(\mathbf{r},\mathbf{r}') = \sum_{m=-\infty}^{\infty} e^{-jm\beta T}\frac{1}{2\pi}\int_0^{\infty}\frac{e^{-R_m^2s^2+\frac{k^2}{4s^2}}}{s}\mathrm{d}s.$$

Consider dividing the range of integration to $[0,E]$ and $[E,\infty)$ for a non-negative value E. The first series,

$$G_1(\mathbf{r},\mathbf{r}') = \frac{1}{2\pi}\sum_{m=-\infty}^{\infty} e^{-jm\beta T}\int_0^{E}\frac{e^{-R_m^2s^2+\frac{k^2}{4s^2}}}{s}\mathrm{d}s,$$

converges quickly, so it is kept in the spatial domain and truncated. Unfortunately, the second series,

$$G_2(\mathbf{r},\mathbf{r}') = \frac{1}{2\pi}\sum_{m=-\infty}^{\infty} e^{-jm\beta T}\int_E^{\infty}\frac{e^{-R_m^2s^2+\frac{k^2}{4s^2}}}{s}\mathrm{d}s, \tag{3.2}$$

converges slowly.

Ewald proposed in [106] to evaluate (3.2) in the spectral domain using the Poisson summation formula [92, 104]; if a function is smooth and decays slowly in the spatial domain, its spectral representation decays rapidly [107]. After some changes of variables, $G = G_1 + G_2$ with

$$G_1(\mathbf{r},\mathbf{r}') = \frac{1}{4\pi}\sum_{m=-\infty}^{\infty} e^{-jm\beta T}\sum_{n=0}^{\infty}\frac{(Ek)^{2n}}{n!}\mathrm{E}_{n+1}(\frac{R_m^2}{4E^2}) \tag{3.3}$$

and

$$G_2(\mathbf{r},\mathbf{r}') = \frac{1}{4T}\sum_{m=-\infty}^{\infty}\frac{e^{-j\beta_m(x-x')}}{j\gamma_m}[e^{j\gamma_m|y-y'|}\mathrm{erfc}(j\gamma_m E+\frac{|y-y'|}{2E})+ e^{-j\gamma_m|y-y'|}\mathrm{erfc}(j\gamma_m E-\frac{|y-y'|}{2E})], \tag{3.4}$$

where

$$\beta_m = \beta + m\frac{2\pi}{T}$$
$$\gamma_m = \sqrt{k^2-\beta_m^2}$$

with $\mathrm{Im}\{\gamma_m\} \leq 0$[1]. The complementary error function and exponential integral are

$$\mathrm{erfc}(z) = \frac{2}{\sqrt{\pi}}\int_z^\infty e^{-t^2}\mathrm{d}t$$

and

$$\mathrm{E}_m(z) = \int_1^\infty \frac{e^{-zt}}{t^m}\mathrm{d}t. \tag{3.5}$$

The complementary error function with complex arguments can be evaluated with the algorithm in [108]. The first order exponential integral is evaluated with the *expint* routine in MATLAB that combines (5.1.11) and (5.1.22) of [109], and the higher order exponential integrals are evaluated with the recurrence relation in [93, 104] and (5.1.14) of [109].

By a judicious choice of E, the (3.3) and (3.4) converge much faster than the naive form in (3.1). Refer to [92, 93, 104, 77] for more detailed derivation.

3.1.3 Numerically Stable Ewald Representation

The naive form in (3.4) can create numerical overflow if either (a) m is large; or (b) the evaluation point is far away from the periodic sources in the y direction. This problem is caused by $\exp[-j\gamma_m|y-y'|]$ that grows rapidly for large m and $|y-y'|$.

The numerical overflow can be avoided if the scaled complementary error function [77, 109],

$$\mathrm{w}(z) = e^{-z^2}\mathrm{erfc}(-jz),$$

is used instead of the complementary error function for G_2 [77]. With w, (3.4) can be

[1]The choice of sign for γ_m ensures that the value is either decaying or radiating in the y direction.

re-written as

$$G_2(\mathbf{r},\mathbf{r}') = \frac{e^{\frac{-(y-y')^2}{4E^2}}}{4T} \sum_{m=-\infty}^{\infty} \frac{e^{-j\beta_m(x-x')}e^{(E\gamma_m)^2}}{j\gamma_m}[\mathrm{w}(-E\gamma_m + j\frac{|y-y'|}{2E}) + \mathrm{w}(-E\gamma_m - j\frac{|y-y'|}{2E})], \tag{3.6}$$

which is stable for large values of m. Nevertheless, (3.6) can still cause numerical overflows for large values of $|y-y'|$ since w grows exponentially along the negative imaginary axis.

Additional properties of w are used to solve this problem. The growth of w can be kept small regardless of the sign of $\mathrm{Im}\{z\}$ if

$$|\mathrm{Re}\{z\}| \geq |\mathrm{Im}\{z\}| \tag{3.7}$$

since w satisfies [77]

$$|\mathrm{w}(z)| \leq 2e^{-(\mathrm{Re}\{z\})^2+(\mathrm{Im}\{z\})^2} + |\mathrm{w}(-z)|.$$

As a result, if (3.7) does not hold for $-E\gamma_m - j\frac{|y-y'|}{2E}$, or equivalently $\frac{|y-y'|}{2E^2} > \mathrm{Re}\{\gamma_m\} - \mathrm{Im}\{\gamma_m\}$, the alternative form on the right-hand side of

$$\mathrm{w}(-E\gamma_m - j\frac{|y-y'|}{2E}) = 2e^{-(E\gamma_m)^2+\frac{(y-y')^2}{4E^2}-j\gamma_m|y-y'|} - \mathrm{w}(E\gamma_m + j\frac{|y-y'|}{2E})$$

is used instead.

Therefore, a numerically stable form of G_2 is

$$\begin{aligned} G_2(\mathbf{r},\mathbf{r}') = &\frac{e^{\frac{-(y-y')^2}{4E^2}}}{4T}\{\sum_{m\in\mathcal{Z}_1} \frac{e^{-j\beta_m(x-x')}e^{(E\gamma_m)^2}}{j\gamma_m}[\mathrm{w}(-E\gamma_m + j\frac{|y-y'|}{2E}) + \\ &\mathrm{w}(-E\gamma_m - j\frac{|y-y'|}{2E})] + \\ &\sum_{m\in\mathcal{Z}_2} \frac{e^{-j\beta_m(x-x')}e^{(E\gamma_m)^2}}{j\gamma_m}[\mathrm{w}(-E\gamma_m + j\frac{|y-y'|}{2E}) - \\ &\mathrm{w}(E\gamma_m + j\frac{|y-y'|}{2E})]\} + \frac{1}{2T}\sum_{m\in\mathcal{Z}_2} \frac{e^{-j\beta_m(x-x')}e^{-j\gamma_m|y-y'|}}{j\gamma_m} \end{aligned} \tag{3.8}$$

where

$$\mathcal{Z}_2 = \{m \in \mathcal{Z} | \frac{|y-y'|}{2E^2} > \mathrm{Re}\{\gamma_m\} - \mathrm{Im}\{\gamma_m\}\}, \tag{3.9}$$

and $\mathcal{Z}_1$ partitions the set of all integers $\mathcal{Z}$ with $\mathcal{Z}_2$.

3.1.4 Derivatives

The derivative evaluations are straightforward. Using (5.1.26) of [109],

$$\frac{\partial G_1}{\partial x}(\mathbf{r},\mathbf{r}') = \frac{-1}{8\pi E^2}\sum_{m=-\infty}^{\infty} e^{-jm\beta T}[x-(x'+mT)]\sum_{n=0}^{\infty}\frac{(kE)^{2n}}{n!}\mathrm{E}_n(\frac{R_m^2}{4E^2}), \tag{3.10}$$

and

$$\frac{\partial G_1}{\partial y}(\mathbf{r},\mathbf{r}') = \frac{-(y-y')}{8\pi E^2}\sum_{m=-\infty}^{\infty} e^{-jm\beta T}\sum_{n=0}^{\infty}\frac{(kE)^{2n}}{n!}\mathrm{E}_n(\frac{R_m^2}{4E^2}). \tag{3.11}$$

Similarly, (7.1.20) of [109] gives

$$\begin{aligned}
&\frac{\partial G_2}{\partial x}(\mathbf{r},\mathbf{r}') \\
&\quad = -\frac{e^{\frac{-(y-y')^2}{4E^2}}}{4T}\{\sum_{m\in\mathcal{Z}_1}\frac{\beta_m e^{-j\beta_m(x-x')}e^{(E\gamma_m)^2}}{\gamma_m}[\mathrm{w}(-E\gamma_m+j\frac{|y-y'|}{2E})+ \\
&\qquad \mathrm{w}(-E\gamma_m-j\frac{|y-y'|}{2E})]+ \\
&\quad \sum_{m\in\mathcal{Z}_2}\frac{\beta_m e^{-j\beta_m(x-x')}e^{(E\gamma_m)^2}}{\gamma_m}[\mathrm{w}(-E\gamma_m+j\frac{|y-y'|}{2E})- \\
&\qquad \mathrm{w}(E\gamma_m+j\frac{|y-y'|}{2E})]\} - \frac{1}{2T}\sum_{m\in\mathcal{Z}_2}\frac{\beta_m e^{-j\beta_m(x-x')}e^{-j\gamma_m|y-y'|}}{\gamma_m},
\end{aligned} \tag{3.12}$$

and

$$\begin{aligned}
&\frac{\partial G_2}{\partial y}(\mathbf{r},\mathbf{r}') \\
&\quad = \frac{e^{\frac{-(y-y')^2}{4E^2}}}{4T}\mathrm{sgn}(y-y')\{\sum_{m\in\mathcal{Z}_1} e^{-j\beta_m(x-x')}e^{(E\gamma_m)^2}[\mathrm{w}(-E\gamma_m+j\frac{|y-y'|}{2E})- \\
&\qquad \mathrm{w}(-E\gamma_m-j\frac{|y-y'|}{2E})] + \sum_{m\in\mathcal{Z}_2} e^{-j\beta_m(x-x')}e^{(E\gamma_m)^2}[\mathrm{w}(-E\gamma_m+j\frac{|y-y'|}{2E})+ \\
&\qquad \mathrm{w}(E\gamma_m+j\frac{|y-y'|}{2E})]\} - \frac{1}{2T}\mathrm{sgn}(y-y')\sum_{m\in\mathcal{Z}_2} e^{-j\beta_m(x-x')}e^{-j\gamma_m|y-y'|}.
\end{aligned} \tag{3.13}$$

3.1.5 Summary

The periodic Green's function is given by $G = G_1 + G_2$ where G_1 and G_2 are in (3.3) and (3.8), respectively. Its normal derivative is given by

$$\begin{aligned} G_n =& \hat{\mathbf{n}} \cdot \nabla G \\ =& n_x(\frac{\partial G_1}{\partial x} + \frac{\partial G_2}{\partial x}) + n_y(\frac{\partial G_2}{\partial y} + \frac{\partial G_2}{\partial y}) \end{aligned} \tag{3.14}$$

where the necessary partial derivatives are evaluated by (3.10), (3.12), (3.11), and (3.13).

3.2 Singularity Separation

In order to approximate integral operators with singular Green's functions with spectral accuracy, the singular part of the Green's function has to be separated from the smooth (infinitely differentiable) part [50, 28], since the numerical integration scheme designed for smooth functions do not converge spectrally for singular functions, and vice verse [110, 111].

The singularity separation for the periodic Green's function is different from that for the 2-D Green's function in two ways. First, multiple singularities due to the neighboring sources are separated for non-periodic parameterizations that stretch from one end of the period to the other end. Second, the series representation of the singularities derived in in [93, 104] is difficult to evaluate for large values of R_m compared to the wavelength; the terms in the series oscillate wildly between positive and negative values and introduces significant cancellation errors. The connection between the series representations and the Bessel functions has been identified, and the well-established algorithms to evaluate the Bessel functions can be used to evaluate the singularities.

The singularity sparation for Nyström methods is different from the singularity extraction in the potential integral evaluation, such as in [30, 112, 113]. The singularity extraction usually extracts only the dominant singularity, and the resulting function has discontinuities in the derivatives. If such an extraction is used with a Nyström method, the resulting method will show linear convergence since numerical quadratures designed for smooth functions converge linearly for functions with a discontinuity in the derivatives [110, 111, 114].

3.2.1 The Periodic Green's Function

The logarithmic singularity of the periodic Green's function is part of G_1 in (3.3) since

$$\mathrm{E}_1(z) = -\gamma - \log z - \sum_{m=1}^{\infty} \frac{(-1)^m z^m}{m m!},$$

where γ is the Euler constant [109]. From the recursion relation in [93, 104],

$$\mathrm{E}_n^{\mathrm{s}}(z) = (-1)^n \frac{z^{n-1}}{(n-1)!},$$

and the function multiplying $\log R_0^2$ is

$$\begin{aligned} G^{\mathrm{s},0}(\mathbf{r},\mathbf{r}') =& \frac{1}{4\pi} \sum_{n=0}^{\infty} \frac{(Ek)^{2n}}{n!} \mathrm{E}_{n+1}^{\mathrm{s}}(\frac{R_0^2}{4E^2}) \\ =& -\frac{1}{4\pi} \sum_{n=0}^{\infty} \frac{(-1)^n}{(n!)^2} (\frac{k^2 R_0^2}{4})^n. \end{aligned}$$

This summation is difficult to evaluate when $(k^2 R_0^2/4)$ is much larger than one.

Fortunately, this is exactly the expansion of the Bessel function of zeroth order near 0 as shown in (9.1.10) of [109]. Therefore,

$$G^{\mathrm{s},0}(\mathbf{r},\mathbf{r}') = -\frac{1}{4\pi} J_0(kR_0)$$

alternatively, and the routines to evaluate the Bessel function can be used to evaluate $G^{\mathrm{s},0}$ stably for large values of the argument.

When a boundary stretches from one end of the period to the other, the periodic sources in the neighboring periods slows the convergence of the numerical quadrature for smooth functions. Therefore, the logarithmic singularities due to the neighboring sources have to be separated as well. With multiple singularity separation, the periodic Green's function is

$$G(\mathbf{r},\mathbf{r}') = G^{\mathrm{r}}(\mathbf{r},\mathbf{r}') + G^{\mathrm{s},-1}(\mathbf{r},\mathbf{r}') \log R_{-1}^2 + G^{\mathrm{s},0}(\mathbf{r},\mathbf{r}') \log R_0^2 + G^{\mathrm{s},1}(\mathbf{r},\mathbf{r}') \log R_1^2$$

where G^{r}, $G^{\mathrm{s},-1}$, $G^{\mathrm{s},0}$, and $G^{\mathrm{s},1}$ are smooth functions given by

$$\begin{aligned} G^{\mathrm{s},-1}(\mathbf{r},\mathbf{r}') &= -\frac{1}{4\pi}e^{j\beta T}J_0(kR_{-1}) \\ G^{\mathrm{s},0}(\mathbf{r},\mathbf{r}') &= -\frac{1}{4\pi}J_0(kR_0) \\ G^{\mathrm{s},1}(\mathbf{r},\mathbf{r}') &= -\frac{1}{4\pi}e^{-j\beta T}J_0(kR_1), \end{aligned} \tag{3.15}$$

and

$$G^{\mathrm{r}}(\mathbf{r},\mathbf{r}') = G(\mathbf{r},\mathbf{r}') - G^{\mathrm{s},-1}(\mathbf{r},\mathbf{r}')\log R_{-1}^2 - G^{\mathrm{s},0}(\mathbf{r},\mathbf{r}')\log R_0^2 - G^{\mathrm{s},1}(\mathbf{r},\mathbf{r}')\log R_1^2. \tag{3.16}$$

3.2.2 Normal Derivative of the Periodic Green's Function

Similarly, the function multiplying $\log R_0^2$ for G_n is

$$\begin{aligned} G_n^{\mathrm{s},0}(\mathbf{r},\mathbf{r}') =& -\frac{1}{8\pi E^2}[n_x(x-x')+n_y(y-y')]\sum_{n=1}^{\infty}\frac{(Ek)^{2n}}{n!}\mathrm{E}_n^{\mathrm{s}}(\frac{R_0^2}{4E^2}) \\ =& \frac{k^2}{8\pi}[n_x(x-x')+n_y(y-y')]\sum_{n=0}^{\infty}\frac{(-1)^n}{n!(n+1)!}(\frac{k^2R_0^2}{4})^n \\ =& \frac{k}{4\pi}[n_x(x-x')+n_y(y-y')]\frac{J_1(kR_0)}{R_0} \end{aligned}$$

where (9.1.10) of [109] is used for the last equality. Considering the neighboring singularities, the normal derivative of the periodic Green's function can be written as

$$G_n(\mathbf{r},\mathbf{r}') = G_n^{\mathrm{r}}(\mathbf{r},\mathbf{r}') + G_n^{\mathrm{s},-1}(\mathbf{r},\mathbf{r}')\log R_{-1}^2 + G_n^{\mathrm{s},0}(\mathbf{r},\mathbf{r}')\log R_0^2 + G_n^{\mathrm{s},1}(\mathbf{r},\mathbf{r}')\log R_1^2$$

where G_n^{r}, $G_n^{\mathrm{s},-1}$, $G_n^{\mathrm{s},0}$, and $G_n^{\mathrm{s},1}$ are smooth functions given by

$$\begin{aligned} G_n^{\mathrm{s},-1}(\mathbf{r},\mathbf{r}') =& \frac{k}{4\pi}[n_x(x-x'+T)+n_y(y-y')]e^{j\beta T}\frac{J_1(kR_{-1})}{R_{-1}} \\ G_n^{\mathrm{s},0}(\mathbf{r},\mathbf{r}') =& \frac{k}{4\pi}[n_x(x-x')+n_y(y-y')]\frac{J_1(kR_0)}{R_0} \\ G_n^{\mathrm{s},1}(\mathbf{r},\mathbf{r}') =& \frac{k}{4\pi}[n_x(x-x'-T)+n_y(y-y')]e^{-j\beta T}\frac{J_1(kR_1)}{R_1}, \end{aligned} \tag{3.17}$$

and

$$G_n^{\mathrm{r}}(\mathbf{r},\mathbf{r}') = G_n(\mathbf{r},\mathbf{r}') - G_n^{\mathrm{s},-1}(\mathbf{r},\mathbf{r}')\log R_{-1}^2 - G_n^{\mathrm{s},0}(\mathbf{r},\mathbf{r}')\log R_0^2 - G_n^{\mathrm{s},1}(\mathbf{r},\mathbf{r}')\log R_1^2. \tag{3.18}$$

3.3 Parameterization of Boundary

It is difficult to devise a spectrally convergent numerical quadrature that integrates any smooth function times $\log ||\mathbf{r} - \mathbf{r}'||^2$ since $\mathbf{r}$ and $\mathbf{r}'$ can be any two points on an arbitrary curve. Therefore, a global parameterization is used to simplify the singularity [95, 96, 97, 98, 101, 99, 100, 50, 28].

Consider a smooth vector-valued function $\mathbf{q}$ that maps $[-1, 1]$ to a non-self intersecting open curve from one end of the period to the other. The source and test points are $\mathbf{r}' = \mathbf{q}(\tau)$ and $\mathbf{r} = \mathbf{q}(t)$, respectively, for some τ and t in $[-1, 1]$, and the integral operators become

$$\int G(\mathbf{r}, \mathbf{r}')\rho(\mathbf{r}')\mathrm{d}\mathbf{r}' = \int_{-1}^{1} G(\mathbf{q}(t), \mathbf{q}(\tau))\rho(\mathbf{q}(\tau))||\mathbf{q}'(\tau)||\mathrm{d}\tau$$

and

$$\int G_n(\mathbf{r}, \mathbf{r}')\rho(\mathbf{r}')\mathrm{d}\mathbf{r}' = \int_{-1}^{1} G_n(\mathbf{q}(t), \mathbf{q}(\tau))\rho(\mathbf{q}(\tau))||\mathbf{q}'(\tau)||\mathrm{d}\tau.$$

For convenience of presentation, the parameterization is assumed to start from the left end of the period and end at the right[2]. Then, the Green's function is

$$\begin{aligned} &G(\mathbf{q}(t), \mathbf{q}(\tau)) \\ &\quad = \tilde{G}^{\mathrm{r}}(\mathbf{q}(t), \mathbf{q}(\tau)) + 2G^{\mathrm{s},-1}(\mathbf{q}(t), \mathbf{q}(\tau)) \log |(t+2) - \tau| + \\ &\quad\quad 2G^{\mathrm{s},0}(\mathbf{q}(t), \mathbf{q}(\tau)) \log |t - \tau| + 2G^{\mathrm{s},1}(\mathbf{q}(t), \mathbf{q}(\tau)) \log |(t-2) - \tau| \end{aligned} \tag{3.19}$$

where

$$\begin{aligned} &\tilde{G}^{\mathrm{r}}(\mathbf{q}(t), \mathbf{q}(\tau)) \\ &\quad = \begin{cases} G^{\mathrm{r}}(\mathbf{q}(t), \mathbf{q}(\tau)) + G^{\mathrm{s},-1}(\mathbf{q}(t), \mathbf{q}(\tau)) \log \dfrac{R_{-1}^2}{|(t+2) - \tau|^2} + \\ \quad G^{\mathrm{s},0}(\mathbf{q}(t), \mathbf{q}(\tau)) \log \dfrac{R_0^2}{|t - \tau|^2} + \\ \quad G^{\mathrm{s},1}(\mathbf{q}(t), \mathbf{q}(\tau)) \log \dfrac{R_1^2}{|(t-2) - \tau|^2}, \quad t \neq \tau \\ G^{\mathrm{r}}(\mathbf{q}(t), \mathbf{q}(t)) + G^{\mathrm{s},-1}(\mathbf{q}(t), \mathbf{q}(t)) \log \dfrac{R_{-1}^2}{4} + \\ \quad 2G^{\mathrm{s},0}(\mathbf{q}(t), \mathbf{q}(t)) \log ||\mathbf{q}'(t)|| + \\ \quad G^{\mathrm{s},1}(\mathbf{q}(t), \mathbf{q}(t)) \log \dfrac{R_1^2}{4}, \quad t = \tau \end{cases} \end{aligned} \tag{3.20}$$

[2]If the direction of the parameterization is the opposite, the $|(t \pm 2) - \tau|$ has to be replaced by $|(t \mp 2) - \tau|$.

is smooth for $|t|$, $|\tau| < 1$[3]. The logarithmic singularities no longer depend on the shape of the boundary and can be integrated more easily.

The same idea can be applied to G_n, and the result is (3.19) and (3.20) with $\tilde{G}^{\mathrm{r}}$, G^{r}, $G^{\mathrm{s},-1}$, $G^{\mathrm{s},0}$, and $G^{\mathrm{s},1}$ replaced by $\tilde{G}^{\mathrm{r}}_n$, G^{r}_n, $G^{\mathrm{s},-1}_n$, $G^{\mathrm{s},0}_n$, and $G^{\mathrm{s},1}_n$, respectively.

3.4 Numerical Quadrature

Spectrally convergent numerical quadratures of the form

$$\int_{-1}^{1} f(\tau)\mathrm{d}\tau = \sum_{n=0}^{N_q-1} w^{1}_{n/N_q} f(\tau_{n/N_q})$$
$$\int_{-1}^{1} f(\tau)\log|t-\tau|\mathrm{d}\tau = \sum_{n=0}^{N_q-1} w^{\log}_{n/N_q}(t) f(\tau_{n/N_q})$$

are devised where f is a smooth function. In addition to the spectral convergence requirement, the quadrature points, or abscissas, τ_{n/N_q} should be the same for different weight functions in order to match the unknowns. Therefore, Gaussian quadratures cannot be used.

Fejér quadratures for both unit and $\log|t-\tau|$ weights are developed. Fejér quadratures use the spectral convergence of the Chebyshev polynomial interpolation at the zeros of a Chebyshev polynomial for smooth functions on $[-1,1]$[4]. If the interpolated polynomial is integrated exactly, the result is the first-kind Fejér quadrature [116, 117]. The interpolated polynomial times $\log|t-\tau|$ is integrated exactly, and the result is a first-kind modified Fejér quadrature [118].

The first-kind modified Fejér quadrature to create a spectrally convergent Nyström method for $\log|t-\tau|$ weight function is a novel contribution. A similar modified Clenshaw-Curtis quadrature is used in [119] for the 2-D Green's function, but the spectral convergence is not demonstrated. The relation between first/second-kind Fejér and Clenshaw-Curtis quadratures and their FFT acceleration can be found in [114, 120, 121].

[3]This condition is met for open quadrature rules, such as the first-kind Fejér quadrature shown in subsection 3.4.

[4]The zeros of a Chebyshev polynomial are also called the Chebyshev nodes and play an important role in approximation theory [115].

3.4.1 First-Kind Fejér Quadratures

Suppose T_l is the lth order Chebyshev polynomial. For a given function f, $\tilde{f}$ interpolating f at the zeros of the N_qth order Chebyshev polynomial[5],

$$\tau_{n/N_q} = \cos\frac{(2n-1)\pi}{2N_q}, \quad n = 1, \cdots, N_q, \tag{3.21}$$

is

$$\tilde{f}(t) = \sum_{l=0}^{N_q-1}{}' a_l T_l(t) = \frac{1}{2}a_0 + \sum_{l=1}^{N_q-1} a_l T_l(t)$$

where

$$a_l = \frac{2}{N_q}\sum_{n=1}^{N_q} T_l(\tau_{n/N_q}) f(\tau_{n/N_q}).$$

Integrating $\tilde{f}(t)$ times a weight function $w(\cdot;t)$ exactly instead of f gives

$$\begin{aligned}\int_{-1}^{1} f(\tau)w(\tau;t)\mathrm{d}\tau &\approx \int_{-1}^{1} \tilde{f}(\tau)w(\tau;t)\mathrm{d}\tau \\ &= \sum_{n=1}^{N_q}[\frac{2}{N_q}\sum_{l=0}^{N_q-1}{}' \cos\frac{l(2n-1)\pi}{2N_q} M_l(t)] f(\tau_{n/N_q}),\end{aligned}$$

where

$$M_l(t) = \int_{-1}^{1} T_l(\tau)w(\tau;t)\mathrm{d}\tau \tag{3.22}$$

is the modified Chebyshev moment of order l. The resulting numerical quadrature is spectrally convergent for a smooth f [123] since the Chebyshev polynomial interpolation error reduces spectrally for smooth function [115, 124, 114].

3.4.2 Modified Chebyshev Moment Evaluation

The problem of constructing the Fejér quadrature for a given weight function w becomes the problem of finding the corresponding modified Chebyshev moments. For $w(\tau) = 1$, they

[5]The Chebyshev polynomial interpolation in $[-1, 1]$ is closely related to the trigonometric polynomial interpolation in $[0, 2\pi]$ through a simple cosine transformation. For some f defined in $[-1, 1]$, the Chebyshev polynomial interpolation can be understood as applying trigonometric polynomial interpolation to the 2π-periodic function $(f \circ \cos)$ in $[0, 2\pi]$ [122].

are known in a closed form:

$$\begin{aligned} M_l^1 &= \int_{-1}^{1} T_l(\tau)\mathrm{d}\tau \\ &= \begin{cases} 0, & l\text{: odd} \\ \dfrac{2}{1-l^2}, & l\text{: even} \end{cases} \end{aligned}$$

Therefore, the spectrally convergent quadrature for a smooth $f(t)$ is

$$\int_{-1}^{1} f(\tau)\mathrm{d}\tau \approx \sum_{n=1}^{N_q} w_{n/N_q}^1 f(\tau_{n/N_q}) \tag{3.23}$$

where

$$w_{n/N_q}^1 = \frac{2}{N_q} \sum_{l=0}^{N_q-1} \cos\frac{l(2n-1)\pi}{2N_q} M_l^1.$$

The modified Chebyshev moments $M_l^{\log}(t)$ for $w(\tau) = \log|t-\tau|$, $|t|<1$ are evaluated by a recurrence relation [118]

$$\begin{aligned} &(l-1)(l+2)M_{l+1}^{\log}(t) - 2t(l^2-1)M_l^{\log}(t) + (l+1)(l-2)M_{l-1}^{\log}(t) \\ =&2(-1)^l(t+1)\log(t+1) - 2(1-t)\log(1-t) - (l-1)M_{l+1}^1 + (l+1)M_{l-1}^1. \end{aligned} \tag{3.24}$$

The forward recursion from

$$\begin{aligned} M_0^{\log}(t) =&(1+t)\log(1+t) + (1-t)\log(1-t) - 2 \\ M_1^{\log}(t) =&tM_0^{\log}(t) + \frac{1}{2}(1-t)^2\log(1-t) - \frac{1}{2}(1+t)^2\log(1+t) + t \end{aligned}$$

is stable for $|t|<1$ [118]. Therefore, the spectrally convergent quadrature for a smooth f and $|t|<1$ is

$$\int_{-1}^{1} f(\tau)\log|t-\tau|\mathrm{d}\tau \approx \sum_{n=1}^{N_q} w_{n/N_q}^{\log}(t) f(\tau_{n/N_q}) \tag{3.25}$$

where

$$w_{n/N_q}^{\log}(t) = \frac{2}{N_q} \sum_{l=0}^{N_q-1} \cos\frac{l(2n-1)\pi}{2N_q} M_l^{\log}(t).$$

For $\log|(t\pm 2)-\tau|$ weight function, the recurrence relation in (3.24) fails since (a) the logarithmic functions are not defined for $(t\pm 2)$ instead of t; and (b) the forward recursion

is no longer stable for $|t \pm 2|$, $|t| < 1$. The generalization of (3.24) to any t is

$$\begin{aligned}&(l-1)(l+2)M_{l+1}^{\log}(t) - 2t(l^2-1)M_l^{\log}(t) + (l+1)(l-2)M_{l-1}^{\log}(t)\\ =&2(-1)^l(t+1)\log|t+1| - 2(1-t)\log|1-t| - (l-1)M_{l+1}^1 + (l+1)M_{l-1}^1\end{aligned} \tag{3.26}$$

with

$$\begin{aligned}M_0^{\log}(t) =&(1-t)\log|1-t| + (1+t)\log|1+t| - 2\\ M_1^{\log}(t) =&\frac{1}{2}(1-t^2)(\log|1-t| - \log|t+1|) - t.\end{aligned} \tag{3.27}$$

The unstable recurrence relation in (3.26) is evaluated with the Olver's algorithm [125, 126]. The algorithm evaluates the recurrence relation as a boundary value problem to control the growth of the numerical error by setting $M_{l_{\max}} = 0$ for sufficiently large $l_{\max}$ adaptively determined; it is a reasonable approximation if the moments asymptotically decay to zero as order increases.

The asymptotic convergence of the modified Chebyshev moments to zero can be shown indirectly using the bounds on the Fourier coefficients of continuous functions. By the change of variable $\tau = \cos\theta$,

$$\begin{aligned}M_l^{\log}(t) =& \int_{-1}^{1} T_m(\tau)\log|t-\tau|\mathrm{d}\tau\\ =&\frac{1}{2}\int_{-\pi}^{\pi} |\sin\theta|\log|t-\cos\theta|\cos(m\theta)\mathrm{d}\theta,\end{aligned} \tag{3.28}$$

and the lth order modified Chebyshev moment for $\log|t-\tau|$ is the lth order Fourier coefficient of the 2π periodic function $f(\theta) = |\sin\theta|\log|t-\cos\theta|$. Since f is continuous for $t \neq \pm 1$, the asymptotic bounds on the Fourier coefficients of continuous functions[6] ensure that the modified Chebyshev moments asymptotically converge to zero.

[6] An example of such theorem is Theorem 4 in Chapter 2 of [122].

3.5 Summary of the Method

Consider the monopole operator $\int G(\mathbf{r},\mathbf{r}')\rho(\mathbf{r}')\mathrm{d}\mathbf{r}'$. Given a non-periodic parameterization $\mathbf{q}$ and $\mathbf{r}=\mathbf{q}(t)$ for some $t\in(-1,1)$,

$$\begin{aligned}\int G(\mathbf{r},\mathbf{r}')\rho(\mathbf{r}')\mathrm{d}\mathbf{r}' \approx \sum_{n=1}^{N_q}[&w^1_{n/N_q}\tilde{G}^{\mathrm{r}}(\mathbf{q}(t),\mathbf{q}(\tau^{\mathrm{p}}_{n/N_q}))+\\ &2w^{\log}_{n/N_q}(t+2)\,G^{\mathrm{s},-1}(\mathbf{q}(t),\mathbf{q}(\tau_{n/N_q}))+\\ &2w^{\log}_{n/N_q}(t)\,G^{\mathrm{s},0}(\mathbf{q}(t),\mathbf{q}(\tau_{n/N_q}))+\\ &2w^{\log}_{n/N_q}(t-2)\,G^{\mathrm{s},1}(\mathbf{q}(t),\mathbf{q}(\tau_{n/N_q}))]\cdot\\ &||\mathbf{q}'(\tau_{n/N_q})||\rho(\mathbf{q}(\tau_{n/N_q}).\end{aligned} \tag{3.29}$$

The normal derivative of the monopole operator $\int G_n(\mathbf{r},\mathbf{r}')\rho(\mathbf{r}')\mathrm{d}\mathbf{r}'$ is discretized similarly, and the result is (3.29) with $\tilde{G}^{\mathrm{r}}$, $G^{\mathrm{s},-1}$, $G^{\mathrm{s},0}$, and $G^{\mathrm{s},1}$ replaced by $\tilde{G}^{\mathrm{r}}_n$, $G^{\mathrm{s},-1}_n$, $G^{\mathrm{s},0}_n$, and $G^{\mathrm{s},1}_n$, respectively.

Consider an integral equation with the monopole operator

$$\int G(\mathbf{r},\mathbf{r}')\rho(\mathbf{r}')\mathrm{d}\mathbf{r}' = f(\mathbf{r}),$$

where f is a function, which can be another integral operator. In order to get a system of linear equations, (a) the monopole operator is approximated by (3.29); and (b) the approximated equation is tested at the quadrature points $\mathbf{q}(\tau_{m/N_q})$, $m=1,\cdots,N_q$. The result is the system of linear equations

$$\mathbf{S}\boldsymbol{\rho}=\mathbf{f}, \tag{3.30}$$

where

$$\begin{aligned}\mathbf{s}_{m,n} =[&w^1_{n/N_q}\tilde{G}^{\mathrm{r}}(\mathbf{q}(\tau_{m/N_q}),\mathbf{q}(\tau_{n/N_q}))+\\ &2w^{\log}_{n/N_q}(\tau_{m/N_q}+2)\,G^{\mathrm{s},-1}(\mathbf{q}(\tau_{m/N_q}),\mathbf{q}(\tau_{n/N_q}))+\\ &2w^{\log}_{n/N_q}(\tau_{m/N_q})\,G^{\mathrm{s},0}(\mathbf{q}(\tau_{m/N_q}),\mathbf{q}(\tau_{n/N_q}))+\\ &2w^{\log}_{n/N_q}(\tau_{m/N_q}-2)\,G^{\mathrm{s},1}(\mathbf{q}(\tau_{m/N_q}),\mathbf{q}(\tau_{n/N_q}))]||\mathbf{q}'(\tau_{n/N_q})||,\end{aligned} \tag{3.31}$$

and

$$\begin{aligned}\rho_n =& \rho(\mathbf{q}(\tau_{n/N_q}))\\ f_m =& f(\mathbf{q}(\tau_{m/N_q})),\end{aligned}$$

for $m, n = 1, \cdots, N_q$. Similarly, discretizing and testing

$$\int G_n(\mathbf{r}, \mathbf{r}')\rho(\mathbf{r}')\mathrm{d}\mathbf{r}' = f(\mathbf{r})$$

for a function f gives

$$\mathbf{K}'\boldsymbol{\rho} = \mathbf{f} \tag{3.32}$$

where the entry $\mathbf{k}'_{m,n}$ of $\mathbf{K}'$ is given by (3.31) with $\tilde{G}^{\mathrm{r}}$, $G^{\mathrm{s},-1}$, $G^{\mathrm{s},0}$, and $G^{\mathrm{s},1}$ replaced by $\tilde{G}^{\mathrm{r}}_n$, $G^{\mathrm{s},-1}_n$, $G^{\mathrm{s},0}_n$, and $G^{\mathrm{s},1}_n$, respectively.

As an example, consider the integral equations (2.22) and (2.23) for 2-D dielectric scattering by a homogeneous scatterer whose boundary is parameterized by $\mathbf{q}$. Once discretized and tested, the resulting system of linear equations is

$$\begin{bmatrix} \mathbf{S}^{\mathrm{out}} & -\mathbf{S}^{\mathrm{in}} \\ \alpha^{\mathrm{out}}\mathbf{K}'^{\mathrm{out}} & -\alpha^{\mathrm{in}}\mathbf{K}'^{\mathrm{in}} \end{bmatrix} \begin{bmatrix} \boldsymbol{\rho}^{\mathrm{out}} \\ \boldsymbol{\rho}^{\mathrm{in}} \end{bmatrix} = - \begin{bmatrix} \boldsymbol{\phi}^i_z \\ \boldsymbol{\phi}^i_r \end{bmatrix} \tag{3.33}$$

where

$$\begin{aligned}\rho^{\mathrm{out}}_n =& \rho^{\mathrm{out}}(\mathbf{q}(\tau_{n/N_q}))\\ \rho^{\mathrm{in}}_n =& \rho^{\mathrm{in}}(\mathbf{q}(\tau_{n/N_q}))\\ \phi^i_{z,m} =& \phi^i_z(\mathbf{q}(\tau_{m/N_q}))\\ \phi^i_{r,m} =& \hat{z}\cdot\hat{\mathbf{n}}\times\boldsymbol{\phi}^i_r(\mathbf{q}(\tau_{m/N_q}))\end{aligned}$$

for $m, n = 1, \cdots, N_q$. Once the solutions $\boldsymbol{\rho}^{\mathrm{out}}_E$ and $\boldsymbol{\rho}^{\mathrm{out}}_H$ for the E- and H-polarization problems are found, the outside $\mathbf{E}$ at $\mathbf{r}$, not on the boundary, is evaluated by

$$\mathbf{E} = \mathbf{C} \begin{bmatrix} \boldsymbol{\rho}^{\mathrm{out}}_E \\ \boldsymbol{\rho}^{\mathrm{out}}_H \end{bmatrix} \tag{3.34}$$

where 3-by-$2N_q$ matrix $\mathbf{C}$ is

$$\begin{aligned} C_{1,N_q+n} =& \frac{1}{j\omega\epsilon^{\text{out}}} w^1_{n/N_q} \frac{\partial G}{\partial y}(\mathbf{r}, \mathbf{q}(\tau_{n/N_q})) \\ C_{2,N_q+n} =& \frac{-1}{j\omega\epsilon^{\text{out}}} w^1_{n/N_q} \frac{\partial G}{\partial x}(\mathbf{r}, \mathbf{q}(\tau_{n/N_q})) \\ C_{3,n} =& w^1_{n/N_q} G(\mathbf{r}, \mathbf{q}(\tau_{n/N_q})), \end{aligned}$$

$n = 1, \cdots, N_q$, and the other entries are zero.

3.6 Numerical Examples

This section presents some computational results with the proposed Nyström method. First, the use of periodic Green's function is justified by comparing the results using truncation and the proposed methods in subsection 3.6.1. The rate of convergence of the proposed method is verified for dielectric scattering in subsection 3.6.2. Finally, the effect of smoothness of the parameterization on the rate of convergence is investigated in subsection 3.6.3.

3.6.1 Truncation versus the Periodic Green's Function

In order to justify the use of periodic Green's function, reflectance as a function of the incident angle is evaluated. An infinitely long film is illuminated by a plane wave from above with wavelength λ_0 and varying incident angles. The dielectric has thickness λ_0, permittivity $12\epsilon_0$, and permeability μ_0; and the medium above and below the dielectric film is vacuum (permittivity ϵ_0 and permeability μ_0).

First, the infinitely long film is truncated to a $100\lambda_0$-long dielectric slab, and the truncated problem is solved using 20 quadrature points per wavelength per unknown equivalent source. The resulting system of linear equations, similar to (3.33), is too large to fit into the memory. Therefore, the matrix is sparsified with FFT [127], and the system of linear equations is solved iteratively with GMRES [128, 129] with circulant matrix preconditioning [130, 131].

Figure 3-1 shows the reflectance for E- and H-polarizations computed by truncation superimposed on the reference values from an analytic formula [67, 132]. As immediately seen, the computed values are quite inaccurate. Furthermore, the accuracy of the result degrades as the incident angle increases; this is a well known problem of truncation [77].

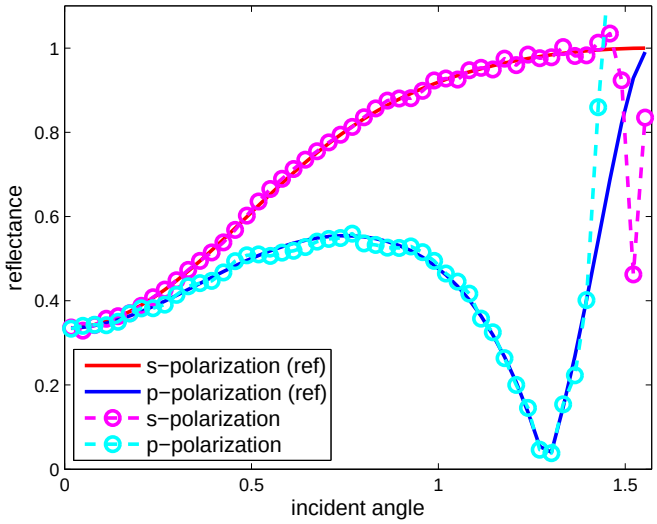

Figure 3-1: Reflectance of the dielectric film in air as a function of the incident angle computed by truncation.

The problem can be completely avoided with the proposed method as shown in Figure 3-2. The period of the Green's function is set to λ_0, and 20 quadrature points per unknown equivalent source is used for fair comparison.

Note that, the periodic Green's function can be used to model semi-infinite domains without a specialized Green's function, such as the substrate Green's function [71, 72, 73, 74]. This is demonstrated with the structure in Figure 3-3, which is a simplified example for a periodic grating embedded in a substrate. The layers have permittivity of ϵ_0, $3.7\epsilon_0$, $12\epsilon_0$, and $3.7\epsilon_0$ from the top, and the permeability is μ_0 for all the layers. The structure is illuminated by a plane wave from vacuum with wavelength λ_0 and varying incident angles, and the reflectance as a function of the incident angle is shown in Figure 3-4. The example uses 50 quadrature points per unknown equivalent source.

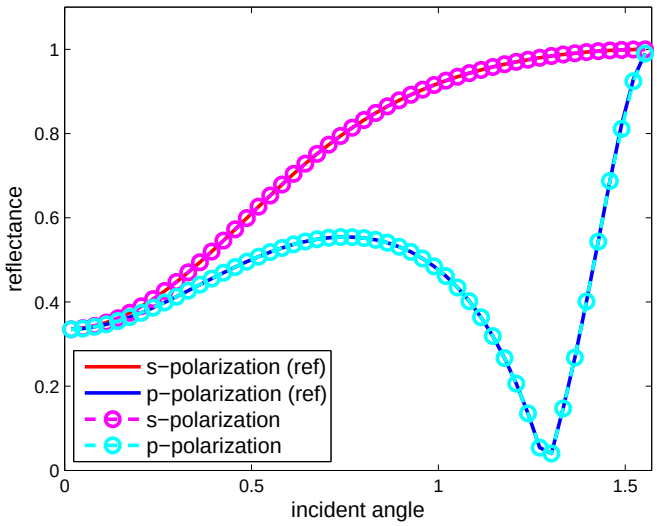

Figure 3-2: Reflectance of the dielectric film in air as a function of the incident angle computed by the proposed Nyström method for the periodic Green's function.

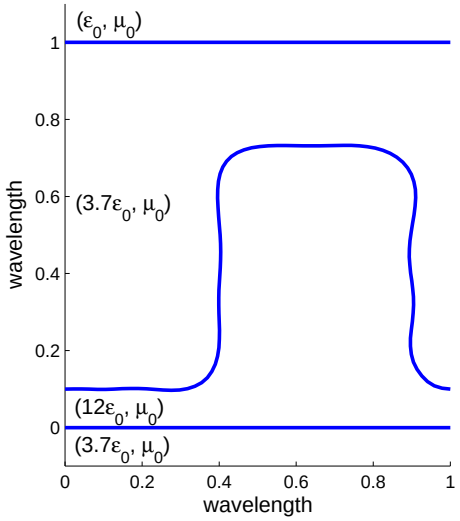

Figure 3-3: Periodic grating embedded in a substrate.

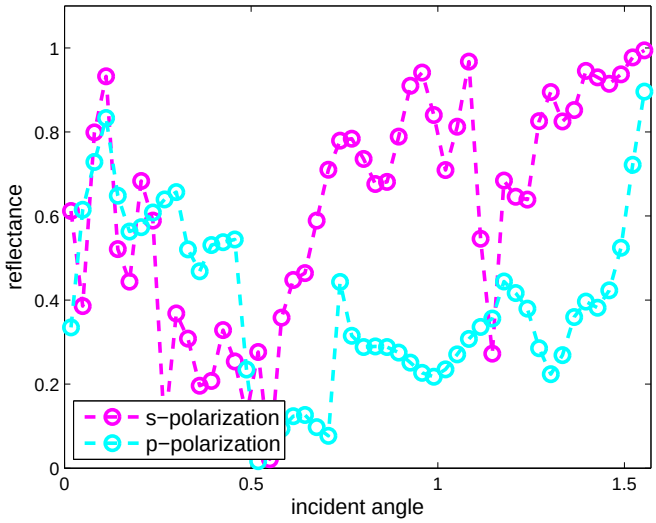

Figure 3-4: Reflectance of the structure in Figure 3-3 as a function of the incident angle.

3.6.2 Convergence Verification

Consider a sinusoidal dielectric interface between vacuum and a medium with $12\epsilon_0$ and μ_0 parameterized by[7]

$$\begin{aligned} q_x(t) =& \frac{1.3827\lambda_0}{2}(1-t) \\ q_y(t) =& 0.1\lambda_0 \sin(\pi(t+1)). \end{aligned} \tag{3.35}$$

The structure is illuminated by a plane wave from vacuum with wavelength λ_0 and incident angle $\pi/6$.

Figure 3-5 shows the relative error in the scattered field measured $10\lambda_0$ away from the structure in the $(\sin(\pi/6), \cos(\pi/6), 0)$ direction. As one can see, the proposed method clearly shows spectral convergence[8]. The convergence of the other method that only extracts the singularity associated with $G^{\mathrm{s},0}$ quickly saturates and becomes linear. Since there is no known analytic solution for this problem, the fields evaluated with 100 quadrature points per unknown equivalent source for each method are used as the references, and the relative error between the two references is 5.0043×10^{-8}.

The convergence of the field for the structure in Figure 3-3 is shown in Figure 3-6.

[7]The parameterization is from the right to the left to keep the normal direction point into vacuum, and a flat interface is avoided to thoroughly test $\mathbf{K}'$.

[8]Different types of convergence and ways to identify them from the error plots are explained in Chapter 2 of [122].

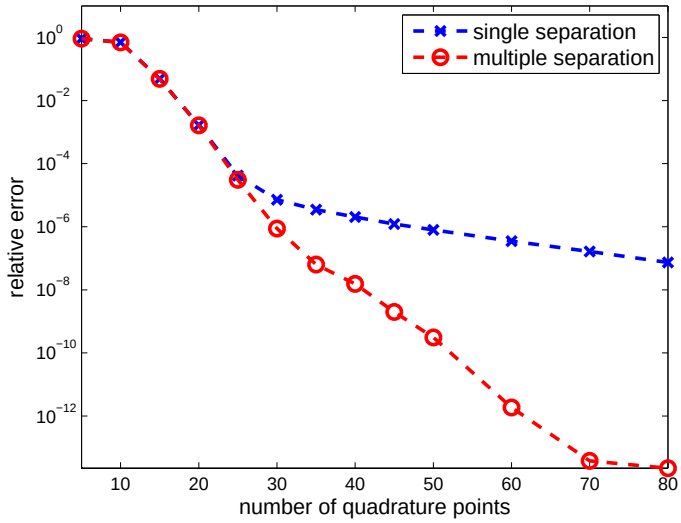

Figure 3-5: Relative error in the scattered field due to the dielectric interface in (3.35).

The incident field and the measurement points are identical to those in Figure 3-5, and

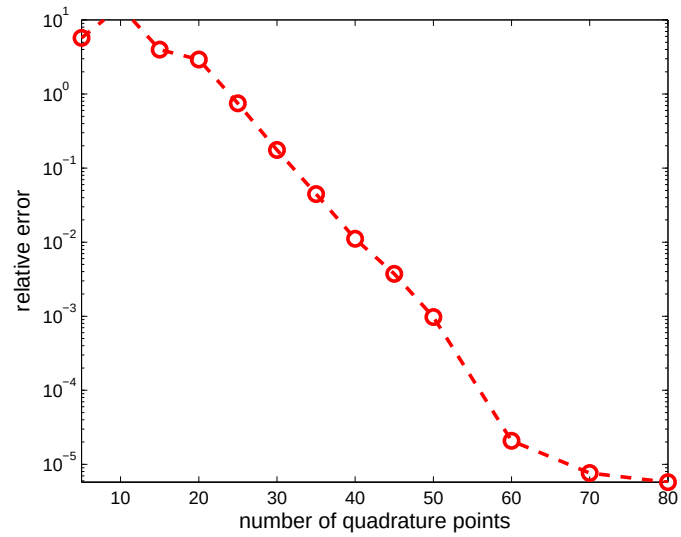

Figure 3-6: Relative error in the scattered field due to the structure in Figure 3-3.

the reference field is computed with 100 quadrature points per equivalent source. The convergence is still spectral, but it is slower than what is shown in Figure 3-5. This is due to the small distance between the bottom dielectric interface and part of the dielectric interface just above it in Figure 3-3.

To understand the relation between the distance between interfaces and the rate of

convergence further, a wavy dielectric film with $12\epsilon_0$ and μ_0 in air is investigated. The bottom dielectric interface is parameterized by (3.35), and the top dielectric interface is (3.35) shifted vertically. Figure 3-7 shows the convergence of the scattered field for three different vertical separations. Even though all three cases converge spectrally, the slope

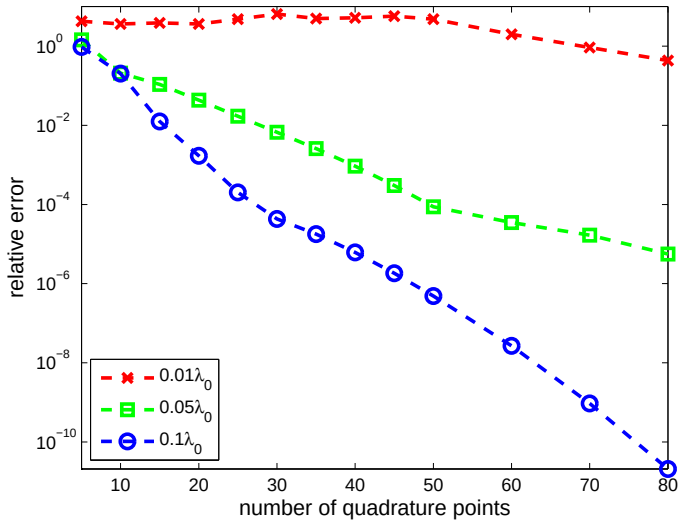

Figure 3-7: Relative error in the scattered field for three different film thickness.

strongly depends on the vertical separation: the larger the distance, the steeper the slope. This is due to the first-kind Fejér quadrature used to evaluate the interaction between the two interfaces. The convergence of a numerical quadrature for a smooth integrand deteriorates as the singularities of the integrand in the complex domain approach the domain of integration [110, 111, 114].

The incident field has wavelength λ_0 and incident angle $\pi/6$, and the scattered field is measured at $10\lambda_0$ away from the structure in the $(\sin(\pi/6), \cos(\pi/6), 0)$ direction. Finally, the reference fields are evaluated with 100 quadrature points per unknown equivalent source.

3.6.3 Boundary Approximation

Consider an interface between vacuum and a dielectric medium with $12\epsilon_0$ and μ_0 shown in Figure 3-8. The interface is illuminated by a plane wave from vacuum with wavelength λ_0 and incident angle $\pi/6$, and the period of the structure is $1.3827\lambda_0$.

To see the relation between the smoothness of the parameterization and the rate of convergence of the solution, the figure shows three different parameterizations: (a) a simple

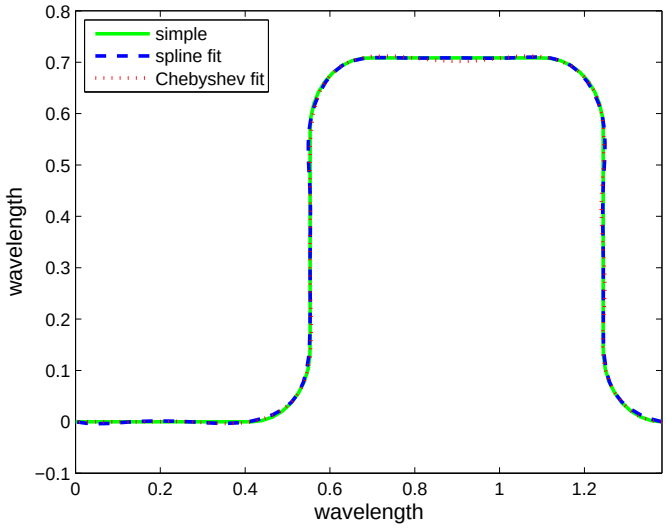

Figure 3-8: Three different parameterizations for simple grating with different smoothness.

parameterization with lines and quarter circles; (b) a cubic spline interpolation to q_x and q_y with 20 knots while enforcing periodic derivatives at the ends [133]; and (c) a Chebyshev polynomial interpolation to q_x and q_y with 20 samples. Even though they are nearly indistinguishable in the figure, the simple parameterization has discontinuity in the second derivative, the cubic spline interpolation is continuous up to the second derivative, and the Chebyshev interpolation is smooth.

Figure 3-9 shows the relative error in the solution as the number of quadrature points is increased. Reference values are computed with 100 quadrature points for each parameterization; the relative error between the reference values computed with simple and Chebyshev parameterizations is 0.0276, and the relative error between those computed with spline and Chebyshev parameterizations is 0.0419. The result shows that approximation to the parameterization is necessary to achieve rapid convergence[9]. Due to the lack of an analytic solution, the error introduced by approximating the parameterization is difficult to quantify but is believed to be small.

For smooth parameterizations, the Chebyshev interpolation converges quickly as the number of samples increases. Figure 3-10 shows the relative error in the scattered field as the number of sample points is increased for the problem used for Figure 3-5. The

[9]The slight non-monotonicity in the convergence is due to the non-uniform distribution of the quadrature points. Sufficient number of quadrature points are necessary to capture all the details of the parameterization since the first-kind Fejér quadrature places more quadrature points at the ends.

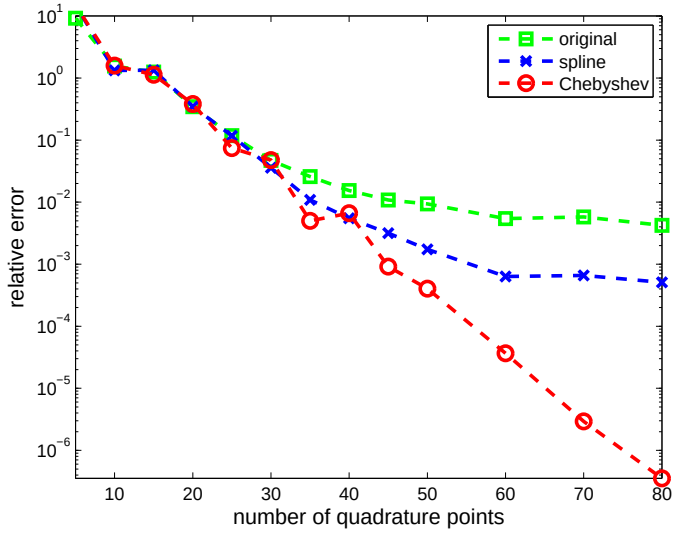

Figure 3-9: Relative error in the scattered field for different parameterizations of the interface.

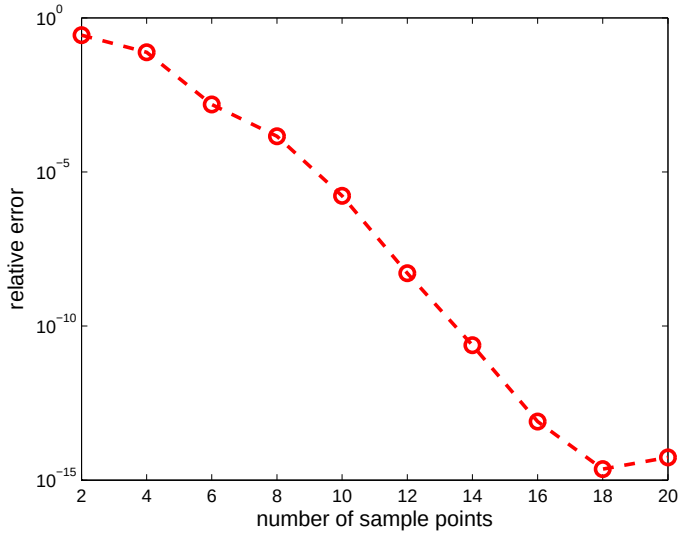

Figure 3-10: Relative error in the scattered field as the order of the Chebyshev interpolation is increased.

Chebyshev interpolation to the original parameterization (3.35) converges quickly since the parameterization is smooth. The same number of quadrature points, 20 per unknown equivalent source, is used for all the evaluations.

Chapter 4

Inverse Problem and Fast Jacobian Approximation

One of the key problems in differential or integral equation-based optimization is derivative evaluation. Analytic formulae for the derivatives are unknown in many cases, and numerical methods to approximate the derivatives can be very expensive [53, 54, 56].

However, if the inverse problem is formulated as a nonlinear least-square problem and solved with the Levenberg-Marquardt algorithm, only the Jacobian of the residual function is necessary [134, 135, 54]. Furthermore, if the forward problem is solved with a finite-difference or finite-element method, the cost of Jacobian approximation can be kept low with the adjoint method. The finite-difference and finite-element methods give sparse matrices whose entries are easy to evaluate [41, 42, 43, 44]. Therefore, the major cost of Jacobian evaluation is the cost of linear system solves, which is reduced to the cost of one linear solve with the adjoint method [56]. This has made the Levenberg-Marquardt algorithm with the adjoint method popular in practice, together with other quasi-Newton methods [135, 54, 53].

The adjoint method alone cannot reduce the cost of Jacobian evaluation sufficiently if integral equation methods are used for the forward analysis. Integral equation methods result in dense matrices, and the cost of evaluating the matrix entries is high, especially when Green's functions are difficult to evaluate. Therefore, reduction in the number of linear system solves by the adjoint method alone is insufficient to reduce to overall cost of Jacobian evaluation.

A fast method to approximate the Jacobian is proposed for shape optimization problems if the forward problem is solved by a Nyström method. The proposed method evaluates the Jacobian with a small number of additional Green's function evaluations, and the cost of the Jacobian evaluation is almost independent of the number of optimization variables when the cost of Green's function evaluation dominates. Therefore, the method is well-suited for shape-optimization problems with periodic structures. The proposed method outperforms the adjoint method alone when there are more than two optimization variables.

The spectrally convergent Nyström method in chapter 3 and the fast Jacobian evaluation method are used to identify the parameters characterizing a dielectric grating from the scattered fields. The inverse problem is posed as a nonlinear least-square problem and solved with the Levenberg-Marquardt algorithm, and the sensitivity of the estimates to the measurement noise is investigated as the number of sampled wavelengths is increased.

The rest of the chapter is organized as follows: section 4.1 summarizes the nonlinear least-square problem and the Levenberg-Marquardt algorithm, and section 4.2 presents the finite-difference and adjoint methods to approximate the Jacobian. The fast Jacobian approximation method is proposed in section 4.3. Finally, computational examples are shown in section 4.4.

4.1 The Nonlinear Least-Square Problem and the Levenberg-Marquardt Algorithm

The nonlinear least-square problem

$$\min_{\mathbf{p}} \quad ||\mathbf{y}(\mathbf{p}) - \mathbf{y}_m||_2^2 \tag{4.1}$$

is one way to estimate the values of interest $\mathbf{p} = (p_1, \cdots, p_{N_o})$ from some measured values $\mathbf{y}_m$ using a model $\mathbf{y}$ given by

$$\begin{aligned} \mathbf{A}(\mathbf{p})\mathbf{x}(\mathbf{p}) &= \mathbf{b}(\mathbf{p}) \\ \mathbf{y}(\mathbf{p}) &= \mathbf{C}(\mathbf{p})\mathbf{x}(\mathbf{p}). \end{aligned}$$

If integral equations are used for the forward analysis, $\mathbf{A}(\mathbf{p})\mathbf{x}(\mathbf{p}) = \mathbf{b}(\mathbf{p})$ is the discretized and tested integral equation, and $\mathbf{y}$ is found by applying an integral operator to the solution

of the integral equations. An example for 2-D dielectric scattering is shown in (3.33) and (3.34).

Some variants of the problem can be transformed into (4.1). If measurements are taken for more than one frequency, the corresponding nonlinear least-square problem is

$$\min_{\mathbf{p}} \sum_{m} \quad ||\mathbf{y}(\mathbf{p};\omega_m) - \mathbf{y}_m(\omega_m)||_2^2,$$

and it is transformed into (4.1) if

$$\begin{bmatrix} \mathbf{y}(\cdot;\omega_1) \\ \mathbf{y}(\cdot;\omega_2) \\ \vdots \end{bmatrix} \text{ and } \begin{bmatrix} \mathbf{y}_m(\omega_1) \\ \mathbf{y}_m(\omega_2) \\ \vdots \end{bmatrix}$$

are used for $\mathbf{y}$ and $\mathbf{y}_m$, respectively. Similarly, if $\mathbf{A}$, $\mathbf{b}$, or $\mathbf{C}$ is a complex-valued function,

$$\begin{bmatrix} \text{Re}\{\mathbf{y}\} \\ \text{Im}\{\mathbf{y}\} \end{bmatrix} \text{ and } \begin{bmatrix} \text{Re}\{\mathbf{y}_m\} \\ \text{Im}\{\mathbf{y}_m\} \end{bmatrix}$$

are used for $\mathbf{y}$ and $\mathbf{y}_m$, respectively, to naturally recover real $\mathbf{p}$ from the optimization problem.

The Levenberg-Marquardt algorithm is a popular method for solving nonlinear least-square problems. Given an initial guess $\mathbf{p}_0$, the algorithm iteratively improves the guess by solving a linearized problem with a trust-region constraint [134, 135, 54]. An update $\triangle\mathbf{p}_m$ for the current guess $\mathbf{p}_m$ is found by solving

$$\begin{aligned} \min_{\triangle\mathbf{p}_m} \quad & ||\mathbf{J}(\mathbf{p}_m)\triangle\mathbf{p}_m - (\mathbf{y}_m - \mathbf{y}(\mathbf{p}_m))||_2^2 \\ \text{subject to} \quad & ||\triangle\mathbf{p}_m|| \leq \delta_m, \end{aligned}$$

where $\mathbf{J}(\mathbf{p}_m)$ is the Jacobian of $\mathbf{y}$ at $\mathbf{p}_m$, and δ_m is the trust-region radius ensuring the accuracy of the linearization. Then, the improved guess is $\mathbf{p}_{m+1} = \mathbf{p}_m + \triangle\mathbf{p}_m$.

The Levenberg-Marquardt algorithm is reliable and efficient for a wide range of problems if δ_m is properly chosen [135, 54]. Even though the method makes quadratic-like approximation to the original objective function at each step, only the Jacobian of $\mathbf{y}$ in $\mathbf{p}$ is

required since the Hessian is approximated from the Jacobian[1]. This makes the algorithm attractive especially when the derivatives of the objective function have to be approximated numerically [135]. For more about the Levenberg-Marquardt algorithm, refer to [135, 54]. Different methods to control δ_m are shown mainly in [134, 135, 54].

4.2 Jacobian Evaluation via the Adjoint Method

The Jacobian of $\mathbf{y}$ can be assembled from the partial derivatives of $\mathbf{A}$, $\mathbf{b}$, and $\mathbf{C}$ in p_m, the mth optimization variable. The partial derivatives in p_m at $\mathbf{p}$ are

$$\begin{aligned}
\mathbf{A}_{p_m}(\mathbf{p}) &= \lim_{\alpha \to 0} \frac{\mathbf{A}(\mathbf{p} + \alpha \hat{e}_m) - \mathbf{A}(\mathbf{p})}{\alpha} \\
\mathbf{b}_{p_m}(\mathbf{p}) &= \lim_{\alpha \to 0} \frac{\mathbf{b}(\mathbf{p} + \alpha \hat{e}_m) - \mathbf{b}(\mathbf{p})}{\alpha} \\
\mathbf{C}_{p_m}(\mathbf{p}) &= \lim_{\alpha \to 0} \frac{\mathbf{C}(\mathbf{p} + \alpha \hat{e}_m) - \mathbf{C}(\mathbf{p})}{\alpha}
\end{aligned}$$

where $\hat{e}_m$ is the unit coordinate vector with one for the mth entry and zeros for the others. Then, the partial derivative of $\mathbf{y}$ in p_m at $\mathbf{p}$ is

$$\begin{aligned}
\mathbf{y}_{p_m}(\mathbf{p}) =& \mathbf{C}_{p_m}(\mathbf{p})\mathbf{x}(\mathbf{p}) + \mathbf{C}(\mathbf{p})\mathbf{x}_{p_m}(\mathbf{p}) \\
=& \mathbf{C}_{p_m}(\mathbf{p})\mathbf{x}(\mathbf{p}) + \mathbf{C}(\mathbf{p})\mathbf{A}^{-1}(\mathbf{p})[\mathbf{b}_{p_m}(\mathbf{p}) - \mathbf{A}_{p_m}(\mathbf{p})\mathbf{x}(\mathbf{p})],
\end{aligned} \tag{4.2}$$

and the Jacobian of $\mathbf{y}$ at $\mathbf{p}$ is simply

$$\mathbf{J}(\mathbf{p}) = [\mathbf{y}_{p_m}(\mathbf{p}) \cdots \mathbf{y}_{p_{N_o}}(\mathbf{p})]. \tag{4.3}$$

The adjoint method can reduce N_o linear solves in the Jacobian evaluation to one [56]. The adjoint problem

$$\mathbf{A}^T(\mathbf{p})\mathbf{W}(\mathbf{p}) = \mathbf{C}^T(\mathbf{p})$$

is solved once, and the solution $\mathbf{W}(\mathbf{p})$ is used repeatedly to evaluate all

$$\mathbf{y}_{p_m}(\mathbf{p}) = \mathbf{C}_{p_m}(\mathbf{p})\mathbf{x}(\mathbf{p}) + \mathbf{W}^T(\mathbf{p})[\mathbf{b}_{p_m}(\mathbf{p}) - \mathbf{A}_{p_m}(\mathbf{p})\mathbf{x}(\mathbf{p})] \tag{4.4}$$

[1]This can lead to slow convergence near a local minimum if the residual $\mathbf{y}(\mathbf{p}) - \mathbf{y}_m$ is large at the local minimum [135].

for $m = 1, \cdots, N_o$.

4.3 Fast Jacobian Evaluation

If $\mathbf{A}$ is a discretized integral operator, the adjoint method can still be expensive since (a) $\mathbf{A}_{p_m}$ is dense; and (b) the evaluation of $\mathbf{A}_{p_m}$ requires multiple Green's function or its derivative evaluations. This section proposes a fast method to evaluate $\mathbf{A}_{p_m}$ for shape optimization problems: $\mathbf{p}$ only affects the parameterization $\mathbf{q}(\cdot; \mathbf{p})$. The proposed method is similar to the sensitivity analysis method for isoparametric finite-element methods [56].

Methods to evaluate $\mathbf{S}_{p_m}$ and $\mathbf{K}'_{p_m}$ are developed since $\mathbf{A}_{p_m}$ is assembled from them as $\mathbf{A}$ is assembled from $\mathbf{S}$ and $\mathbf{K}'$. The partial derivative to $\mathbf{S}$, $\mathbf{S}_{p_m}$, is evaluated in two steps. First, the partial derivatives of $\mathbf{S}$ in the quadrature points are evaluated. In order to simplify the notation, x_n and y_n denote the x and y coordinates of the nth quadrature point $\mathbf{q}(\tau_{n/N_q})$. The x and y components of $\mathbf{q}'(\tau_{n/N_q})$ are denoted x'_n and y'_n. From (3.31), only the entries in the mth row and column of $\mathbf{S}$ change if either x_n or y_n is modified. This implies that $\mathbf{S}_{x_n}$ and $\mathbf{S}_{y_n}$ are sparse matrices with non-zero entries in the nth row and column only[2]. Similarly, the change in x'_n and y'_n only affects the mth row of $\mathbf{S}$, and $\mathbf{S}_{x'_n}$ and $\mathbf{S}_{y'_n}$ are sparse matrices with a non-zero nth row.

Then, the desired partial derivatives $\mathbf{S}_{p_m}$, $m = 1, 2, \cdots, N_o$, are assembled from $\mathbf{S}_{x_n}$, $\mathbf{S}_{y_n}$, $\mathbf{S}_{x'_n}$, and $\mathbf{S}_{y'_n}$, $m = 1, 2, \cdots, N_q$ via the chain rule:

$$\mathbf{S}_{p_m}(\mathbf{p}) = \sum_{n=1}^{N_q} [\mathbf{S}_{x_n}(\mathbf{p}) \frac{\partial x_n}{\partial p_m}(\mathbf{p}) + \mathbf{S}_{y_n}(\mathbf{p}) \frac{\partial y_n}{\partial p_m}(\mathbf{p}) + \mathbf{S}_{x'_n}(\mathbf{p}) \frac{\partial x'_n}{\partial p_m}(\mathbf{p}) + \mathbf{S}_{y'_n}(\mathbf{p}) \frac{\partial y'_n}{\partial p_m}(\mathbf{p})],$$

where $\partial x_n / \partial_m$ and $\partial y_n / \partial_m$ are the partial derivatives of the x and y components of $\mathbf{q}(\tau_{n/N_q}$ with respect to p_n. Similarly, $\partial x'_n / \partial_m$ and $\partial y'_n / \partial_m$ are those of $\mathbf{q}'(\tau_{n/N_q})$ with respect to p_n.

The method to evaluate $\mathbf{K}'_{p_m}$ is almost identical except that $\mathbf{K}'$ depends on $\mathbf{q}''(\tau_{n/N_q})$ as well. If the x and y components of $\mathbf{q}''(\tau_{n/N_q})$ are denoted x''_n and y''_n, respectively, $\mathbf{K}'_{x''_n}$

[2]The (n, n) entry is zero, to be more precise.

and $\mathbf{K}'_{y''_n}$ are sparse matrices with only the $(n,\, n)$ entry being non-zero. Therefore,

$$\mathbf{K}'_{p_m}(\mathbf{p}) = \sum_{n=1}^{N_q} [\mathbf{K}'_{x_n}(\mathbf{p}) \frac{\partial x_n}{\partial p_m}(\mathbf{p}) + \mathbf{K}'_{y_n}(\mathbf{p}) \frac{\partial y_n}{\partial p_m}(\mathbf{p}) + \mathbf{K}'_{x'_n}(\mathbf{p}) \frac{\partial x'_n}{\partial p_m}(\mathbf{p}) + \mathbf{K}'_{y'_n}(\mathbf{p}) \frac{\partial y'_n}{\partial p_m}(\mathbf{p}) + \mathbf{K}'_{x''_n}(\mathbf{p}) \frac{\partial x''_n}{\partial p_m}(\mathbf{p}) + \mathbf{K}'_{y''_n}(\mathbf{p}) \frac{\partial y''_n}{\partial p_m}(\mathbf{p})].$$

If the partial derivatives are not readily available, they are approximated by a finite-difference method. For instance, $\mathbf{A}_{p_m}$ at $\mathbf{p}$ is approximated by

$$\mathbf{A}_{p_m}(\mathbf{p}) \approx \frac{\mathbf{A}(\mathbf{p} + \alpha \hat{e}_m) - \mathbf{A}(\mathbf{p})}{\alpha},$$

where the rule of thumb to choose α is [134]

$$\triangle\alpha = \sqrt{\text{eps}}\, \text{sgn}(p_m) \max(|p_m|, 1);$$

eps is the machine epsilon for the floating point arithmetic [128]. A symmetric two-sided approximation is more accurate but doubles the number of additional function evaluations.

The number of additional Green's function evaluations is small and proportional to the number of quadrature points N_q, not to the number of optimization variables N_o. Evaluating the finite-difference approximations to $\mathbf{S}_{x_n}$, $\mathbf{S}_{y_n}$, $\mathbf{K}'_{x_n}$, and $\mathbf{K}'_{y_n}$ requires $2N_q$ Green's function evaluations in addition to what is required to evaluate the operators themselves. The other partial derivatives do not need any additional Green's function evaluation if the Green's function and its gradient values for the operator evaluations are reused. Therefore, evaluating all $\mathbf{S}_{p_m}$ and $\mathbf{K}'_{p_m}$ for $m = 1, \cdots, N_o$ takes $2N_q^2$ additional Green's function and $2N_q^2$ additional normal derivative evaluations. Since the evaluation of $\mathbf{S}$ needs N_q^2 Green's function evaluations, the additional cost to evaluate all $\mathbf{S}_{p_m}$ is just two additional operator evaluations. Similar argument applies to $\mathbf{K}'_{p_m}$ evaluations.

The number of quadrature points can be kept small if the Nyström method for forward analysis converges spectrally. Therefore, the method is ideal for optimization problems with many optimization variables when it is coupled with the method proposed in Chapter 3, or other spectrally convergent methods in [95, 96, 97, 98, 101, 99, 100, 50, 28].

4.4 Numerical Examples

First, the costs of evaluating the Jacobian with the finite-difference approximation and the proposed method are compared. A flat dielectric interface between two dielectric media is interpolated with cubic splines with increasing number of knots. The top medium is air, and the other medium is characterized by $12\epsilon_0$ and μ_0. The scattered field due the the incident field with wavelength λ_0 and incident angle $\pi/6$ is measured at $10\lambda_0$ distance from the interface in the $(\cos\pi/6, \sin\pi/6, 0)$, and the Jacobian of the scattered field with respect to the position of the knots is evaluated. Twenty quadrature points per unknown equivalent source is used for each evaluation.

Figure 4-1 shows the CPU time taken to evaluate the Jacobian with (4.2), (4.4), and the proposed method. The cost of the proposed method stays nearly constant since the cubic

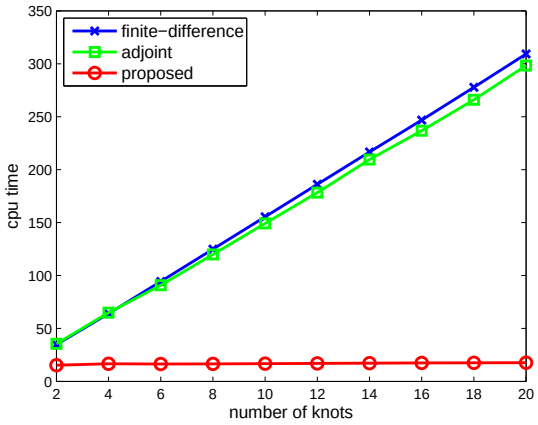

Figure 4-1: CPU time taken to evaluate the Jacobian.

spline parameterization is much more inexpensive to evaluate than the periodic Green's function. In contrast, the cost of using (4.2) and (4.4) grows linearly as the number of knots grows; the figure also shows that the cost of repeatedly solving the systems of linear equations with different right-hand sides for (4.2) is negligible compared to the cost of approximating the derivatives of the integral operators. The CPU time is evaluated with the *cputime* function in MATLAB.

The proposed method is applied to a dielectric grating identification problem. Consider a grating characterized by four parameters r_1, r_2, h, and w as shown in Figure 4-2. The media above and below are air and a dielectric material with permittivity $12\epsilon_0$ and permeability μ_0, and it is illuminated by a plane wave with an incident angle $\pi/6$.

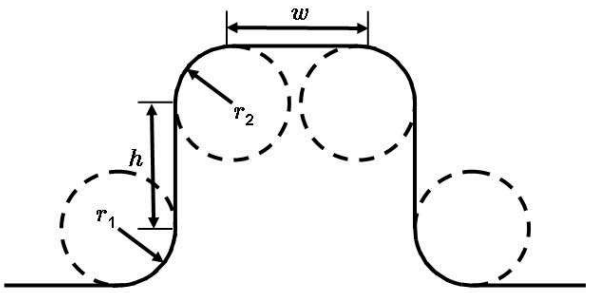

Figure 4-2: Parameterized grating to demonstrate the proposed method.

For a nominal wavelength λ_0, the period of the structure is $T = 1.3827\lambda_0$, and the nominal parameters are $r_{1,0} = 0.1T$, $r_{2,0} = 0.1T$, $h_0 = 0.8\lambda_0$, and $w_0 = 0.3T$. The test conditions for identifying a perturbed structure under the presence of measurement noise are

- The perturbed parameters r_1, r_2, h, and w can deviate from the nominal ones by $\pm 5\%$.
- The measurements are taken $10\lambda_0$ away from the surface in the $(\cos\pi/6, \sin\pi/6, 0)$ direction and contains $\pm 5\%$ measurement noise.
- Three different inverse problems with different numbers of incident wavelengths are considered: the first uses $1.25\lambda_0$; the second uses $1.25\lambda_0$ and $2\lambda_0$; and the third uses $1.25\lambda_0$, $1.62\lambda_0$, and $2\lambda_0$.
- The boundary is fitted with Chebyshev polynomials with 20 samples for the measurement simulation and forward analysis.
- The proposed Nyström method in Chapter 3 with 20 quadrature points is used for the measurement simulations and forward analysis.

Figure 4-3 shows the distribution of the relative errors in the estimated parameters from 100 measurements with different measurement noise for the same perturbed structure. The perturbed structure has $r_1 = 0.1046T$, $r_2 = 0.1015T$, $h = 0.7629\lambda_0$, and $w = 0.3105T$. The result shows that a reasonable estimation is possible even for a single wavelength measurement, but the sensitivity of the estimates to measurement noise is reduced if multiple wavelengths are used. The cost of using multiple wavelengths is longer forward analysis

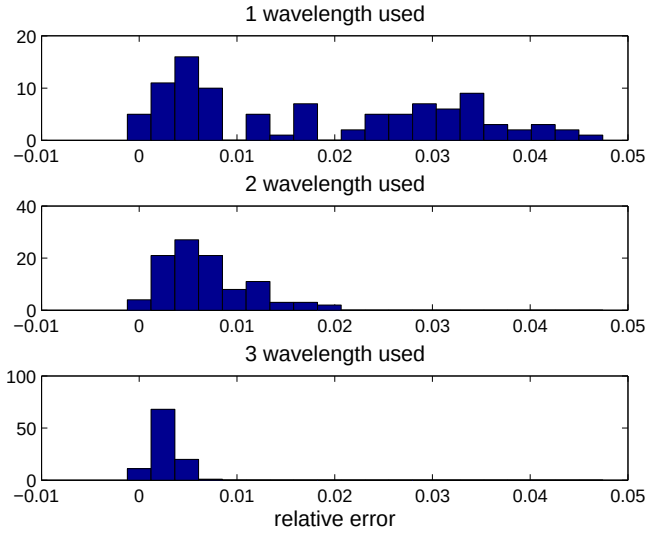

Figure 4-3: Noise sensitivity of the estimation.

time and the time to approximate the Jacobian, increasing linearly with the number of wavelengths.

Chapter 5

Panel Integration

Projection methods, such as collocation and Galerkin methods, are widely used to solve surface integral equations in 3-D [136, 137, 63, 28, 64, 138]. The projection methods are more versatile than the Nyström methods since only local approximations to the geometry and solution are necessary; they discretize the surface of a scatterer with panels and approximate the solution with basis functions.

Consider the 3-D mixed-potential operator in (2.29). If the electric and magnetic currents $\mathbf{J}$ and $\mathbf{M}$ are represented by a set of basis functions $\{\mathbf{b}_m\}$,

$$\mathbf{J}(\mathbf{r}) = \sum_m \alpha_m \mathbf{b}_m(\mathbf{r})$$
$$\mathbf{M}(\mathbf{r}) = \sum_m \beta_m \mathbf{b}_m(\mathbf{r})$$

with sets of weights $\{\alpha_m\}$ and $\{\beta_m\}$, the resulting fields are

$$\mathbf{E}(\mathbf{r};\mathbf{J},\mathbf{M}) = -jk\eta \sum_m \alpha_m (\mathbf{I}_1 \mathbf{b}_m)(\mathbf{r}) + \frac{\eta}{jk} \sum_m \alpha_m (\mathbf{I}_2 \mathbf{b}_m)(\mathbf{r}) - \sum_m \beta_m (\mathbf{I}_3 \mathbf{b}_m)(\mathbf{r})$$
$$\mathbf{H}(\mathbf{r};\mathbf{J},\mathbf{M}) = -j\frac{k}{\eta} \sum_m \beta_m (\mathbf{I}_1 \mathbf{b}_m)(\mathbf{r}) + \frac{1}{jk\eta} \sum_m \beta_m (\mathbf{I}_2 \mathbf{b}_m)(\mathbf{r}) + \sum_m \alpha_m (\mathbf{I}_3 \mathbf{b}_m)(\mathbf{r})$$

where

$$
\begin{aligned}
(\mathbf{I}_1\mathbf{b}_m)(\mathbf{r}) &= \int \mathbf{b}_m(\mathbf{r}')G(\mathbf{r},\mathbf{r}')\mathrm{d}\mathbf{r}' \\
(\mathbf{I}_2\mathbf{b}_m)(\mathbf{r}) &= \nabla \int [\nabla'_s \cdot \mathbf{b}_m(\mathbf{r}')]G(\mathbf{r},\mathbf{r}')\mathrm{d}\mathbf{r}' \\
(\mathbf{I}_3\mathbf{b}_m)(\mathbf{r}) &= \nabla \times \int \mathbf{b}_m(\mathbf{r}')G(\mathbf{r},\mathbf{r}')\mathrm{d}\mathbf{r}'
\end{aligned}
\tag{5.1}
$$

and

$$
G(\mathbf{r},\mathbf{r}') = \frac{e^{-jk||\mathbf{r}-\mathbf{r}'||}}{4\pi||\mathbf{r}-\mathbf{r}'||}.
$$

Therefore, accurate and efficient evaluation of the integrals $(\mathbf{I}_1\mathbf{b}_m)$, $(\mathbf{I}_2\mathbf{b}_m)$, and $(\mathbf{I}_3\mathbf{b}_m)$ are important for projection methods.

The integrals (5.1) for nearby- and self-interactions are difficult to evaluate since the Green's function is singular: it has a peak for $\mathbf{r} = \mathbf{r}'$. Conventional numerical quadratures for smooth functions converge slowly and become quickly expensive to achieve moderate accuracy. Therefore, efficient integration methods have been the subject of study for a long time [29, 139, 140, 30, 31, 141, 142, 143, 112, 144, 145, 113, 146, 74, 147, 148].

For the quasi-static case, closed-form formulae have been developed for constant and linear basis functions by various authors: [29, 139] propose change of variable methods, [31] presents a projection-based approach, and there are Gauss's theorem-based methods in [30, 142]. These formulae are highly accurate and efficient.

There is no analytic formula for full-wave analysis, and different mixtures of analytic and numerical quadrature techniques are used. Singularity extraction [141, 112, 113] and singularity cancellation [140, 143, 147, 148] methods are popular [149]. Alternative methods are dimension reduction schemes, where transformations are used to reduce area (volume) integrals over panels (volume elements) to line integrals over the edges [142, 144, 145, 146, 74]. The dimension reduction methods achieve (a) the ease of designing an efficient numerical quadrature; (b) high computational efficiency; and (c) good accuracy for most nearby- and self-interactions.

The existing methods do not converge spectrally for nearby- and self- interactions. Singularity extraction methods remove the dominant singularities only, and the discontinuity in the derivatives of the desingularized integrand slows the convergence of numerical quadratures. Singularity cancellation methods except [147] have problems with nearby-interactions

whose singularity is hard to cancel. Even though dimension reduction methods avoid problems with most nearby- and self-interactions, the methods converge poorly if the evaluation point is close to one of the edges; the integrands of the line integrals become nearly singular, slowing the numerical quadrature convergence [145].

This chapter proposes a change of variables to improve the convergence of the dimension reduction method when the evaluation point is close to an edge. The dimension reduction method reduces the area integrals into line integrals, and a change of variable based on a complex-domain mapping is used to integrate the resulting line integrals with spectral accuracy. As a result, the proposed method dramatically reduces the number of quadrature points to achieve a given accuracy and is effective for points close to a panel edge.

The Rao-Wilton-Glisson (RWG) basis function is reviewed in section 5.2. It is shown that the integrals in (5.1) for the RWG basis function can be assembled from three auxiliary integrals. Section 5.3 turns the auxiliary integrals into line integrals over the panel edges, and the proposed change of variables for the resulting line integrals is shown in section 5.4. Section 5.5 compares the accuracy and convergence of the proposed method with the singularity extraction method in [112], the singularity cancellation method in [147], and the edge-splitting method in [145].

The proposed method can be applied to any flat polygonal panel and volume elements [74] with straight edges even though only flat triangular panels are considered in this chapter. The material in this chapter is presented at the 2005 Design Automation Conference [74] and the 2008 International Microwave Symposium [150].

5.1 Notation

A flat triangular panel $\triangle$ is defined by three vertices denoted $\mathbf{v}_m$, $m = 1, 2, 3$, and $\mathbf{v}_4$ and $\mathbf{v}_0$ are defined to be $\mathbf{v}_1$ and $\mathbf{v}_3$, respectively, for the convenience of presentation. The edge opposite to $\mathbf{v}_m$ is the mth edge of the triangle, and it is characterized by a unit direction vector $\hat{\mathbf{l}}_m$ pointing from $\mathbf{v}_{m+1}$ to $\mathbf{v}_{m-1}$ and a unit direction vector $\hat{\mathbf{h}}_m$ pointing outward and in the plain containing the panel. Then, the normal direction of the panel is $\hat{\mathbf{n}} = \hat{\mathbf{h}}_m \times \hat{\mathbf{l}}_m$ for any m.

The point where the field or potential is evaluated is denoted $\mathbf{r}$, and $\mathbf{r}'$ is a point on $\triangle$. In addition, the projection of $\mathbf{r}$ to the plane containing the panel is denoted $\mathbf{r}^{\perp}$; $\boldsymbol{\rho}$ is the

vector from $\mathbf{r}^\perp$ and $\mathbf{r}'$ given by $\boldsymbol{\rho} = \mathbf{r}' - \mathbf{r}^\perp$, and d is the distance from $\mathbf{r}$ to $\mathbf{r}^\perp$ evaluated by $d = \hat{\mathbf{n}} \cdot (\mathbf{r}' - \mathbf{r})$. These symbols are summarized in Figure 5-1.

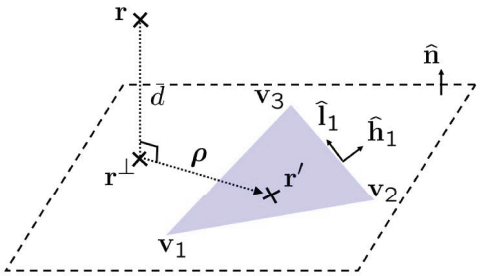

Figure 5-1: Panel coordinate system.

Some additional values in Figure 5-2 are defined to easily represent line integrals over an edge. Given $\mathbf{r}'$ on the mth edge, h_m is the distance from $\mathbf{r}^\perp$ to the edge, and l is the

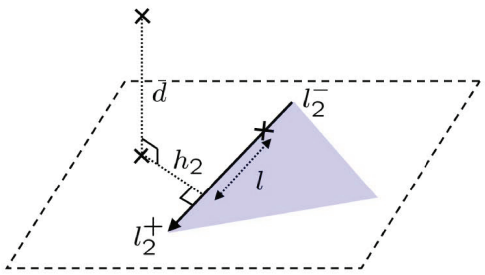

Figure 5-2: Edge coordinate system.

distance from the point on the edge closest to $\mathbf{r}$ (or $\mathbf{r}^\perp$, equivalently) to $\mathbf{r}'$. For an edge with $\hat{\mathbf{h}}_m$ and $\hat{\mathbf{l}}_m$, they are given by

$$\begin{aligned} h_m &= \hat{\mathbf{h}}_m \cdot (\mathbf{r}' - \mathbf{r}) \\ l &= \hat{\mathbf{l}}_m \cdot (\mathbf{r}' - \mathbf{r}). \end{aligned}$$

Note that h_m is the same for all $\mathbf{r}'$ on the edge.

5.2 The Rao-Wilton-Glisson Basis Function and Auxiliary Integrals

The Rao-Wilton-Glisson (RWG) basis function is a popular linear basis function to approximate both the electric and magnetic currents over a surface [136]. For an edge with length L, the RWG basis function for the edge shown in Figure 5-3 is

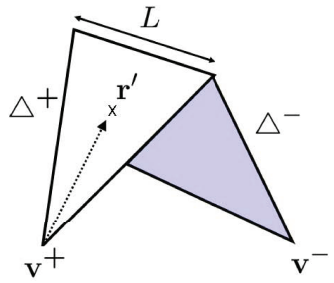

Figure 5-3: The Rao-Wilton-Glisson basis function.

$$\mathbf{b}^{\mathrm{RWG}}(\mathbf{r}') = \begin{cases} \dfrac{L}{2A^+}(\mathbf{r}' - \mathbf{v}^+), & \mathbf{r}' \in \triangle^+ \\ \dfrac{L}{2A^-}(\mathbf{v}^- - \mathbf{r}'), & \mathbf{r}' \in \triangle^- \end{cases}$$

where $A^\pm$ are the areas of the two flat triangular panels $\triangle^\pm$ sharing the edge, and $\mathbf{v}^\pm$ are the vertices of $\triangle^\pm$ opposite to the edge. The definition ensures that no charge accumulates at the edges and removes the need of line charges to satisfy (2.2) [136].

Evaluation of the field due to $\mathbf{b}^{\mathrm{RWG}}$ is performed panel-wise to save computation [136]. Given a panel $\triangle$, the integrals

$$\begin{aligned} (\mathbf{I}_1\mathbf{b}_m^{1/2})(\mathbf{r};\triangle) &= \int_\triangle \mathbf{b}_m^{1/2}(\mathbf{r}')G(\mathbf{r},\mathbf{r}')\mathrm{d}\mathbf{r}' \\ (\mathbf{I}_2\mathbf{b}_m^{1/2})(\mathbf{r};\triangle) &= \nabla \int_\triangle [\nabla_s' \cdot \mathbf{b}_m^{1/2}(\mathbf{r}')]G(\mathbf{r},\mathbf{r}')\mathrm{d}\mathbf{r}' \\ (\mathbf{I}_3\mathbf{b}_m^{1/2})(\mathbf{r};\triangle) &= \nabla \times \int_\triangle \mathbf{b}_m^{1/2}(\mathbf{r}')G(\mathbf{r},\mathbf{r}')\mathrm{d}\mathbf{r}' \end{aligned} \tag{5.2}$$

due to the half linear basis functions $\mathbf{b}_m^{1/2}(\mathbf{r}') = \mathbf{r}' - \mathbf{v}_m$, $m = 1, 2, 3$, are evaluated first, and $(\mathbf{I}_1\mathbf{b}^{\mathrm{RWG}})$, $(\mathbf{I}_2\mathbf{b}^{\mathrm{RWG}})$, and $(\mathbf{I}_3\mathbf{b}^{\mathrm{RWG}})$ are assembled from

$$(\mathbf{I}_1\mathbf{b}^{\mathrm{RWG}})(\mathbf{r}) = \frac{L}{2A^+}(\mathbf{I}_1\mathbf{b}_+^{1/2})(\mathbf{r};\triangle^+) - \frac{L}{2A^-}(\mathbf{I}_1\mathbf{b}_-^{1/2})(\mathbf{r};\triangle^-)$$

and similarly for the other two.

The integrals in (5.2) is simplified further by introducing auxiliary integrals [146]. The auxiliary integrals are

$$I(\mathbf{r};\triangle) = \frac{1}{4\pi}\int_{\triangle} G(\mathbf{r},\mathbf{r}')\mathrm{d}\mathbf{r}', \tag{5.3}$$

its gradient $\nabla I(\mathbf{r};\triangle)$, and

$$\mathbf{I}(\mathbf{r};\triangle) = \frac{1}{4\pi}\int_{\triangle} \boldsymbol{\rho} G(\mathbf{r},\mathbf{r}')\mathrm{d}\mathbf{r}'. \tag{5.4}$$

Then[1],

$$\begin{aligned}
(\mathbf{I}_1\mathbf{b}_m^{1/2})(\mathbf{r};\triangle) =& \mathbf{I}(\mathbf{r};\triangle) - (\mathbf{v}_m - \mathbf{r}^{\perp})I(\mathbf{r};\triangle)\\
(\mathbf{I}_2\mathbf{b}_m^{1/2})(\mathbf{r};\triangle) =& 2\nabla I(\mathbf{r};\triangle)\\
(\mathbf{I}_3\mathbf{b}_m^{1/2})(\mathbf{r};\triangle) =& (\mathbf{v}_m - \mathbf{r}) \times \nabla I(\mathbf{r};\triangle)
\end{aligned}$$

for $m = 1, 2, 3$. A different set of auxiliary integrals based on area (simplex) coordinates can be found in [136, 141].

5.3 Dimension Reduction

The auxiliary integrals over a flat triangular panel are transformed to line integrals over the edges using the Gauss' theorem [30, 112, 74]. Instead of using the general, and rather abstract, procedure in [142], we take a concrete approach using partial differential equations.

Reducing (5.3) to line integrals using the Gauss' theorem is equivalent to finding a particular solution to the partial differential equation

$$\nabla_s' \cdot \mathbf{f} = G(\mathbf{r},\mathbf{r}') = \frac{e^{-jk||\mathbf{r}'-\mathbf{r}||}}{||\mathbf{r}'-\mathbf{r}||}. \tag{5.6}$$

[1]The proof for the last relation is

$$\begin{aligned}
(\mathbf{I}_3\mathbf{b}_m^{1/2})(\mathbf{r};\triangle) =& \nabla \times \int_{\triangle} (\mathbf{r}' - \mathbf{v}_m) G(\mathbf{r},\mathbf{r}')\mathrm{d}\mathbf{r}'\\
=& \int_{\triangle} \nabla G(\mathbf{r},\mathbf{r}') \times [(\mathbf{r}' - \mathbf{r}) - (\mathbf{v}_m - \mathbf{r})]\mathrm{d}\mathbf{r}'\\
=& (\mathbf{v}_m - \mathbf{r}) \times \nabla \int_{\triangle} G(\mathbf{r},\mathbf{r}')\mathrm{d}\mathbf{r}'
\end{aligned} \tag{5.5}$$

where the vector identity $\nabla \times (a\mathbf{b}) = a(\nabla \times \mathbf{b}) + (\nabla a) \times \mathbf{b}$ is used.

It is convenient to write (5.6) in the cylindrical coordinates centered at $\mathbf{r}^{\perp}$, exploiting the radial symmetry of the right-hand side function. Assuming $\mathbf{f} = f_\rho \hat{\boldsymbol{\rho}}$ where $\hat{\boldsymbol{\rho}}$ is the direction of $\boldsymbol{\rho}$, (5.6) becomes

$$\frac{1}{\rho}\frac{\partial}{\partial \rho}(\rho f_\rho) = \frac{e^{-jk\sqrt{\rho^2+d^2}}}{\sqrt{\rho^2+d^2}}.$$

Such a choice of $\mathbf{f}$ is justified since only a particular solution is sought. Therefore, a particular solution to (5.6) is

$$\mathbf{f}(\boldsymbol{\rho}, d) = \frac{1}{-jk}\frac{e^{-jk\sqrt{\rho^2+d^2}}}{\rho}\hat{\boldsymbol{\rho}}.$$

Once a particular solution is found, Gauss' theorem is applied to (5.3) and

$$\begin{aligned} I(\mathbf{r}; \triangle) &= \frac{1}{4\pi}\Big[\int_{\triangle \setminus \bigcirc_\epsilon} G(\mathbf{r}, \mathbf{r}')\mathrm{d}\mathbf{r}' + \int_{\bigcirc_\epsilon} G(\mathbf{r}, \mathbf{r}')\mathrm{d}\mathbf{r}'\Big] \\ &= \frac{1}{4\pi}\Big[\int_{\partial(\triangle \setminus \bigcirc_\epsilon)} \frac{e^{-jk\sqrt{\rho^2+d^2}}}{-jk}\frac{\boldsymbol{\rho}\cdot\hat{\mathbf{h}}}{\rho^2}\mathrm{d}\mathbf{r}' + \int_{\bigcirc_\epsilon} G(\mathbf{r}, \mathbf{r}')\mathrm{d}\mathbf{r}'\Big] \end{aligned}$$

where $\bigcirc_\epsilon$[2] is the intersection of the radius ϵ circle centered at $\mathbf{r}^{\perp}$ with $\triangle$, $\partial(\triangle \setminus \bigcirc_\epsilon)$ is the boundary of $\triangle \setminus \bigcirc_\epsilon$, and $\hat{\mathbf{h}}$ is the in-plane unit outward direction of $\triangle \setminus \bigcirc_\epsilon$. Since this holds for any $\epsilon > 0$,

$$I(\mathbf{r}; \triangle) = \frac{1}{4\pi}\int_{\partial\triangle} \frac{e^{-jk\sqrt{\rho^2+d^2}} - e^{-jk|d|}}{-jk}\frac{\boldsymbol{\rho}\cdot\hat{\mathbf{h}}}{\rho^2}\mathrm{d}\mathbf{r}', \tag{5.7}$$

where $\partial\triangle$ is the boundary of $\triangle$.

The gradient of I is evaluated by [112, 141]

$$\nabla I(\mathbf{r}; \triangle) = \frac{\partial I}{\partial \hat{\mathbf{n}}}(\mathbf{r}; \triangle)\hat{\mathbf{n}} + \nabla_s I(\mathbf{r}; \triangle).$$

The normal derivative is found by directly differentiating (5.7),

$$\begin{aligned} \frac{\partial I}{\partial \hat{\mathbf{n}}}(\mathbf{r}; \triangle) =& \frac{1}{4\pi}\Big\{-\int_{\partial\triangle} \frac{d}{\sqrt{\rho^2+d^2}}\big[e^{-jk\sqrt{\rho^2+d^2}} - e^{-jk|d|}\big]\frac{\boldsymbol{\rho}\cdot\hat{\mathbf{h}}}{\rho^2}\mathrm{d}\mathbf{r}' \\ &+ e^{-jk|d|}\int_{\partial\triangle}\big[\mathrm{sgn}(d) - \frac{d}{\sqrt{\rho^2+d^2}}\big]\frac{\boldsymbol{\rho}\cdot\hat{\mathbf{h}}}{\rho^2}\mathrm{d}\mathbf{r}'\Big\} \end{aligned} \tag{5.8}$$

[2]The decomposition of $\triangle$ into $\triangle \setminus \bigcirc_\epsilon$ and $\bigcirc_\epsilon$ is necessary since the Gauss' theorem only applies to continuously differentiable functions [151].

where an analytic solution exists for the second integral for flat polygonal panels [30, 112]. The tangential gradient $\nabla_s I$ is converted to line integrals using Gauss' theorem [141, 112]:

$$\begin{aligned}\nabla_s I(\mathbf{r};\triangle) =& -\frac{1}{4\pi}\int_{\triangle}\nabla' G(\mathbf{r},\mathbf{r}')\mathrm{d}\mathbf{r}' \\ =& -\frac{1}{4\pi}\int_{\partial\triangle}\frac{e^{-jk\sqrt{\rho^2+d^2}}}{\sqrt{\rho^2+d^2}}\hat{\mathbf{h}}\mathrm{d}\mathbf{r}'.\end{aligned} \tag{5.9}$$

Finally, (5.4) can be reduced to

$$\mathbf{I}(\mathbf{r};\triangle) = \frac{1}{4\pi}\int_{\partial\triangle}\frac{e^{-jk\sqrt{\rho^2+d^2}}-1}{-jk}\hat{\mathbf{h}}\mathrm{d}\mathbf{r}', \tag{5.10}$$

following similar steps of solving

$$\nabla_s' f = \rho\frac{e^{-jk\sqrt{\rho^2+d^2}}}{\sqrt{\rho^2+d^2}}\hat{\boldsymbol{\rho}}$$

for f and applying Gauss' theorem.

5.4 Change of Variables

The mth edge integral of (5.7)

$$\frac{1}{4\pi}\int_{l_m^-}^{l_m^+}\frac{e^{-jk\sqrt{l^2+h_m^2+d^2}}-e^{-jk|d|}}{-jk}\frac{h_m}{l^2+h_m^2}\mathrm{d}l \tag{5.11}$$

has to be evaluated numerically, where l_m^- and l_m^+ are the ends of the edge given by

$$\begin{aligned}l_m^- =& \hat{\mathbf{l}}_m\cdot(\mathbf{v}_{m+1}-\mathbf{r}) \\ l_m^+ =& \hat{\mathbf{l}}_m\cdot(\mathbf{v}_{m-1}-\mathbf{r}).\end{aligned} \tag{5.12}$$

The factor $h_m/(l^2+h_m^2)$ generates a peak at $l=0$ if h_m is nearly zero and slows the convergence of numerical quadratures for smooth functions [145].

Faster convergence is possible with a change of variable motivated by a complex-domain mapping. The complex-domain mapping

$$g_1(t;\delta,\epsilon) = \delta + \epsilon\sinh[\frac{\alpha^+ + \alpha^-}{2}(t-1)+\alpha^-] \tag{5.13}$$

proposed in [152] with $\alpha^- = \text{asinh}(\frac{1-\delta}{\epsilon})$ and $\alpha^+ = \text{asinh}(\frac{1+\delta}{\epsilon})$ maps from $[-1,1]$ to $[-1,1]$ while moving the lines of singularity parallel to the real axis at $\pm\frac{\pi}{\alpha^- + \alpha^+}j$ to the lines of singularities from $(\delta+\epsilon j)$ to $(\delta+\infty j)$ and from $(\delta-\epsilon j)$ to $(\delta-\infty j)$ parallel to the imaginary axis. As a result, the ellipse of analyticity of the integrand is enlarged with a proper choice of δ and ϵ, and the numerical quadratures for smooth functions converge faster [114, 153].

To understand the effect of (5.13), Figure 5-4 shows the quadrature location l_n and weight w_n of the Gauss-Legendre quadrature on $[-1,1]$ and $g_1(l_n;0,0.01)$ and $g_1'(l_n;0,0.01)w_n$. The choice of δ and ϵ is made to compensate the dominant singularity at $\pm 0.01j$ for $[-1,1]$

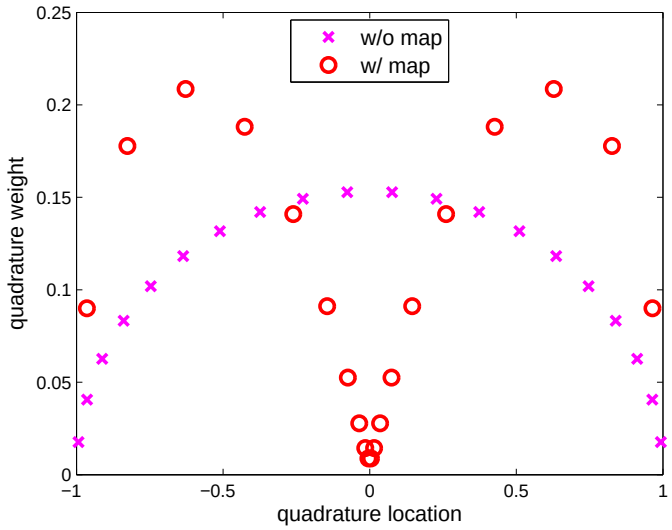

Figure 5-4: Quadrature location and weight for the Gauss-Legendre quadrature in l and the one in t mapped to l using g_1.

domain of integration. The mapped Gauss-Legendre quadrature automatically samples more near the peak, instead of the ends. Furthermore, the mapped quadrature does not weight the sampled integrand highly near the peak; this is a sensible thing to do since sampled value can have large errors near the peak.

To see the effect of the mapping, the left-hand side of

$$\int_{-1}^{1} \frac{h}{l^2+h^2} \mathrm{d}l = 2\tan^{-1}\frac{1}{h}$$

is evaluated numerically using Gauss-Legendre quadrature with and without g_1, and the relative error is plotted in Figure 5-5. Even though the relative errors reduce spectrally for

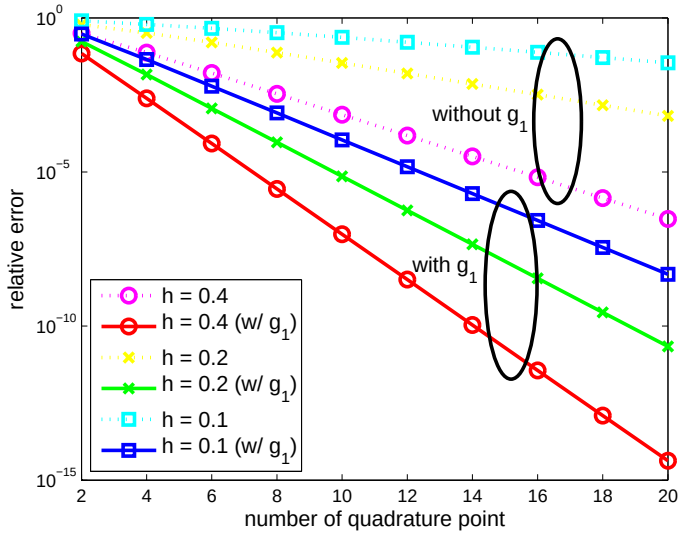

Figure 5-5: Relative error in numerically evaluating $\int_{-1}^{1} \frac{h}{l^2+h^2} \mathrm{d}l$ with and without g_1.

all the cases, the slopes become quickly gradual as the singularity at $\pm hj$ in the complex-domain approaches the domain of integration if no change of variable is used. The change of variable g_1 steepens the slope significantly.

The mapping (5.13) needs some modification before it can be applied to (5.11). First, a second mapping

$$g_2(t) = \frac{l_m^- + l_m^+}{2} t + \frac{l_m^+ - l_m^-}{2}$$

that maps $[-1, 1]$ to $[l_m^-, l_m^+]$ is necessary with

$$\delta = -\frac{l_m^+ + l_m^-}{l_m^+ - l_m^-}, \quad \epsilon = \frac{2h_m}{l_m^+ - l_m^-} \tag{5.14}$$

to place the resulting poles at $\pm h_m j$. Finally, we observed that the effect of poles at $\pm h_m j$ diminishes as d increases, and the mapping starts to slow the convergence of the numerical integration for large values of d. To avoid this problem, $\max(|h_m|, |d|)$ is used instead of h_m in (5.14)

Therefore, we propose to evaluate (5.11) as

$$\frac{1}{4\pi} \int_{-1}^{1} \frac{e^{-jk\sqrt{c_1^2(t)+h_m^2+d^2}} - e^{-jk|d|}}{-jk} \frac{h_m}{c_1^2(t) + h_m^2} c_1'(t) \mathrm{dt}$$

with

$$c_1(t) = g_2(g_1(t; -\frac{l_m^+ + l_m^-}{l_m^+ - l_m^-}, \frac{2\max(|h_m|, |d|)}{l_m^+ - l_m^-})). \tag{5.15}$$

The first integral of (5.8) has the same problem as (5.11), and the change of variable c_1 is applied to improve convergence.

In addition, a similar change of variable

$$c_2(t) = g_2(g_1(t; -\frac{l_m^+ + l_m^-}{l_m^+ - l_m^-}, \frac{2\sqrt{h_m^2 + d^2}}{l_m^+ - l_m^-})) \tag{5.16}$$

is applied to (5.9) and (5.10) to improve the rate of convergence even though the original integrands do not have any peak. The improvement comes from pushing the branch point at $l = \pm\sqrt{h_m^2 + d^2}$ away from the real axis and enlarging the ellipse of analyticity of the integrands. Usual numerical integration schemes for smooth functions, such as the Gauss-Legendre quadrature, are applied to the resulting integrals.

5.5 Numerical Examples

To show the effectiveness of the complex-domain mapping, the proposed method is compared with three existing methods. The first method is our implementation of the singularity extraction method proposed in [112] with the numerical cubature rules in [154, 155]. The second is our implementation of the line integration method with edge splitting in [145] using a Gauss-Legendre quadrature rule. The last is our implementation of the Khayat-Wilton transform method introduced in [147]. The proposed mapping method uses the Gauss-Legendre quadrature rule.

The comparison is made only for I since the rate of convergence of ∇I and $\mathbf{I}$ shows similar improvement with the change of variables in (5.15) and (5.16). Subsection 5.5.1 tests the self- and nearby-interactions using the same test cases used as in [144, 147]. The proposed method does not suffer from cancellation errors when distant interactions are computed, and it is shown in subsection 5.5.2. Finally, subsection 5.5.3 shows comparison between the proposed and singularity extraction methods for a lossy medium.

5.5.1 Self- and Nearby-Interactions

Figure 5-6 shows the panel and the three evaluation points at a given wavelength λ: $(0.01\lambda, 0.01\lambda, 0)$ and $(0.03\lambda, 0.03\lambda, 0)$ for a self interaction and $(0.01\lambda, 0.01\lambda, 0.01\lambda)$ for a nearby interaction.

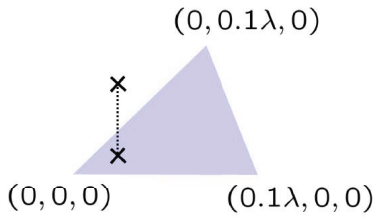

Figure 5-6: Test case used for self- and nearby-interactions.

Figure 5-7 shows the convergence of four different methods at $(0.01\lambda, 0.01\lambda, 0)$. The relative errors are computed with respect to the 14-digit reference values in Table II of [147]. The proposed method (solid line) shows a greater rate of convergence than all the existing methods. Note that achieving high accuracy is nearly impossible with the existing methods due to their slow convergence.

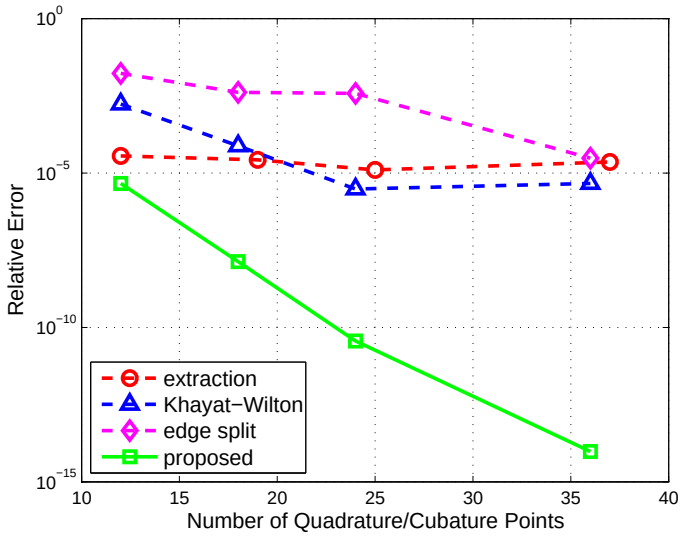

Figure 5-7: Convergence at $(0.01\lambda, 0.01\lambda, 0)$.

To see the difference between the edge splitting and complex-domain mapping method better, the convergence of the methods at $(0.03\lambda, 0.03\lambda, 0)$ is shown in Figure 5-8. The point

$(0.03\lambda, 0.03\lambda, 0)$ is close to the centroid of the triangle, and the edge-splitting methods shows a better convergence than the previous test case. By comparing Figure 5-7 and Figure 5-8, we can see that the convergence of the edge-splitting method depends on how close the evaluation point is to an edge, while the proposed method (solid line) shows robust convergence regardless of the evaluation point.

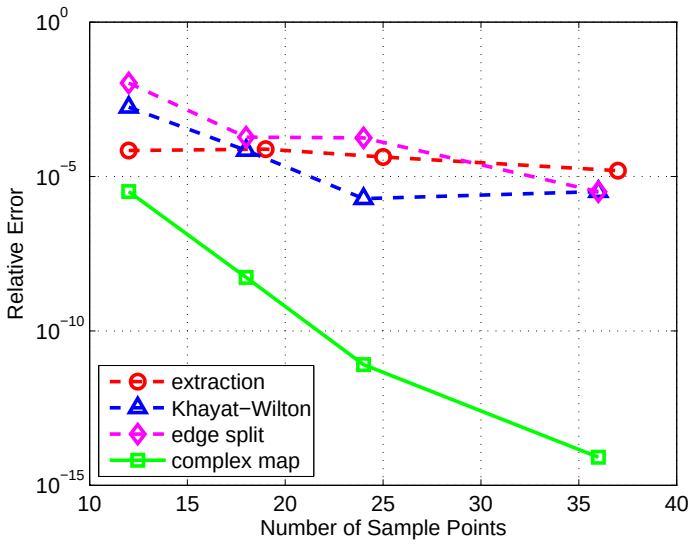

Figure 5-8: Convergence at $(0.03\lambda, 0.03\lambda, 0)$.

The nearby interactions are tested by lifting the evaluation point at $(0.01\lambda, 0.01\lambda, 0)$ to $(0.01\lambda, 0.01\lambda, 0.01\lambda)$. The convergence for the methods is shown in Figure 5-9 with respect to the reference values computed with the proposed method with 300 quadrature points. Again, the proposed method (solid line) shows rapid convergence and outperforms all other methods, even though the improvement is not as significant as in Figure 5-7.

Figure 5-10 shows the relative error of the methods while the evaluation point moves parallel to the x-axis through $(0, 0.05\lambda, 0)$ to test self- and nearby-interactions. One can see that the proposed method (solid line) achieves small relative error for all self- and nearby-evaluation points. As shown in Figure 5-7 and Figure 5-9, the proposed method converges much more quickly than the existing methods as the number of quadrature points grow. This is demonstrated again in Figure 5-11. Hence, the proposed method can easily meet high accuracy requirements, if necessary.

The reference values are computed with the proposed method using 300 quadrature

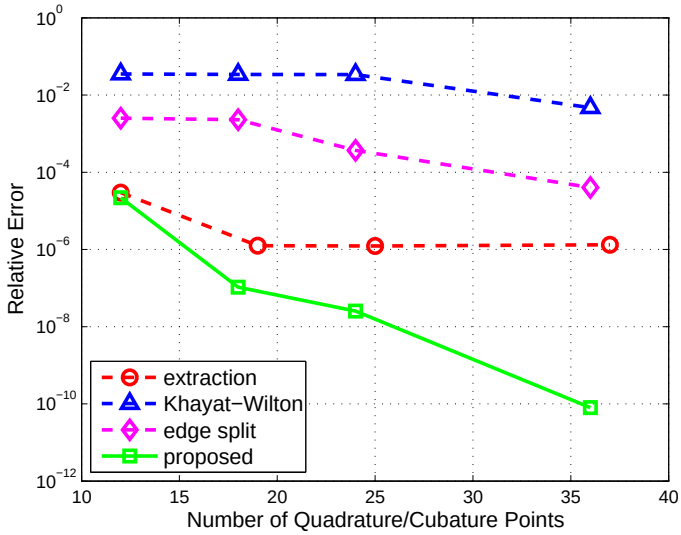

Figure 5-9: Convergence at $(0.01\lambda, 0.01\lambda, 0.01\lambda)$.

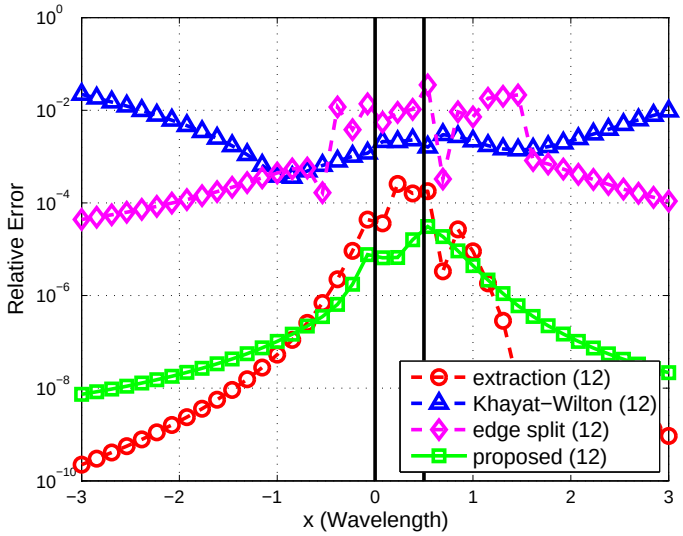

Figure 5-10: Moving the evaluation point on the plane, parallel to the x-axis.

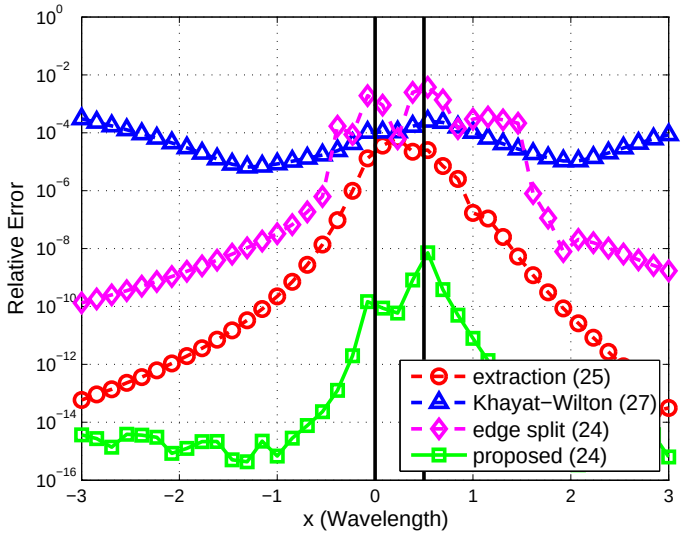

Figure 5-11: Approximately doubling the number of quadrature points.

number of quadrature	6	9	12	15	18
average	5.09e-5	6.93e-8	9.50e-11	5.76e-13	4.03e-13
maximum	4.03e-4	2.04e-6	9.69e-9	3.97e-11	3.75e-12

Table 5.1: Average and maximum relative error for different numbers of quadrature points.

points, and the Khayat-Wilton transform uses two quadrature points in Figure 5-10 and three quadrature points in Figure 5-11 for each radial and transverse direction. The vertical solid lines show the panel boundaries, and the numbers of quadrature points used for each method are shown in the legend.

5.5.2 Distant Interactions

To show that the proposed method does not suffer from cancellation errors for distant interactions, thousand random points distributed between distances of 0.3 wavelengths and ten wavelengths from the center of the panel are used to test the accuracy of the proposed method. The singularity extraction method with 37 cubature points is used to compute the reference values since singularity extraction methods are known to work well for distant interactions. Table 5.1 summarizes the average and the maximum relative errors for different numbers of quadrature points.

5.5.3 Lossy Media

To see the accuracy of the proposed method in lossy media, the frequency sweep test in [146] is performed with the same condition: panel vertices are at $(\alpha, -\alpha, 0)$, $(\alpha, \alpha/2, 0)$, and $(-2\alpha, \alpha/2, 0)$; and the evaluation point is placed at $(0, 0, \alpha)$ with $\alpha = 1e-3$[m] in copper medium ($\sigma = 5.8 \times 10^7$[Sm^{-1}]). For the reference, the proposed method is used while increasing the number of sample points until four consecutive values of I are the same up to 14 digits.

The relative error in I is shown in Figure 5-12. The proposed method is more robust to the increase in loss than the singularity extraction method. Furthermore, the accuracy of the proposed method improves significantly as the number of sample points is increased from nine to 15; the singularity extraction method performs better than the proposed for low loss and very small number of sample points.

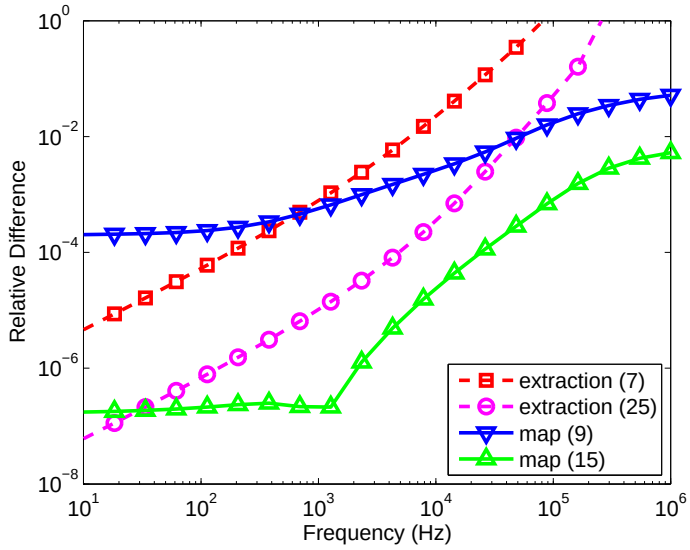

Figure 5-12: Relative error as a function of frequency in copper.

Chapter 6

Inverse Analysis with Parameterized Model Order Reduction

Solutions from projection methods usually converge more slowly than those from Nyström methods since projection methods make local and low-order approximation to either the geometry or the solution [28, 156, 157, 158]. Better rate of convergence can be achieved if the approximation to the geometry or the solution is improved [156, 157, 158]. Examples are curved panels for better geometry approximation [156, 158] and higher order basis functions for better approximation of the solution [157].

The rate of convergence of the projection methods is still linear even with these improvements. As a result, a larger system of linear equations, compared to the Nyström method, has to be solved for each forward analysis to meet the given accuracy requirements. Therefore, the overall inverse wave scattering analysis becomes considerably slower.

This chapter proposes a method that uses a parameterized reduced-order model to replace the forward analysis. Such a low-order model is called a proxy or a surrogate in some fields since it acts as a proxy for the original forward analysis [159, 160, 161], and the proposed method is similar to [162, 163, 164, 165, 166, 167, 168] in a sense since some computation is done before the optimization to improve the forward analysis efficiency.

Novel contributions are made in three ways: (a) the moment matching graph; (b) techniques to extend the polynomial-fit parameterized moment matching (PMM) to scattering

problems; and (c) a fast method to solve inverse wave scattering problems by coupling a parameterized reduced-order model and optimization. The result is a more efficient Jacobian evaluation as well as forward analysis.

First, the Galerkin method is used to discretize the PMCHW formulation in section 2.3, and the PMM and polynomial-fit PMM are summarized in section 6.2. The moment matching graph in section 6.3 generalizes the existing PMM and finds the condition on the projection matrix to match the moments when the system matrix is a polynomial function of the optimization variables. Section 6.4 presents extensions to the polynomial-fit PMM for scattering problems. A brief summary of the proposed method is given in section 6.5. Finally, Jacobian evaluation is explained in section 6.6, and the method is used to identify some discrete 3-D objects in section 6.7. This chapter is an extension to [169] presented at the 2005 International Microwave Symposium.

6.1 The PMCHW Formulation

Suppose the boundary of the scatterer is discretized, and the electric and magnetic currents are approximated by M Rao-Wilton-Glisson basis functions [136]

$$\mathbf{J}(\mathbf{r}) = \sum_{n=1}^{M} \alpha_n \mathbf{b}_n^{\mathrm{RWG}}(\mathbf{r})$$
$$\mathbf{M}(\mathbf{r}) = \sum_{n=1}^{M} \beta_n \mathbf{b}_n^{\mathrm{RWG}}(\mathbf{r}).$$

The fields due to the discretized currents using (2.29) are

$$\mathbf{E}(\mathbf{r};\mathbf{J},\mathbf{M}) = -jk\eta \sum_{n=1}^{M} \alpha_n (\mathbf{I}_1 \mathbf{b}_n^{\mathrm{RWG}})(\mathbf{r}) + \frac{\eta}{jk} \sum_{n=1}^{M} \alpha_n (\mathbf{I}_2 \mathbf{b}_n^{\mathrm{RWG}})(\mathbf{r}) - \sum_{n=1}^{M} \beta_n (\mathbf{I}_3 \mathbf{b}_n^{\mathrm{RWG}})(\mathbf{r})$$
$$\mathbf{H}(\mathbf{r};\mathbf{J},\mathbf{M}) = -j\frac{k}{\eta} \sum_{n=1}^{M} \beta_n (\mathbf{I}_1 \mathbf{b}_n^{\mathrm{RWG}})(\mathbf{r}) + \frac{1}{jk\eta} \sum_{n=1}^{M} \beta_n (\mathbf{I}_2 \mathbf{b}_n^{\mathrm{RWG}})(\mathbf{r}) + \sum_{n=1}^{M} \alpha_n (\mathbf{I}_3 \mathbf{b}_n^{\mathrm{RWG}})(\mathbf{r}).$$

where $(\mathbf{I}_1 \mathbf{b}_n^{\mathrm{RWG}})$, $(\mathbf{I}_2 \mathbf{b}_n^{\mathrm{RWG}})$, and $(\mathbf{I}_3 \mathbf{b}_n^{\mathrm{RWG}})$ are evaluated with the proposed method in chapter 5. The system of linear equations after discretizing and testing the PMCHW

formulation in (2.28) is

$$\begin{bmatrix} \eta^{\text{out}}\mathbf{L}^{\text{out}} + \eta^{\text{in}}\mathbf{L}^{\text{in}} & -\mathbf{K}^{\text{out}} - \mathbf{K}^{\text{in}} \\ \mathbf{K}^{\text{out}} + \mathbf{K}^{\text{in}} & \mathbf{L}^{\text{out}}/\eta^{\text{out}} + \mathbf{L}^{\text{in}}/\eta^{\text{in}} \end{bmatrix} \begin{bmatrix} \boldsymbol{\alpha} \\ \boldsymbol{\beta} \end{bmatrix} = - \begin{bmatrix} \mathbf{b}_E \\ \mathbf{b}_H \end{bmatrix} \tag{6.1}$$

where

$$\begin{aligned} L_{m,n} =& - jk \int \mathbf{b}_m^{\text{RWG}}(\mathbf{r}) \cdot (\mathbf{I}_1 \mathbf{b}_n^{\text{RWG}})(\mathbf{r}) \mathrm{d}\mathbf{r} + \frac{1}{jk} \int \mathbf{b}_m^{\text{RWG}}(\mathbf{r}) \cdot (\mathbf{I}_2 \mathbf{b}_n^{\text{RWG}})(\mathbf{r}) \mathrm{d}\mathbf{r} \\ K_{m,n} =& \int \mathbf{b}_m^{\text{RWG}}(\mathbf{r}) \cdot (\mathbf{I}_3 \mathbf{b}_n^{\text{RWG}})(\mathbf{r}) \mathrm{d}\mathbf{r} \\ b_{E,m} =& \int \mathbf{b}_m^{\text{RWG}}(\mathbf{r}) \cdot \mathbf{E}^i(\mathbf{r}) \mathrm{d}\mathbf{r} \\ b_{H,m} =& \int \mathbf{b}_m^{\text{RWG}}(\mathbf{r}) \cdot \mathbf{H}^i(\mathbf{r}) \mathrm{d}\mathbf{r} \end{aligned}$$

for $m, n = 1, \cdots, M$. The outer integrals are evaluated numerically without difficulty since the potential integrals behave reasonably [151]. Note that $\int \mathbf{b}_m^{\text{RWG}}(\mathbf{r}) \cdot (\mathbf{I}_2 \mathbf{b}_n^{\text{RWG}})(\mathbf{r}) \mathrm{d}\mathbf{r}$ can be simplified further by moving the gradient operator to the test basis function [136].

Once $\boldsymbol{\alpha}$ and $\boldsymbol{\beta}$ are found, the outside $\mathbf{E}$ at $\mathbf{r}$ is found by

$$\mathbf{E} = \mathbf{C} \begin{bmatrix} \boldsymbol{\alpha} \\ \boldsymbol{\beta} \end{bmatrix} \tag{6.2}$$

where the nth column $C_{:,n}$ of the 3-by-$2M$ matrix $\mathbf{C}$ is given by

$$\begin{aligned} C_{:,n} =& - jk\eta (\mathbf{I}_1 \mathbf{b}_n^{\text{RWG}})(\mathbf{r}) + \frac{\eta}{jk} (\mathbf{I}_2 \mathbf{b}_n^{\text{RWG}})(\mathbf{r}) \\ C_{:,M+n} =& (\mathbf{I}_3 \mathbf{b}_n^{\text{RWG}})(\mathbf{r}) \end{aligned}$$

for $n = 1, \cdots, M$.

6.2 Background for the Parameterized Moment Matching

6.2.1 The Parameterized Moment Matching

Consider a model

$$\begin{aligned}(\mathbf{A}_0 - \sum_{m=1}^{N_o} p_m \mathbf{A}_m)\mathbf{x}(\mathbf{p}) =& \mathbf{b} \\ \mathbf{y}(\mathbf{p}) =& \mathbf{C}\mathbf{x}(\mathbf{p})\end{aligned} \tag{6.3}$$

to compute $\mathbf{y}$ as a function of $\mathbf{p}$ where $\mathbf{A}_m$, $m = 0, \cdots, N_o$ are M-by-M matrices. Each evaluation of $\mathbf{y}(\mathbf{p})$ requires a linear system solve of size M-by-M, which can be expensive for models like (6.1) and (6.2).

An approximation to $\mathbf{y}$ is made using the PMM in [170, 171, 172, 173, 174, 175, 176]. The reduced system is

$$\begin{aligned}(\hat{\mathbf{A}}_0 - \sum_{m=1}^{N_o} p_m \hat{\mathbf{A}}_m)\hat{\mathbf{x}}(\mathbf{p}) =& \hat{\mathbf{b}} \\ \hat{\mathbf{y}}(\mathbf{p}) =& \hat{\mathbf{C}}\hat{\mathbf{x}}(\mathbf{p})\end{aligned} \tag{6.4}$$

with $\hat{\mathbf{A}}_m = \mathbf{V}^H \mathbf{A}_m \mathbf{V}$ for $m = 0, \cdots, N_o$, $\hat{\mathbf{b}} = \mathbf{V}\mathbf{b}$, and $\hat{\mathbf{C}} = \mathbf{C}\mathbf{V}$ for some M-by-m $\mathbf{V}$ with orthonormal columns. Hence, the evaluation of $\hat{\mathbf{y}}(\mathbf{p})$ requires a linear system solve of size m-by-m. In order for $\hat{\mathbf{y}}$ to approximate $\mathbf{y}$, the projection matrix $\mathbf{V}$ must be chosen carefully; the PMM in [170, 171, 172, 173, 174, 175, 176] chooses $\mathbf{V}$ so that the first few Taylor expansion coefficients of $\hat{\mathbf{y}}$ in $\mathbf{p}$ match those of $\mathbf{y}$, which is a generalization of the single parameter case in [177, 178, 179] and the references therein. The Taylor expansion coefficient are called moments due to the time domain interpretation [180].

For $\mathbf{A}$ that is a polynomial in $\mathbf{p}$, the products of parameters are re-defined to be independent parameters, and the PMM is applied to the resulting affine function with more parameters. Chapter 6.3 proposes a graph-based moment matching to determine $\mathbf{V}$ while incorporating the products of parameters without re-definition.

6.2.2 The Polynomial-Fit Parameterized Moment Matching

Consider a model

$$\begin{aligned} \mathbf{A}(\mathbf{p};\omega)\mathbf{x}(\mathbf{p};\omega) =& \mathbf{b}(\mathbf{p};\omega) \\ \mathbf{y}(\mathbf{p};\omega) =& \mathbf{C}(\mathbf{p};\omega)\mathbf{x}(\mathbf{p};\omega). \end{aligned} \tag{6.5}$$

as a function of optimization variables $\mathbf{p}$ and the angular frequency ω; an example is the discretized and tested PMCHW formulation in (6.1) and (6.2).

In practice, the functional dependence of $\mathbf{A}$ on $\mathbf{p}$ and ω is not known explicitly and unlikely to be a polynomial of $\mathbf{p}$ and ω. Therefore, the PMM in subsection 6.2.1 cannot be applied in its original form.

The polynomial-fit PMM in [174, 176] samples $\mathbf{A}(\mathbf{p}_m;\omega_m)$ for different $\mathbf{p}_m$'s and ω_m's and fits the entries of the sampled matrices with polynomials. For instance, the entry-by-entry polynomial fit $\tilde{\mathbf{A}}(\mathbf{p};\omega)$ to $\mathbf{A}(\mathbf{p};\omega)$ is

$$\tilde{\mathbf{A}}(\mathbf{p};\omega) = \tilde{\mathbf{A}}_0 - \sum_{m=1}^{N_o+1} p_m \tilde{\mathbf{A}}_m - \sum_{m=1}^{N_o+1} p_m p_n \tilde{\mathbf{A}}_{m,n} - \cdots \tag{6.6}$$

where $p_{N_o+1} = \omega$ for notational convenience. Then, the PMM can be applied [172, 174, 176].

6.2.3 Justification for Fitting Matrix Entries

The PMM or the polynomial-fit PMM is not the only method to find $\hat{\mathbf{y}}$. There are at least three different ways depending on when fitting occurs. In this subsection, these options are examined, and the use of the polynomial-fit PMM is justified for scattering problems.

First and the most straightforward method computes the response $\mathbf{y}(\mathbf{p}_m;\omega_m)$ for a number of different $\mathbf{p}_m$'s and ω_m's and constructs $\tilde{\mathbf{y}}$ as polynomial or rational fit.[181]. The memory footprint is small since only 3-by-1 vectors of $\mathbf{y}(\mathbf{p}_m;\omega_m)$ have to be stored, but most of the information from the forward analysis is lost. Examples are [181, 182, 183].

The polynomial-fit PMM explained in subsection 6.2.2 is the other extreme. The method tries to use all the information gathered from the boundary element analysis and requires a large amount of memory to store sampled M-by-M matrices. The third method fits the surface currents $\mathbf{x}$, and it is a compromise between the first and the second methods.

In addition to the memory footprint, the ease of polynomial or rational fit should be

considered since fitting a highly nonlinear function is known to be difficult, especially if the function oscillates or has peaks, such as $\mathbf{y}$ from (6.1) and (6.2) [184, 19]. Furthermore, $\mathbf{x}$ is an even stronger nonlinear function than $\mathbf{y}$ since $\mathbf{C}$ in (6.2) smoothens $\mathbf{x}$ to compute $\mathbf{y}$. In contrast, the entries of $\mathbf{A}$, $\mathbf{C}$, and $\mathbf{b}$ are averaged potentials and fields as functions of the parameters. Therefore, the polynomial-fit PMM is the most reasonable choice for optical scattering problems.

6.3 The Moment Matching Graph

An alternative method to construct $\mathbf{V}$ for a polynomial $\mathbf{A}$ in $\mathbf{p}$ without re-defining products of parameters as independent ones is proposed. Even though there is a more general method for an arbitrary $\mathbf{A}$ [171, 173, 175], the proposed method has its own advantage: it is specialized for polynomials and graphical. The sufficient condition for $\mathbf{V}$ to match moments of $\mathbf{y}$ is identified by traversing the corresponding moment matching graph and collecting the node values. Furthermore, the method identifies the condition to match a single moment instead of all the moments of the same order. The proposed method is used in [185] to gain insight into the PMM and to reduce computation for large number of parameters.

For the convenience of the notation, let us define $\mathbf{p}^{\mathbf{m}} = p_1^{m_1} \cdots p_{N_o}^{m_{N_o}}$. The inequalities on m are interpreted elementwise, e.g.

$$\mathbf{m} \geq 0 \Leftrightarrow m_n \geq 0, \quad n = 1, \cdots, N_o.$$

Given a set $\mathcal{I}$ of non-negative vectors of dimension N_o excluding $\mathbf{0}$, the proposed algorithm reduces

$$\begin{aligned} (\mathbf{A_0} - \sum_{\mathbf{m}\in\mathcal{I}} \mathbf{p}^{\mathbf{m}}\mathbf{A_m})\mathbf{x}(\mathbf{p}) =& \mathbf{b} \\ \mathbf{y}(\mathbf{p}) =& \mathbf{C}\mathbf{x}(\mathbf{p}) \end{aligned} \tag{6.7}$$

with an invertible $\mathbf{A_0}$ to

$$\begin{aligned} (\hat{\mathbf{A}}_\mathbf{0} - \sum_{\mathbf{m}\in\mathcal{I}} \mathbf{p}^{\mathbf{m}}\hat{\mathbf{A}}_\mathbf{m})\hat{\mathbf{x}}(\mathbf{p}) =& \hat{\mathbf{b}} \\ \hat{\mathbf{y}}(\mathbf{p}) =& \hat{\mathbf{C}}\hat{\mathbf{x}}(\mathbf{p}) \end{aligned} \tag{6.8}$$

with

$$\begin{aligned}\hat{\mathbf{A}}_{\mathbf{m}} =& \mathbf{V}^H\mathbf{A}\mathbf{V}, \quad \mathbf{m} \in \{\mathbf{0}\} \cup \mathcal{I} \\ \hat{\mathbf{b}} =& \mathbf{V}^H\mathbf{b} \\ \hat{\mathbf{C}} =& \mathbf{C}\mathbf{V},\end{aligned} \tag{6.9}$$

for some M-by-m matrix $\mathbf{V}$ with orthonormal columns while matching the first few Taylor expansion coefficients of $\hat{\mathbf{y}}$ in $\mathbf{p}$ with those of $\mathbf{y}$.

6.3.1 Construction of the Moment Matching Graph

The moment matching graph is completely characterized by a set of nodes

$$\mathcal{N} = \{(m_1, \cdots, m_{N_o}) \geq 0\},$$

a set of directed edges $\mathcal{E}$, and the node values $\mathbf{v}_{\mathbf{m}}$ associated with the node $\mathbf{m}$ in $\mathcal{N}$. Given $\mathcal{I}$, the set of edges are given by

$$\mathcal{E} = \{(\mathbf{n}, \mathbf{m}) : \mathbf{m} - \mathbf{n} \in \mathcal{I}\},$$

and the node values are determined by the following rule:

1. $\mathbf{v_0} = \mathbf{A_0^{-1}}\mathbf{b}$.

2. If $\mathbf{m}$ is not $\mathbf{0}$,

$$\mathbf{v}_{\mathbf{m}} = \begin{cases} 0, & \text{if no edge entering} \\ \displaystyle\sum_{\mathbf{n}:\ \mathbf{m}-\mathbf{n}\in\mathcal{I}} (\mathbf{A_0^{-1}}\mathbf{A}_{\mathbf{m}-\mathbf{n}})\mathbf{v}_{\mathbf{n}}, & \text{otherwise.} \end{cases} \tag{6.10}$$

For example, consider

$$\begin{aligned}(\mathbf{A}_{(0,0)} - p_1\mathbf{A}_{(1,0)} - p_1^2\mathbf{A}_{(2,0)} - p_1p_2\mathbf{A}_{(1,1)})\mathbf{x}(\mathbf{p}) =& \mathbf{b} \\ \mathbf{y}(\mathbf{p}) =& \mathbf{C}\mathbf{x}(\mathbf{p}).\end{aligned} \tag{6.11}$$

Then, $\mathcal{I} = \{(1,0), (2,0), (1,1)\}$, and the corresponding moment matching graph for $||\mathbf{m}||_1 \leq 3$, $\mathbf{m} \in \mathcal{N}$ is shown in Figure 6-1. For this moment matching graph,

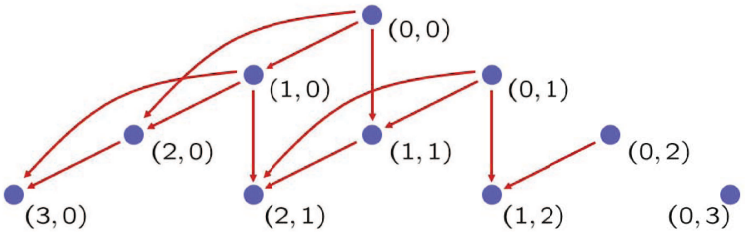

Figure 6-1: Moment matching graph for (6.11).

$$
\begin{aligned}
\mathcal{N} =& \{(0,0),(1,0),(0,1),(2,0),(1,1),(0,2),(3,0),(2,1),(1,2),(0,3),\cdots\} \\
\mathcal{E} =& \{((0,0),(1,0)),((0,0),(2,0)),((0,0),(1,1)), \\
& ((1,0),(2,0)),((1,0),(3,0)),((1,0),(2,1)),\cdots\},
\end{aligned}
$$

and the node values are

$$
\begin{aligned}
\mathbf{v}_{(0,0)} =& \breve{\mathbf{b}} \\
\mathbf{v}_{(1,0)} =& \breve{\mathbf{A}}_{(1,0)}\breve{\mathbf{b}} \\
\mathbf{v}_{(0,1)} =& \mathbf{0} \\
\mathbf{v}_{(2,0)} =& [\breve{\mathbf{A}}_{(2,0)} + \breve{\mathbf{A}}^2_{(1,0)}]\breve{\mathbf{b}} \\
\mathbf{v}_{(1,1)} =& \breve{\mathbf{A}}_{(1,1)}\breve{\mathbf{b}} \\
\mathbf{v}_{(0,2)} =& \mathbf{0} \\
\mathbf{v}_{(3,0)} =& [\breve{\mathbf{A}}_{(1,0)}\breve{\mathbf{A}}_{(2,0)} + \breve{\mathbf{A}}^3_{(1,0)} + \breve{\mathbf{A}}_{(2,0)}\breve{\mathbf{A}}_{(1,0)}]\breve{\mathbf{b}} \\
\mathbf{v}_{(2,1)} =& [\breve{\mathbf{A}}_{(1,1)}\breve{\mathbf{A}}_{(1,0)} + \breve{\mathbf{A}}_{(1,0)}\breve{\mathbf{A}}_{(1,1)}]\breve{\mathbf{b}} \\
\mathbf{v}_{(1,2)} =& \mathbf{0} \\
\mathbf{v}_{(0,3)} =& \mathbf{0}
\end{aligned}
$$

where

$$
\begin{aligned}
\breve{\mathbf{b}} =& (\mathbf{A}^{-1}_{(0,0)}\mathbf{b}) \\
\breve{\mathbf{A}}_{\mathbf{m}} =& \mathbf{A}^{-1}_{(0,0)}\mathbf{A}_{\mathbf{m}}
\end{aligned}
\tag{6.12}
$$

are used for brevity.

6.3.2 Properties of the Moment Matching Graph

The moment matching graph can be used to evaluate the moments of $\mathbf{x}$ in $\mathbf{p}$ explicitly. For instance, consider the example in (6.11). With Neumann expansion,

$$\begin{aligned}\mathbf{x}(\mathbf{p}) =&(\mathbf{A}_{(0,0)} - p_1\mathbf{A}_{(1,0)} - p_1^2\mathbf{A}_{(2,0)} - p_1p_2\mathbf{A}_{(1,1)})^{-1}\mathbf{b}\\ =&(\mathbf{I} - p_1\breve{\mathbf{A}}_{(1,0)} - p_1^2\breve{\mathbf{A}}_{(2,0)} - p_1p_2\breve{\mathbf{A}}_{(1,1)})^{-1}\breve{\mathbf{b}}\\ =&\sum_{m=0}^{\infty}(p_1\breve{\mathbf{A}}_{(1,0)} - p_1^2\breve{\mathbf{A}}_{(2,0)} - p_1p_2\breve{\mathbf{A}}_{(1,1)})^m\breve{\mathbf{b}}\\ =&\mathbf{v}_{(0,0)} + p_1\mathbf{v}_{(1,0)} + p_1^2\mathbf{v}_{(2,0)} + p_1p_2\mathbf{v}_{(1,1)} + p_1^3\mathbf{v}_{(3,0)} + p_1^2p_2\mathbf{v}_{(2,1)} + \cdots\end{aligned} \tag{6.13}$$

where the simplified notation in (6.12) is used.

This property is of little value in practice [177, 178], but it is summarized in the following Lemma since it is used to prove the moment matching property of the graph.

Lemma 6.3.1. *Given $\mathcal{I}$,*

$$(\mathbf{A_0} - \sum_{\mathbf{m}\in\mathcal{I}}\mathbf{p^m}\mathbf{A_m})^{-1}\mathbf{b} = \sum_{\mathbf{m}\in(\mathcal{Z}_0^+)^{No}}\mathbf{p^m}\mathbf{v_m} \tag{6.14}$$

where $\mathbf{v_m}$ is the node value in (6.10), and $\mathcal{Z}_0^+$ is the set of non-negative integers.

Proof. The proof is based on the strong mathematical induction, and the coefficient multiplying $\mathbf{p^m}$ is denoted $\mathbf{w_m}$. The Lemma holds trivially for $\mathbf{w_0} = \mathbf{v_0} = \mathbf{A_0^{-1}b}$. Suppoe $\mathbf{w_l} = \mathbf{v_l}$ for all $\mathbf{l}$, $||\mathbf{l}||_1 < m$: From Neumann expansion, $\mathbf{w_m p^m}$ with $||\mathbf{m}||_1 = m$ is part of

$$(\sum_{\mathbf{n}\in\mathcal{I}}\mathbf{A_0^{-1}A_n p^n})(\sum_{||\mathbf{l}||_1<m}\mathbf{w_l p^l})$$

or

$$\mathbf{w_m} = \sum_{\mathbf{n}:\ \mathbf{m-n}\in\mathcal{I}}(\mathbf{A_0^{-1}A_n})\mathbf{w_n} = \sum_{\mathbf{n}:\ \mathbf{m-n}\in\mathcal{I}}(\mathbf{A_0^{-1}A_n})\mathbf{v_n},$$

which is exactly how the node values are evaluated. This concludes the proof. □

Consider the moment matching graphs for (6.7) and (6.8). The node and edge sets of the two graphs are identical, and the nodes values are denoted $\mathbf{v_m}$ for (6.7) and $\hat{\mathbf{v}}_\mathbf{m}$ for (6.8). The following is the key Theorem to establish the moment matching property of the graph.

Theorem 6.3.2. *Given* $\mathbf{m}$*, if* $\mathbf{V}$ *with orthonormal columns satisfies* $\mathbf{v_m} \in colsp(\mathbf{V})$ *and*

$$\begin{aligned} \mathbf{V}^H\mathbf{v_n} =& \hat{\mathbf{v}}_\mathbf{n} \\ \mathbf{v_n} \in& colsp(\mathbf{V}) \end{aligned} \tag{6.15}$$

for all $\mathbf{n}$ *satisfying* $\mathbf{m} - \mathbf{n} \in \mathcal{I}$*,*

$$\mathbf{V}^H\mathbf{v_m} = \hat{\mathbf{v}}_\mathbf{m}. \tag{6.16}$$

Proof. For $\mathbf{m} = \mathbf{0}$,

$$\begin{aligned} \hat{\mathbf{v}}_\mathbf{0} =& (\mathbf{V}^H\mathbf{A_0}\mathbf{V})^{-1}\mathbf{V}^H\mathbf{b} \quad (6.9) \\ =& (\mathbf{V}^H\mathbf{A_0}\mathbf{V})^{-1}\mathbf{V}^H\mathbf{A_0}\mathbf{v_0} \\ =& \mathbf{V}^H\mathbf{v_0} \end{aligned} \tag{6.17}$$

since $\mathbf{V}\mathbf{V}^H\mathbf{v_0} = \mathbf{v_0}$ for any $\mathbf{v_0} \in \text{colsp}(\mathbf{V})$. Similarly,

$$\begin{aligned} \hat{\mathbf{v}}_\mathbf{m} =& \hat{\mathbf{A}}_\mathbf{0}^{-1} \sum_{\mathbf{n}:\ \mathbf{m}-\mathbf{n}\in\mathcal{I}} \hat{\mathbf{A}}_{\mathbf{m}-\mathbf{n}}\hat{\mathbf{v}}_\mathbf{n} \quad (6.10) \\ =& (\mathbf{V}^H\mathbf{A_0}\mathbf{V})^{-1} \sum_{\mathbf{n}:\ \mathbf{m}-\mathbf{n}\in\mathcal{I}} (\mathbf{V}^H\mathbf{A}_{\mathbf{m}-\mathbf{n}}\mathbf{V})\mathbf{V}^H\mathbf{v_n} \quad (6.9) \text{ and } (6.15) \\ =& (\mathbf{V}^H\mathbf{A_0}\mathbf{V})^{-1}\mathbf{V}^H \sum_{\mathbf{n}:\ \mathbf{m}-\mathbf{n}\in\mathcal{I}} \mathbf{A}_{\mathbf{m}-\mathbf{n}}\mathbf{v_n} \\ =& (\mathbf{V}^H\mathbf{A_0}\mathbf{V})^{-1}\mathbf{V}^H\mathbf{A_0}\mathbf{v_m} \quad (6.10) \\ =& \mathbf{V}^H\mathbf{v_m} \end{aligned}$$

for $\mathbf{m}$ not equal to $\mathbf{0}$. □

The moment matching property of the graph is a direct consequence of Theorem 6.3.2. Note that similar insights are used in [176, 186].

Corollary 6.3.3. *If the condition in Theorem 6.3.2 holds, the* $\mathbf{m}$ *moments of* $\mathbf{y}$ *and* $\hat{\mathbf{y}}$ *are matched.*

Proof.

$$\begin{aligned} \hat{\mathbf{C}}\hat{\mathbf{v}}_\mathbf{m} =& \mathbf{C}\mathbf{V}\mathbf{V}^H\mathbf{v_m} \\ =& \mathbf{C}\mathbf{v_m} \end{aligned} \tag{6.18}$$

since $\mathbf{v_m} \in \text{colsp}(\mathbf{V})$. □

As a result, the condition to match the $\mathbf{m}$ moments is found by traversing the moment matching graph of the original system backward from node $\mathbf{m}$ to node $\mathbf{0}$ and collecting the node values. For instance, the condition to match the $(2,1)$ moment for (6.11) is

$$\{\mathbf{v}_{(2,1)}, \mathbf{v}_{(1,1)}, \mathbf{v}_{(1,0)}, \mathbf{v}_{(0,0)}\} \in \text{colsp}(\mathbf{V}).$$

6.4 Improvements to the Polynomial-Fit Parameterized Moment Matching

In this section, we investigate the additional issues related to (a) fitting $\mathbf{C}(\mathbf{p}_m; \omega_m)$ with respect to ω and (b) constructing $\mathbf{V}$ when $\mathbf{b}$ also depends on $\mathbf{p}$ and $\omega$are investigated.

6.4.1 Fitting in Frequency

For the structures of interest, the size of the scattering surface is of the order of a wavelength, while the measurement point is usually a number of wavelengths away. Under this setting, the entries of $\mathbf{C}$ are strong nonlinear functions of ω that oscillates. This can be seen from the 3-D Green's function,

$$G(\mathbf{r}, \mathbf{r}') = \frac{e^{-j\omega\sqrt{\epsilon\mu}||\mathbf{r}'-\mathbf{r}||}}{4\pi||\mathbf{r}'-\mathbf{r}||},$$

which rapidly oscillates even with a small change in ω when $||\mathbf{r}-\mathbf{r}'||$ is large.

Polynomial fitting is not accurate for oscillating functions; to improve the accuracy of the fit, a nominal distance is factored out. Assume that there is a cluster of panels distributed within a range smaller than ω, and let the center of the cluster be $\mathbf{r}_0$. By factoring out $||\mathbf{r}_0-\mathbf{r}||$, G becomes

$$\begin{aligned} G(\mathbf{r}, \mathbf{r}') &= e^{-j\omega\sqrt{\epsilon\mu}||\mathbf{r}_0-\mathbf{r}||}\frac{e^{-j\omega\sqrt{\epsilon\mu}(||\mathbf{r}'-\mathbf{r}||-||\mathbf{r}_0-\mathbf{r}||)}}{4\pi||\mathbf{r}'-\mathbf{r}||} \\ &= e^{-j\omega\sqrt{\epsilon\mu}||\mathbf{r}_0-\mathbf{r}||}G'(\mathbf{r}, \mathbf{r}') \end{aligned}$$

and $(||\mathbf{r}'-\mathbf{r}|| - ||\mathbf{r}_0-\mathbf{r}||)$ in G' remains small. Hence, G' no longer oscillates and is fitted easily with a polynomial. A generalization of the idea can be found in [187].

6.4.2 Removing Parameter Dependency of b

For the scattering problem, the input $\mathbf{b}$ is a function of $\mathbf{p}$ and ω since the integrals of the incident fields change as the scattering surface or the frequency changes. Even after $\mathbf{b}$ is approximated with an entry-by-entry polynomial fit, the PMM cannot be applied to find $\mathbf{V}$ since the PMM assumes that $\mathbf{b}$ is a constant.

A modification to $\tilde{\mathbf{A}}$, $\tilde{\mathbf{b}}$, and $\tilde{\mathbf{C}}$ is proposed to have a constant right-hand side vector. The modified system is

$$\begin{aligned} \tilde{\mathbf{A}}'(\mathbf{p};\omega)\ \tilde{\mathbf{x}}'(\mathbf{p};\omega) =& \tilde{\mathbf{b}}' \\ \tilde{\mathbf{y}}(\mathbf{p};\omega) =& \tilde{\mathbf{C}}'(\mathbf{p};\omega)\ \tilde{\mathbf{x}}'(\mathbf{p};\omega), \end{aligned} \tag{6.19}$$

where

$$\tilde{\mathbf{A}}'_{m,n,\cdots} = \begin{cases} \left[\begin{array}{c|c} \tilde{\mathbf{A}}_0 & -\tilde{\mathbf{b}}_0 \\ \hline 0 & \alpha \end{array}\right], & \text{for } \tilde{\mathbf{A}}'_0 \\ \left[\begin{array}{c|c} \tilde{\mathbf{A}}_{m,n,\cdots} & -\tilde{\mathbf{b}}_{m,n,\cdots} \\ \hline 0 & 0 \end{array}\right], & \text{otherwise} \end{cases},$$

$$\tilde{\mathbf{b}}' = \left[\begin{array}{c} 0 \\ \vdots \\ 0 \\ \hline \alpha \end{array}\right],$$

and

$$\tilde{\mathbf{C}}'_{m,n,\cdots} = \left[\begin{array}{c|c} \tilde{\mathbf{C}}_{m,n,\cdots} & 0 \end{array}\right].$$

The scalar α should be chosen to maintain the conditioning of $\mathbf{A}'_0$, and a reasonable choice is the maximum diagonal entry of $\tilde{\mathbf{A}}_0$. Then, the PMM can be readily applied to (6.19) and construct $\mathbf{V}$.

6.5 Summary of the Method

The reduced model for dielectric scattering

$$\begin{aligned}\hat{\mathbf{A}}(\mathbf{p};\omega)\hat{\mathbf{x}}(\mathbf{p};\omega) =&\hat{\mathbf{b}}\\ \hat{\mathbf{y}}(\mathbf{p};\omega) =&\hat{\mathbf{C}}(\mathbf{p};\omega)\hat{\mathbf{x}}(\mathbf{p};\omega)\end{aligned} \tag{6.20}$$

with[1]

$$\begin{aligned}\hat{\mathbf{A}}(\mathbf{p};\omega) =&\hat{\mathbf{A}}_0 - \sum_{m=1}^{N_o+1} p_m\hat{\mathbf{A}}_m - \sum_{m,n=1}^{N_o+1} p_m p_n\hat{\mathbf{A}}_{m,n} - \cdots\\ \hat{\mathbf{C}}(\mathbf{p};\omega) =&\hat{\mathbf{C}}_0 - \sum_{m=1}^{N_o+1} p_m\hat{\mathbf{C}}_m - \sum_{m,n=1}^{N_o+1} p_m p_n\hat{\mathbf{C}}_{m,n} - \cdots\end{aligned}$$

is constructed as follows:

1. The matrices $\mathbf{A}(\mathbf{p};\omega)$ and $\mathbf{C}(\mathbf{p};\omega)$ and the vector $\mathbf{b}(\mathbf{p};\omega)$ in (6.5) are fitted with methods in subsection 6.2.2 and 6.4.1, resulting in

$$\begin{aligned}\tilde{\mathbf{A}}(\mathbf{p};\omega) =&\tilde{\mathbf{A}}_0 - \sum_{m=1}^{N_o+1} p_m\tilde{\mathbf{A}}_m - \sum_{m,n=1}^{N_o+1} p_m p_n\tilde{\mathbf{A}}_{m,n} - \cdots\\ \tilde{\mathbf{C}}(\mathbf{p};\omega) =&\tilde{\mathbf{C}}_0 - \sum_{m=1}^{N_o+1} p_m\tilde{\mathbf{C}}_m - \sum_{m,n=1}^{N_o+1} p_m p_n\tilde{\mathbf{C}}_{m,n} - \cdots\end{aligned}$$

   and

$$\tilde{\mathbf{b}}(\mathbf{p};\omega) = \tilde{\mathbf{b}}_0 - \sum_{m=1}^{N_o+1} p_m\tilde{\mathbf{b}}_m - \sum_{m,n=1}^{N_o+1} p_m p_n\tilde{\mathbf{b}}_{m,n} - \cdots .$$

2. The parameter dependence of $\mathbf{b}$ on $\mathbf{p}$ and ω is removed using the method in subsection 6.4.2, resulting in

$$\begin{aligned}\tilde{\mathbf{A}}'(\mathbf{p};\omega) =&\tilde{\mathbf{A}}'_0 - \sum_{m=1}^{N_o+1} p_m\tilde{\mathbf{A}}'_m - \sum_{m,n=1}^{N_o+1} p_m p_n\tilde{\mathbf{A}}'_{m,n} - \cdots\\ \tilde{\mathbf{C}}'(\mathbf{p};\omega) =&\tilde{\mathbf{C}}'_0 - \sum_{m=1}^{N_o+1} p_m\tilde{\mathbf{C}}'_m - \sum_{m,n=1}^{N_o+1} p_m p_n\tilde{\mathbf{C}}'_{m,n} - \cdots\end{aligned}$$

   and $\tilde{\mathbf{b}}'$.

[1] For convenience of notation, $p_{N_o+1} = \omega$ is used.

3. The projection matrix $\mathbf{V}$ with orthonormal columns is found, and the reduced system is constructed by

$$\hat{\mathbf{A}}_{m,n,\cdots} = \mathbf{V}^H \tilde{\mathbf{A}}'_{m,n,\cdots} \mathbf{V}$$
$$\hat{\mathbf{C}}_{m,n,\cdots} = \tilde{\mathbf{C}}'_{m,n,\cdots} \mathbf{V}$$

for $m, n, \cdots = 1, \cdots, N_o + 1$, and $\hat{\mathbf{b}} = \mathbf{V}^H \tilde{\mathbf{b}}'$.

6.6 Inverse Scattering Analysis

In order the identify $\mathbf{p}$ from the measurements $\mathbf{y}_m(\omega_m)$, a nonlinear least-square problem

$$\min_{\mathbf{p}} \quad \sum_m ||\hat{\mathbf{y}}(\mathbf{p}; \omega_m) - \mathbf{y}_m(\omega_m)||_2^2 \tag{6.21}$$

is solved.

The Jacobian evaluation for the Levenberg-Marquardt algorithm is trivial since the partial derivatives of the reduced integral operators are straightforward to evaluate. For example,

$$\hat{\mathbf{A}}_{p_m}(\mathbf{p}; \omega) = -\hat{\mathbf{A}}_m - \sum_{n=1}^{N_o+1} p_n \hat{\mathbf{A}}_{m,n} - \cdots, \quad m = 1, \cdots, N_o \tag{6.22}$$

and the Jacobian is easily assembled using (4.2) or, more preferably, (4.4).

6.7 Numerical Examples

6.7.1 Case One: a Sphere

The scatterer is a ball of silicon dioxide with permittivity $11.7\epsilon_0$ and permeability μ_0. For a nominal length $\lambda_0 = 200$nm, the test conditions are

- The radius of the sphere is $r \in [0.475\lambda_0, 0.525\lambda_0]$ with the nominal value of $r_0 = 0.5\lambda_0$.
- The incident field is a plane wave with $\lambda \in [0.95\lambda_0, 1.05\lambda_0]$, coming from $\theta = \pi/3$, polarized in the $\hat{x}$-direction; the phase is set to zero at the origin.
- The scattered field is measured at distance $20.013\lambda_0$ away from center in the $(1, 1, 1)$ direction.

The values for λ/λ_0 and r/r_0 are sampled at 0.95, 0.99, 1.01, and 1.05; and they are fitted with a third order polynomial. Then, moments are matched at $(\lambda/\lambda_0, r/r_0) = (1, 1)$, $(0.95, 0.95)$ up to the first order. The reduced model is of size 30-by-30 compared to the original model of size 576-by-576, and it is parameterized in both the wavelength and the radius. As a result, our approach gives a factor of about 8000 times speedup in each model evaluation.

The measured scattered fields $\mathbf{y}_m(\omega_m)$ are evaluated at three different wavelengths, and the optimizer has converged to a minimum of 97.3nm, identifying the true value 97nm with an error of 0.3%.

6.7.2 Case Two: a Pillar

The pillar to be identified has the width w in both the $\hat{x}$- and $\hat{y}$-directions and the height h in the $\hat{z}$-direction. The test conditions are

- The width and the height are $w \in [0.11\lambda_0, 0.14\lambda_0]$ and $h \in [0.225\lambda_0, 0.275\lambda_0]$ with the nominal values of $w_0 = 0.125\lambda_0$ and $h_0 = 0.25\lambda_0$, respectively.
- The same incident field and observation point are used as in the sphere case.

The values for w/w_0 and h/h_0 are sampled at 0.85, 0.95, 1.05, and 1.15; and they are fitted with a third order polynomial. Then, moments are matched at $(w/w_0, h/h_0) = (1, 1)$ up to the second order. Note that the wavelength is no longer a parameter, and three separate models are built for different wavelengths. The original models are of size 540-by-540 each and the reduced models are of size 50-by-50 each, which gives a factor of about 1000 times speedup.

Again, $\mathbf{y}_m(\omega_m)$ are evaluated at three different wavelengths, and the optimizer has converged to 104.9nm, identifying the true value of 105nm with 0.1% error.

Chapter 7

Conclusions and Future Work

A number of fast techniques to solve inverse wave scattering problems in the resonance regime were proposed with an emphasis on faster forward analysis and efficient coupling of the forward and inverse analyses.

First, spectrally convergent Nyström method for scattering by an periodic 2-D structure was proposed. The method separates additional singularities due to the periodic sources in the neighboring periods and integrates the singularities with the modified Fejér quadrature. As a result, periodic structures in 2-D can be analyzed accurately with little memory and computation.

Then, a fast method to approximate the Jacobian for shape optimization problems was proposed. The proposed method requires only a few additional Green's function evaluations, and the cost of Jacobian evaluation does not depend on the number of optimization variables, but on the number of quadrature points, when the Green's function is expensive to evaluate. Therefore, the proposed method is ideal if there are many optimization variables, and a spectrally convergent Nyström method is used for the forward analysis.

Two methods were proposed for problems in 3-D. A new method to evaluate the potential integrals associated with the 3-D mixed-potential integral operator with the Rao-Wilton-Glisson basis function was proposed. The proposed method reduces the surface integral into line integrals and improves the convergence of the line integrals with a change of variables motivated by a complex-domain mapping. The superior accuracy and convergence of the proposed method, compared with a number of existing methods, were demonstrated for nearby- and self-interactions.

A parameterized reduced-order model was introduced to replace the forward analysis, and the slow convergence of projection methods to solve integral equations in 3-D is hidden from the inverse analysis. Improvements to the polynomial-fit parameterized moment matching was proposed for scattering problems, together with the moment matching graph to identify the condition for the projection matrix to match moments. The method was used to identify simple discrete scatterers in 3-D.

Nevertheless, there is room for improvement. A spectrally convergent Nyström method for purely second-kind integral equations for 2-D dielectric scattering can be useful. Second-kind integral equations have better numerical properties than the first-kind [59, 28], and the use of purely second-kind integral equations can improve the quality of the entry-by-entry polynomial fit for the polynomial-fit parameterized moment matching. To solve purely second-kind integral equations, one has to develop a spectrally accurate approximation to the hyper-singular operator. The methods in [101, 99] for the 2-D Green's function can be a reasonable starting point.

The change of variable proposed in chapter 5 is not optimal, and the performance degrades if the evaluation point is lifted slightly from the plane containting the panel, as pointed out briefly in section 5.5. The change of variable may be improved with a futher insight into the integrand as the distance between the evaluation point and the plane containing the panel increases.

It is difficult to apply the polynomial-fit parameterized moment matching to problems with many optimization variables; this can be improved in mainly two ways. The polynomial fitting quickly becomes difficult and expensive as the number of parameters increases. Sparse grids [188] can be a useful idea to reduce the number of samples while maintaining good accuracy of fit.

Secondly, the complexity of the parameterized moment matching algorithm increases exponentially as the number of parameters increases [176, 185]. This problem has to be addressed in order to keep the size of the reduced order model manageable. The sampling method in [185] can be a good point to start.

Appendix A

Nyström Method for Periodic Parameterizations

The Nyström method for periodic Green's function in chapter 3 is extended to structures parameterized by periodic functions. Parameterization by periodic functions are useful for structures with closed boundaries, such as photonic crystals with discrete pillars. The resulting method is very similar to the method for the (non-periodic) 2-D Green's function in [101, 50, 28].

The singularity separation in section 3.2 also applies to problems with periodic parameterizations. The smooth functions $G^{\mathrm{s},-1}$, $G^{\mathrm{s},0}$, $G^{\mathrm{s},1}$, and G^{r} for the periodic Green's function are defined in (3.15) and (3.16), and the corresponding smooth functions $G_n^{\mathrm{s},-1}$, $G_n^{\mathrm{s},0}$, $G_n^{\mathrm{s},1}$, and G_n^{r} for the normal derivative of the periodic Green's function are defined in (3.17) and (3.18).

A.1 Parameterization of Boundary

Consider a smooth 2π-periodic vector valued function $\mathbf{q}$, $\mathbf{q}(t+2\pi) = \mathbf{q}(t)$, that maps $[0, 2\pi]$ to a non-self intersecting closed curve completely contained in a period [101, 50, 28]. The tails of the logarithmic singularity created by the neighboring periodic sources are smooth enough to be integrated without a specialized numerical quadrature. Therefore,

$$G(\mathbf{q}(t), \mathbf{q}(\tau)) = \tilde{G}^{\mathrm{r}}(\mathbf{q}(t), \mathbf{q}(\tau)) + G^{\mathrm{s},0}(\mathbf{q}(t), \mathbf{q}(\tau)) \log(4 \sin^2 \frac{t-\tau}{2}) \tag{A.1}$$

where

$$\tilde{G}^{\mathrm{r}}(\mathbf{q}(t),\mathbf{q}(\tau))$$
$$= \begin{cases} G^{\mathrm{r}}(\mathbf{q}(t),\mathbf{q}(\tau)) + G^{\mathrm{s},-1}(\mathbf{q}(t),\mathbf{q}(\tau))\log R_{-1}^2 + \\ \quad G^{\mathrm{s},0}(\mathbf{q}(t),\mathbf{q}(\tau))\log\dfrac{R_0^2}{4\sin^2\frac{t-\tau}{2}} + G^{\mathrm{s},1}(\mathbf{q}(t),\mathbf{q}(\tau))\log R_1^2, \quad t\neq\tau \\ G^{\mathrm{r}}(\mathbf{q}(t),\mathbf{q}(t)) + G^{\mathrm{s},-1}(\mathbf{q}(t),\mathbf{q}(t))\log R_{-1}^2 + \\ \quad 2G^{\mathrm{s},0}(\mathbf{q}(t),\mathbf{q}(t))\log||\mathbf{q}'(t)|| + G^{\mathrm{s},1}(\mathbf{q}(t),\mathbf{q}(t))\log R_1^2, \quad t=\tau. \end{cases} \tag{A.2}$$

The singularity $\log(4\sin^2\frac{t-\tau}{2})$ is chosen since it is 2π-periodic and behaves like $\log|t-\tau|$ in the limit of τ approaching t. Furthermore, a spectrally convergent numerical quadrature for a smooth 2π-periodic function times the singularity exists as it will be shown in section A.2.

The same idea can be applied to G_n, and the result is (A.1) and (A.2) with $\tilde{G}^{\mathrm{r}}$, G^{r}, $G^{\mathrm{s},-1}$, $G^{\mathrm{s},0}$, and $G^{\mathrm{s},1}$ replaced by $\tilde{G}_n^{\mathrm{r}}$, G_n^{r}, $G_n^{\mathrm{s},-1}$, $G_n^{\mathrm{s},0}$, and $G_n^{\mathrm{s},1}$.

A.2 Numerical Quadrature

The numerical quadratures for smooth 2π-periodic functions and such functions times $\log(\sin^2\frac{t-\tau}{2})$ are well established [189, 102, 101, 97, 98, 99, 100, 28], and they rely on the spectral convergence of trigonometric interpolation with equally spaced points for smooth 2π-periodic functions. Given a 2π-periodic f, $\tilde{f}$ that interpolates f at N_q equally spaced points is

$$\tilde{f}(t) = \begin{cases} \dfrac{1}{N_q}\displaystyle\sum_{n=1}^{N_q} f(\tau_{n/N_q})[\sum_{l=-\nu}^{\nu} e^{jl(t-\tau_{n/N_q})}], & N_q = 2\nu+1 \\ \dfrac{1}{N_q}\displaystyle\sum_{n=1}^{N_q} f(\tau_{n/N_q})[\sum_{l=-\nu}^{\nu}{}'' e^{jl(t-\tau_{n/N_q})}], & N_q = 2\nu \end{cases}$$

where $\tau_{n/N_q} = 2\pi(n-1)/N_q$, $n = 1,\cdots,N_q$. The double primed summation means that the first and the last terms are halved.

A spectrally convergent numerical quadrature for $\int_0^{2\pi} f(\tau)w(\tau)\mathrm{d}\tau$ can be constructed by evaluating $\int_0^{2\pi}\tilde{f}(\tau)w(\tau)\mathrm{d}\tau$ exactly since the error in trigonometric interpolation reduces spectrally [115, 123, 122]. For $w(\tau)=1$, integrating $\tilde{f}$ is trivial and the resulting numerical

quadrature is simply the trapezoidal rule [123, 122]:

$$\int_0^{2\pi} f(\tau)\mathrm{d}\tau \approx \sum_{n=1}^{N_q} w^1_{n/N_q} f(\tau_{n/N_q}) \tag{A.3}$$

where

$$w^1_{n/N_q} = \frac{2\pi}{N_q}. \tag{A.4}$$

For $w(\tau;t) = \log(4\sin^2\frac{t-\tau}{2})$,

$$\int_0^{2\pi} f(\tau)\log(4\sin^2\frac{t-\tau}{2})\mathrm{d}\tau \approx \sum_{n=1}^{N_q} w^{\log}_{n/N_q}(t) f(\tau_{n/N_q}) \tag{A.5}$$

with

$$w^{\log}_{n/N_q}(t) = \begin{cases} -\frac{4\pi}{N_q}\sum_{l=1}^{\nu}\frac{1}{l}\cos[l(t-\tau_{n/N_q})], & N_q = 2\nu+1 \\ -\frac{4\pi}{N_q}\{\sum_{l=1}^{\nu-1}\frac{1}{l}\cos[l(t-\tau_{n/N_q})] + \frac{1}{2\nu}\cos[\nu(t-\tau_{n/N_q})]\}, & N_q = 2\nu \end{cases}$$

since

$$\int_0^{2\pi}\log(4\sin^2\frac{\tau}{2})e^{jl\tau}\mathrm{d}\tau = \begin{cases} 0, & l=0 \\ -\frac{2\pi}{|l|}, & l=\pm1,\pm2,\cdots \end{cases}$$

as in chapter 8 of [28].

A.3 Summary of the Method

Consider the monopole operator $\int G(\mathbf{r},\mathbf{r}')\rho(\mathbf{r}')\mathrm{d}\mathbf{r}'$. For $\mathbf{r} = \mathbf{q}(t)$ for some $t \in [0, 2\pi]$, the discretized monopole operator is

$$\begin{aligned}\int G(\mathbf{r},\mathbf{r}')\rho(\mathbf{r}')\mathrm{d}\mathbf{r}' \approx \sum_{n=1}^{N_q}[w^1_{n/N_q}\tilde{G}^{\mathrm{r}}(\mathbf{q}(t),\mathbf{q}(\tau_{n/N_q}))+ \\ w^{\log}_{n/N_q}(t)G^{\mathrm{s},0}(\mathbf{q}(t),\mathbf{q}(\tau_{n/N_q}))]||\mathbf{q}'(\tau_{n/N_q})||\rho(\mathbf{q}(\tau_{n/N_q})).\end{aligned} \tag{A.6}$$

The normal derivative of the monopole operator $\int G_n(\mathbf{r},\mathbf{r}')\rho(\mathbf{r}')\mathrm{d}\mathbf{r}'$ is discretized similarly, and the result is (A.6) with $\tilde{G}^{\mathrm{r}}$ and $G^{\mathrm{s},0}$ replaced by $\tilde{G}^{\mathrm{r}}_n$ and $G^{\mathrm{s},0}_n$.

For periodic parameterization, the entries of $\mathbf{S}$ in (3.30) are given by

$$\begin{aligned}\mathbf{s}_{m,n} =&[w^1_{n/N_q}\tilde{G}^{\mathrm{r}}(\mathbf{q}(\tau_{m/N_q}),\mathbf{q}(\tau_{n/N_q}))+\\ &2w^{\log}_{n/N_q}(\tau_{m/N_q})G^{\mathrm{s},0}(\mathbf{q}(\tau_{m/N_q}),\mathbf{q}(\tau_{n/N_q}))]||\mathbf{q}'(\tau_{n/N_q})||\end{aligned} \tag{A.7}$$

for $m,n=1,\cdots,N_q$. The entries of $\mathbf{K}'$ are given by (A.7) with $\tilde{G}^{\mathrm{r}}$ and $G^{\mathrm{s},0}$ replaced with $\tilde{G}^{\mathrm{r}}_n$ and $G^{\mathrm{s},0}_n$, respectively.

A.4 Numerical Example

Consider electromagnetic scattering by a layer of dielectric cylinders infinitely periodic in x. The cylinders consist of dielectric matrial with $12\epsilon_0$ and μ_0, and the background medium is air. The structure is illuminated from above by a plane wave with wavelength λ_0 and varying incident angles; the radius of a cylinder is $0.3472\lambda_0$ and the distance between the centers of two neighboring cylinders is $1.3827\lambda_0$.

Figure A-1 shows the reflectance of both E- and H-polarizations as the function of the incident angle. The discretized integral equations for the proposed method is similar to

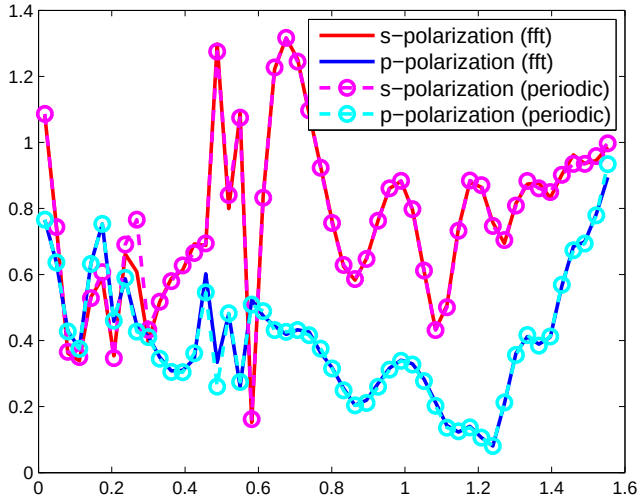

Figure A-1: Reflectance of identical dielectric cylinders in air and infinitely periodic in x as a function of the incident angle.

(3.33) except that S^{in} and K'^{in} uses the 2-D Green's function rather than the periodic Green's function; constructing spectrally convergent approximations to S and K' for the 2-

D Green's function is well-established and shown in [101, 50, 28]. Furthermore, the method can be immediately generalized to more complicated structures, such as the Fabry-Perot structure analyzed in [93].

To show the correctness of the proposed method, the infinitely periodic structure is truncated after 100 periods, and the reflectance is computed using the same techniques to construct Figure 3-1. The two results match well, and the difference becomes smaller as more periods are considered for the truncation method.

Finally, Figure A-2 shows the spectral convergence of the proposed method if it is used to evaluate the scattered field due the infinitely periodic cylinders. The reference solution

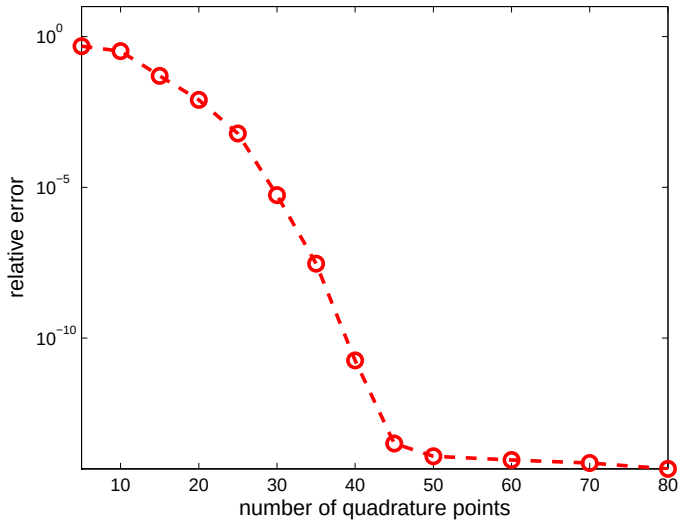

Figure A-2: Relative error in the scattered field.

uses 100-point numerical quadrature.

Appendix B

Analytic Solutions to Scattering by a Circular 2-D Cylinder

Acoustic and electromagnetic scattering due to an infinitely long circular cylinder of various types is commonly used to check the validity of the code. Even though the analytic solutions are found by Sir Rayleigh in 1918 [190], and the results are summarized in [70, 40, 60] and many others, detailed derivations are difficult to find.

This chapter explains how the analytic solutions are derived in detail. The solutions for acoustic scattering by sound-soft, sound-hard, and transparent cylinders are derived in section B.1; the solutions for electromagnetic scattering by perfectly electrically conducting and dielectric cylinders are shown in section B.2.

B.1 Acoustic Scattering by a Circular 2-D Cylinder

Consider the linear acoustic scattering of an incoming plane wave by a circular cylinder of radius a centered at the origin. If the outside medium and the scatterer are characterized by the wave numbers k^{out} and k^{in}, the scattered velocity potential ϕ satisfies

$$\nabla^2\phi + (k^{\text{in}})^2\phi = 0 \tag{B.1}$$

and

$$\nabla^2\phi + (k^{\text{out}})^2\phi = 0 \tag{B.2}$$

inside and outside media, respectively.

Without loss of generality, the incident field is assumed to come from the right due to the symmetry of the scatterer in θ,

$$\phi_{\mathrm{I}} = e^{-j\mathbf{k}^{\mathrm{out}}\cdot\mathbf{r}} = e^{jk^{\mathrm{out}}r\cos\theta}, \tag{B.3}$$

where $\mathbf{k}^{\mathrm{out}} = (-k^{\mathrm{out}}, 0, 0)$ and $\mathbf{r} = r(\cos\theta, \sin\theta, 0)$ are used.

B.1.1 Solution to the Scalar Helmholtz Equation

Consider

$$\nabla^2\phi + k^2\phi = 0 \quad \Leftrightarrow \quad \frac{\partial^2\phi}{\partial x^2} + \frac{\partial^2\phi}{\partial y^2} + k^2\phi = 0 \tag{B.4}$$

for some k. Due to the symmetry of scatterer, it is more convenient to consider (B.4) in the polar coordinate:

$$\frac{1}{r}\frac{\partial}{\partial r}(r\frac{\partial\phi}{\partial r}) + \frac{1}{r^2}\frac{\partial^2\phi}{\partial\theta^2} + k^2\phi = 0.$$

Suppose R_ν and Θ_ν are functions of r and θ only, respectively. Using the separation of variables, $R_\nu\Theta_\nu$ is a solution, and

$$\frac{1}{R_\nu(r)}[r^2\frac{d^2R_\nu(r)}{dr^2} + r\frac{dR_\nu(r)}{dr} + k^2r^2R_\nu(r)] = -\frac{1}{\Theta_\nu(\theta)}\frac{d^2\Theta_\nu(\theta)}{d\theta^2} = \nu^2,$$

where $\nu = 0, 1, \cdots$ is the separation constant chosen to make Θ_ν periodic in θ. Since all $R_\nu\Theta_\nu$, $\nu = 0, 1, \cdots$, are solutions for (B.4), the general solution is

$$\phi(r,\theta) = \sum_{\nu=0}^{\infty} a_\nu R_\nu(r)\Theta_\nu(\theta) \tag{B.5}$$

for some arbitrary constants a_ν determined by the boundary condition.

The ordinary differential equation for Θ_ν is

$$\frac{d^2\Theta_\nu(\theta)}{d\theta^2} + \nu^2\Theta_\nu(\theta) = 0,$$

and the solution is

$$\Theta_\nu(\theta) = A'_\nu\cos(n\theta) + B'_\nu\sin(n\theta)$$

for some constants A'_ν and B'_ν.

Solving for R_ν requires a little more work; the ordinary differential equation for R_ν,

$$r^2\frac{d^2R_\nu(r)}{dr^2}+r\frac{dR_\nu(r)}{dr}+(k^2r^2-\nu^2)R_\nu(r)=0,$$

is equivalent to the well-known Bessel differential equation,

$$w^2\frac{d^2R_\nu(\frac{w}{k})}{dw^2}+w\frac{dR_\nu(\frac{w}{k})}{dw}+(w^2-\nu^2)R_\nu(\frac{w}{k})=0.$$

Therefore, R_ν can be written as the linear combination of either the first- and second-kind Bessel functions or the first- and second-kind Hankel functions.

The choice depends on the type of the boundary condition to be considered. For (B.2), it is more convenient to write R_ν in terms of the first- and second-kind Hankel functions:

$$\begin{aligned} & R_\nu(\frac{w}{k^{\text{out}}})=C'_\nu H_\nu^{(1)}(w)+D'_\nu H_\nu^{(2)}(w) \\ \Leftrightarrow\quad & R_\nu(r)=C'_\nu H_\nu^{(1)}(k^{\text{out}}r)+D'_\nu H_\nu^{(2)}(k^{\text{out}}r) \end{aligned}$$

for some constants C'_ν and D'_ν. Therefore, the general solution is[1]

$$\phi^{\text{out}}(r,\theta)=\sum_{\nu=0}^{\infty}[A'_\nu\cos(\nu\theta)+B'_\nu\sin(\nu\theta)][C'_\nu H_\nu^{(1)}(k^{\text{out}}r)+D'_\nu H_\nu^{(2)}(k^{\text{out}}r)]. \tag{B.6}$$

The general solution in (B.6) is simplified using the properties of ϕ^{out}. Since ϕ^{out} should be even in θ and radiate outwards, $B'_\nu=0$ and $C'_\nu=0$[2]. Therefore,

$$\phi^{\text{out}}(r,\theta)=\sum_{\nu=0}^{\infty}{}'A_\nu H_\nu^{(2)}(k^{\text{out}}r)\cos(\nu\theta) \tag{B.7}$$

with unknown constants A_ν, $\nu=0,1,\cdots$, determined by the boundary condition. The primed summation means that the first term in the summation is halved.

For (B.1), it is more convenient to write R_ν in terms of the first- and second-kind Bessel functions, and the general solution solution is

$$\phi^{\text{in}}(r,\theta)=\sum_{\nu=0}^{\infty}[A'_\nu\cos(\nu\theta)+B'_\nu\sin(\nu\theta)][E'_\nu J_\nu(k^{\text{in}}r)+F'_\nu N_\nu(k^{\text{in}}r)]$$

[1]For the convenience of notation, $a_\nu A'_\nu$ and $a_\nu B'_\nu$ are redefined as A'_ν and B'_ν, respectively.
[2]This means $e^{j\omega t}$ convention is used, i.e. $\varphi(\mathbf{r},t)=\text{Re}\{\phi(\mathbf{r})e^{j\omega t}\}$.

for some constants E'_ν and F'_ν, $\nu = 0, 1, \cdots$. Since the solution has to be even in θ and bounded, $B'_\nu = 0$ and $F'_\nu = 0$. The simpler form of the general solution is

$$\phi^{\text{in}}(r, \theta) = \sum_{\nu=0}^{\infty}{}' B_\nu J_\nu(k^{\text{in}} r) \cos(\nu\theta)$$

with unknown constants B_ν, $\nu = 0, 1, \cdots$, also determined by the boundary condition.

B.1.2 Expansion of ϕ_{I}

Since ϕ is given in terms of the Bessel functions, ϕ_{I} is expanded in a similar manner. Using the Jacobi-Anger expansion,

$$e^{jz\cos\theta} = \sum_{\nu=-\infty}^{\infty} j^\nu J_\nu(z) e^{j\nu\theta},$$

$$\begin{aligned} \phi_{\text{I}}(r, \theta) =& J_0(k^{\text{out}} r) + 2\sum_{\nu=1}^{\infty} j^\nu J_\nu(k^{\text{out}} r)\cos(\nu\theta) \\ =& 2\sum_{\nu=0}^{\infty}{}' j^\nu J_\nu(k^{\text{out}} r)\cos(\nu\theta). \end{aligned} \tag{B.8}$$

B.1.3 Sound-Soft Scatterer

The total velocity potential at the surface of a sound-soft scatter is zero [191, 192],

$$\phi^{\text{out}}(a, \theta) = -\phi_{\text{I}}(a, \theta)$$

for $0 \le \theta \le 2\pi$. Using (B.7) and (B.8),

$$A_\nu = -2j^\nu \frac{J_\nu(k^{\text{out}} a)}{H_\nu^{(2)}(k^{\text{out}} a)}, \quad \nu = 0, 1, \cdots.$$

B.1.4 Sound-Hard Scatterer

The normal derivative of the velocity potential at the surface of a sound-hard scatterer is zero [191, 192],

$$\frac{\partial \phi^{\text{out}}}{\partial r}(a, \theta) = -\frac{\partial \phi_{\text{I}}}{\partial r}(a, \theta)$$

for $0 \le \theta \le 2\pi$. Using the derivatives of (B.7) and (B.8)[3],

$$\frac{\partial \phi^{\text{out}}}{\partial r}(r,\theta) = k^{\text{out}} \sum_{\nu=0}^{\infty}{}' A_\nu H_\nu^{(2)'}(k^{\text{out}} r)\cos(\nu\theta) \tag{B.9}$$

and

$$\frac{\partial \phi_{\text{I}}}{\partial r}(r,\theta) = 2k^{\text{out}} \sum_{\nu=0}^{\infty}{}' j^\nu J_\nu'(k^{\text{out}} r)\cos(\nu\theta), \tag{B.10}$$

the coefficients are

$$A_\nu = -2j^\nu \frac{J_\nu'(k^{\text{out}} a)}{H_\nu^{(2)'}(k^{\text{out}} a)}, \quad \nu = 0, 1, \cdots .$$

B.1.5 Transparent Scatterer

The boundary condition for a transparent scatter is the continuity of velocity potential,

$$\phi^{\text{in}}(a,\theta) = \phi^{\text{out}}(a,\theta) + \phi_{\text{I}}(a,\theta),$$

and the jump in the normal derivative of the velocity potential,

$$\alpha^{\text{in}} \frac{\partial \phi^{\text{in}}}{\partial \hat{\mathbf{n}}}(a,\theta) = \alpha^{\text{out}} [\frac{\partial \phi^{\text{out}}}{\partial \hat{\mathbf{n}}}(a,\theta) + \frac{\partial \phi_{\text{I}}}{\partial \hat{\mathbf{n}}}(a,\theta)]$$

with some α^{in} and α^{out} [191, 192]. Using (B.9), (B.10), and

$$\frac{\partial \phi^{\text{in}}}{\partial r}(r,\theta) = k^{\text{in}} \sum_{\nu=0}^{\infty}{}' B_\nu J_\nu'(k^{\text{in}} r)\cos(\nu\theta),$$

the coefficients can be found from

$$\begin{bmatrix} H_\nu^{(2)}(k^{\text{out}} a) & -J_\nu(k^{\text{in}} a) \\ \alpha^{\text{out}} k^{\text{out}} H_\nu^{(2)'}(k^{\text{out}} a) & -\alpha^{\text{in}} k^{\text{in}} J_\nu'(k^{\text{in}} a) \end{bmatrix} \begin{bmatrix} A_\nu \\ B_\nu \end{bmatrix} = -2j^\nu \begin{bmatrix} J_\nu(k^{\text{out}} a) \\ \alpha^{\text{out}} k^{\text{out}} J_\nu'(k^{\text{out}} a) \end{bmatrix}.$$

[3]The derivatives can be evaluated from (9.1.27) of [109], which translates to

$$J_\nu'(z) = J_{\nu-1}(z) - \frac{\nu}{z} J_\nu(z)$$
$$H_\nu^{(2)'}(z) = H_{\nu-1}^{(2)}(z) - \frac{\nu}{z} H_\nu^{(2)}(z).$$

The solutions are simplified to more meaningful forms. Starting from A_ν,

$$\begin{aligned}
A_\nu =& -2j^\nu \frac{\alpha^{\text{out}}k^{\text{out}}J_\nu(k^{\text{in}}a)J'_\nu(k^{\text{out}}a) - \alpha^{\text{in}}k^{\text{in}}J_\nu(k^{\text{out}}a)J'_\nu(k^{\text{in}}a)}{\alpha^{\text{out}}k^{\text{out}}J_\nu(k^{\text{in}}a)H_\nu^{(2)'}(k^{\text{out}}a) - \alpha^{\text{in}}k^{\text{in}}H_\nu^{(2)}(k^{\text{out}}a)J'_\nu(k^{\text{in}}a)} \\
=& -2j^\nu \frac{\alpha^{\text{out}}k^{\text{out}}J_\nu(k^{\text{in}}a)\frac{J'_\nu(k^{\text{out}}a)}{J_\nu(k^{\text{out}}a)} - \alpha^{\text{in}}k^{\text{in}}J'_\nu(k^{\text{in}}a)}{\alpha^{\text{out}}k^{\text{out}}J_\nu(k^{\text{in}}a)\frac{H_\nu^{(2)'}(k^{\text{out}}a)}{H_\nu^{(2)}(k^{\text{out}}a)} - \alpha^{\text{in}}k^{\text{in}}J'_\nu(k^{\text{in}}a)} \frac{J_\nu(k^{\text{out}}a)}{H_\nu^{(2)}(k^{\text{out}}a)} \\
=& -2j^\nu \frac{\alpha^{\text{out}}k^{\text{out}}\frac{J'_\nu(k^{\text{out}}a)}{J_\nu(k^{\text{out}}a)} - \alpha^{\text{in}}k^{\text{in}}\frac{J'_\nu(k^{\text{in}}a)}{J_\nu(k^{\text{in}}a)}}{\alpha^{\text{out}}k^{\text{out}}\frac{H_\nu^{(2)'}(k^{\text{out}}a)}{H_\nu^{(2)}(k^{\text{out}}a)} - \alpha^{\text{in}}k^{\text{in}}\frac{J'_\nu(k^{\text{in}}a)}{J_\nu(k^{\text{in}}a)}} \frac{J_\nu(k^{\text{out}}a)}{H_\nu^{(2)}(k^{\text{out}}a)}
\end{aligned}$$

for $\nu = 0, 1, \cdots$. Similarly,

$$\begin{aligned}
B_\nu =& -2j^\nu \frac{\alpha^{\text{out}}k^{\text{out}}H_\nu^{(2)}(k^{\text{out}}a)J'_\nu(k^{\text{out}}a) - \alpha^{\text{out}}k^{\text{out}}J_\nu(k^{\text{out}}a)H_\nu^{(2)'}(k^{\text{out}}a)}{\alpha^{\text{out}}k^{\text{out}}J_\nu(k^{\text{in}}a)H_\nu^{(2)'}(k^{\text{out}}a) - \alpha^{\text{in}}k^{\text{in}}H_\nu^{(2)}(k^{\text{out}}a)J'_\nu(k^{\text{in}}a)} \\
=& -2j^\nu \frac{\alpha^{\text{out}}k^{\text{out}}J'_\nu(k^{\text{out}}a) - \alpha^{\text{out}}k^{\text{out}}J_\nu(k^{\text{out}}a)\frac{H_\nu^{(2)'}(k^{\text{out}}a)}{H_\nu^{(2)}(k^{\text{out}}a)}}{\alpha^{\text{out}}k^{\text{out}}J_\nu(k^{\text{in}}a)\frac{H_\nu^{(2)'}(k^{\text{out}}a)}{H_\nu^{(2)}(k^{\text{out}}a)} - \alpha^{\text{in}}k^{\text{in}}J'_\nu(k^{\text{in}}a)} \\
=& -2j^\nu \frac{\alpha^{\text{out}}k^{\text{out}}\frac{J'_\nu(k^{\text{out}}a)}{J_\nu(k^{\text{out}}a)} - \alpha^{\text{out}}k^{\text{out}}\frac{H_\nu^{(2)'}(k^{\text{out}}a)}{H_\nu^{(2)}(k^{\text{out}}a)}}{\alpha^{\text{out}}k^{\text{out}}\frac{H_\nu^{(2)'}(k^{\text{out}}a)}{H_\nu^{(2)}(k^{\text{out}}a)} - \alpha^{\text{in}}k^{\text{in}}\frac{J'_\nu(k^{\text{in}}a)}{J_\nu(k^{\text{in}}a)}} \frac{J_\nu(k^{\text{out}}a)}{J_\nu(k^{\text{in}}a)}
\end{aligned}$$

for $\nu = 0, 1, \cdots$.

B.2 Electromagnetic Scattering by a Circular 2-D Cylinder

Consider the electromagnetic scattering of an incoming plane wave by a circular cylinder of radius a centered at the origin. As explained in subsection 2.1.1, solving the Maxwell's equation for 2-D problems is equivalent to solving two scalar Helmholtz equations. They are (B.1) and (B.2) with E_z instead of ϕ for the E-polarization and with H_z for the H-polarization.

The inside and outside media are characterized by $(k^{\text{in}}, \eta^{\text{in}})$, and $(k^{\text{out}}, \eta^{\text{out}})$, respectively. The wavenumber k and the intrinsic impedance η are given by

$$k = \omega\sqrt{\epsilon\mu}$$

and

$$\eta = \sqrt{\frac{\mu}{\epsilon}},$$

where ϵ and μ are the permittivity and permeability of the medium, and ω is the angular frequency.

Similar to acoustic scattering, the incident field is assumed to come from the right. Then, $\mathbf{E}_{\mathrm{I}} = (0, E_{\mathrm{I},y}, E_{\mathrm{I},z})$ is

$$\begin{aligned} E_{\mathrm{I},y} =& E_{\mathrm{I}}^0 e^{jk^{\mathrm{out}} r\cos\theta} \\ E_{\mathrm{I},z} =& e^{jk^{\mathrm{out}} r\cos\theta}. \end{aligned}$$

for some given complex constant E_{I}^0, and $\mathbf{H}_{\mathrm{I}}$ is completely determined by the Maxwell's equations in (2.1): $\mathbf{H}_{\mathrm{I}} = (0, H_{\mathrm{I},y}, H_{\mathrm{I},z})$ with

$$\begin{aligned} H_{\mathrm{I},y} =& \frac{1}{\eta^{\mathrm{out}}} e^{jk^{\mathrm{out}} r\cos\theta} \\ H_{\mathrm{I},z} =& -\frac{E_{\mathrm{I}}^0}{\eta^{\mathrm{out}}} e^{jk^{\mathrm{out}} r\cos\theta}. \end{aligned}$$

B.2.1 Solutions to the Scalar Helmholtz Equations

Consider the E-polarization. From the analysis in subsection B.1.1, the general solutions to (B.1) and (B.2) with E_z instead of ϕ for a cylindrical scatterer are

$$\begin{aligned} E_z^{\mathrm{out}}(r,\theta) =& \sum_{\nu=0}^{\infty}{}' C_\nu H_\nu^{(2)}(k^{\mathrm{out}} r)\cos(\nu\theta) \\ E_z^{\mathrm{in}}(r,\theta) =& \sum_{\nu=0}^{\infty}{}' D_\nu J_\nu(k^{\mathrm{in}} r)\cos(\nu\theta) \end{aligned} \tag{B.11}$$

where C_ν and D_ν, $\nu = 0, 1, \cdots$, are unknown constants determined by the boundary condition.

The corresponding magnetic field can be found from the Maxwell's equations. Since the scatterer is a cylinder, the cylindrical coordinate representation of the curl operator gives the tangential components directly:

$$\nabla \times \mathbf{f} = [\frac{1}{r}\frac{\partial f_z}{\partial \theta} - \frac{\partial f_\theta}{\partial z}]\hat{r} + [\frac{\partial f_r}{\partial z} - \frac{\partial f_z}{\partial r}]\hat{\theta} + \frac{1}{r}[\frac{\partial}{\partial r}(r f_\theta) - \frac{\partial f_r}{\partial \theta}]\hat{z}$$

for some vector valued function $\mathbf{f} = (f_r, f_\theta, f_z)$.

Hence,

$$\begin{aligned} H_r =& \frac{-1}{jk\eta r}\frac{\partial E_z}{\partial \theta} \\ H_\theta =& \frac{1}{jk\eta}\frac{\partial E_z}{\partial r}, \end{aligned} \tag{B.12}$$

and the term-by-term differentiation of (B.11) gives

$$\begin{aligned} H_r^{\text{out}}(r,\theta) =& \frac{-j}{k^{\text{out}}\eta^{\text{out}}}\sum_{\nu=1}^{\infty}\nu C_\nu \frac{H_\nu^{(2)}(k^{\text{out}}r)}{r}\sin(\nu\theta) \\ H_r^{\text{in}}(r,\theta) =& \frac{-j}{k^{\text{in}}\eta^{\text{in}}}\sum_{\nu=1}^{\infty}\nu D_\nu \frac{J_\nu(k^{\text{in}}r)}{r}\sin(\nu\theta) \end{aligned}$$

and

$$\begin{aligned} H_\theta^{\text{out}}(r,\theta) =& \frac{-j}{\eta^{\text{out}}}\sum_{\nu=0}^{\infty}{}'C_\nu H_\nu^{(2)\prime}(k^{\text{out}}r)\cos(\nu\theta) \\ H_\theta^{\text{in}}(r,\theta) =& \frac{-j}{\eta^{\text{in}}}\sum_{\nu=0}^{\infty}{}'D_\nu J_\nu'(k^{\text{in}}r)\cos(\nu\theta). \end{aligned}$$

The H-polarization works in a similar way. The general solutions for a circular scatterer are

$$\begin{aligned} H_z^{\text{out}}(r,\theta) =& \sum_{\nu=0}^{\infty}{}'E_\nu H_\nu^{(2)}(k^{\text{out}}r)\cos(\nu\theta) \\ H_z^{\text{in}}(r,\theta) =& \sum_{\nu=0}^{\infty}{}'F_\nu J_\nu(k^{\text{in}}r)\cos(\nu\theta) \end{aligned}$$

where E_ν and F_ν, $\nu = 0, 1, \cdots$, are unknown constants determined by the boundary condition. From

$$\begin{aligned} E_r =& \frac{\eta}{jkr}\frac{\partial H_z}{\partial \theta} \\ E_\theta =& \frac{-\eta}{jk}\frac{\partial H_z}{\partial r}, \end{aligned} \tag{B.13}$$

the corresponding electric fields are

$$E_r^{\text{out}}(r,\theta) = \frac{j\eta^{\text{out}}}{k^{\text{out}}} \sum_{\nu=1}^{\infty} \nu E_\nu \frac{H_\nu^{(2)}(k^{\text{out}} r)}{r} \sin(\nu\theta)$$
$$E_r^{\text{in}}(r,\theta) = \frac{j\eta^{\text{in}}}{k^{\text{in}}} \sum_{\nu=1}^{\infty} \nu F_\nu \frac{J_\nu(k^{\text{in}} r)}{r} \sin(\nu\theta)$$

and

$$E_\theta^{\text{out}}(r,\theta) = j\eta^{\text{out}} \sum_{\nu=0}^{\infty}{}' E_\nu H_\nu^{(2)\prime}(k^{\text{out}} r) \cos(\nu\theta)$$
$$E_\theta^{\text{in}}(r,\theta) = j\eta^{\text{in}} \sum_{\nu=0}^{\infty}{}' F_\nu J_\nu'(k^{\text{in}} r) \cos(\nu\theta).$$

B.2.2 Expansion of $\mathbf{E_I}$ and $\mathbf{H_I}$

In order to enforce boundary conditions at the surface of the cylindrical scatterer, the tangential fields at the surface has to be expanded in terms of Bessel functions. Following the idea in subsection B.1.2, the z-components of the fields are

$$E_{\text{I},z}(r,\theta) = 2 \sum_{\nu=0}^{\infty}{}' j^\nu J_\nu(k^{\text{out}} r) \cos(\nu\theta)$$

for the E-polarization and

$$H_{\text{I},z}(r,\theta) = -\frac{2E_{\text{I}}^0}{\eta^{\text{out}}} \sum_{\nu=0}^{\infty}{}' j^\nu J_\nu(k^{\text{out}} r) \cos(\nu\theta)$$

for the H-polarization. Using (B.12) and (B.13), the corresponding θ-components of the fields are

$$H_{\text{I},\theta}(r,\theta) = \frac{-2j}{\eta^{\text{out}}} \sum_{\nu=0}^{\infty}{}' j^\nu J_\nu'(k^{\text{out}} r) \cos(\nu\theta)$$

and

$$E_{\text{I},\theta}(r,\theta) = -2jE_{\text{I}}^0 \sum_{\nu=0}^{\infty}{}' j^\nu J_\nu'(k^{\text{out}} r) \cos(\nu\theta).$$

B.2.3 Perfectly Electrically Conducting Scatterer

The tangential electric field on the surface of a perfectly electrically conducting scatterer is zero. For the E-polarization, this means

$$E_z^{\text{out}}(a,\theta) = -E_{\text{I},z}(a,\theta),$$

and

$$C_\nu = -2j^\nu \frac{J_\nu(k^{\text{out}}a)}{H_\nu^{(2)}(k^{\text{out}}a)}, \quad \nu = 0, 1, \cdots$$

The result is identical to that of the acoustically sound-soft scattering in subsection B.1.3.

For the H-polarization, the boundary condition translates to

$$E_\theta^{\text{out}}(a,\theta) = -E_{\text{I},\theta}(a,\theta),$$

and

$$E_\nu = \frac{2E_{\text{I}}^0 j^\nu}{\eta^{\text{out}}} \frac{J_\nu'(k^{\text{out}}a)}{H_\nu^{(2)'}(k^{\text{out}}a)}, \quad \nu = 0, 1, \cdots,$$

which is evaluated by scaling the acoustically sound-hard scattering result in subsection B.1.4 by $-E_{\text{I}}^0/\eta^{\text{out}}$.

B.2.4 Dielectric Scatterer

The boundary condition for dielectric scatterers is the continuity of the tangential electric and magnetic fields. For the E-polarization, this means

$$\begin{aligned} E_z^{\text{out}}(a,\theta) + E_{\text{I},z}(a,\theta) &= E_z^{\text{in}}(a,\theta) \\ H_\theta^{\text{out}}(a,\theta) + H_{\text{I},\theta}(a,\theta) &= H_\theta^{\text{in}}(a,\theta) \end{aligned}$$

or

$$\begin{bmatrix} H_\nu^{(2)}(k^{\text{out}}a) & -J_\nu(k^{\text{in}}a) \\ \frac{1}{\eta^{\text{out}}} H_\nu^{(2)'}(k^{\text{out}}a) & -\frac{1}{\eta^{\text{in}}} J_\nu'(k^{\text{in}}a) \end{bmatrix} \begin{bmatrix} C_\nu \\ D_\nu \end{bmatrix} = -2j^\nu \begin{bmatrix} J_\nu(k^{\text{out}}a) \\ \frac{1}{\eta^{\text{out}}} J_\nu'(k^{\text{out}}a) \end{bmatrix},$$

and the solution is

$$C_\nu = -2j^\nu \frac{\frac{1}{\eta^{\rm out}}\frac{J_\nu'(k^{\rm out}a)}{J_\nu(k^{\rm out}a)} - \frac{1}{\eta^{\rm in}}\frac{J_\nu'(k^{\rm in}a)}{J_\nu(k^{\rm in}a)}}{\frac{1}{\eta^{\rm out}}\frac{H_\nu^{(2)'}(k^{\rm out}a)}{H_\nu^{(2)}(k^{\rm out}a)} - \frac{1}{\eta^{\rm in}}\frac{J_\nu'(k^{\rm in}a)}{J_\nu(k^{\rm in}a)}} \frac{J_\nu(k^{\rm out}a)}{H_\nu^{(2)}(k^{\rm out}a)}$$

and

$$D_\nu = -2j^\nu \frac{\frac{1}{\eta^{\rm out}}\frac{J_\nu'(k^{\rm out}a)}{J_\nu(k^{\rm out}a)} - \frac{1}{\eta^{\rm out}}\frac{H_\nu^{(2)'}(k^{\rm out}a)}{H_\nu^{(2)}(k^{\rm out}a)}}{\frac{1}{\eta^{\rm out}}\frac{H_\nu^{(2)'}(k^{\rm out}a)}{H_\nu^{(2)}(k^{\rm out}a)} - \frac{1}{\eta^{\rm in}}\frac{J_\nu'(k^{\rm in}a)}{J_\nu(k^{\rm in}a)}} \frac{J_\nu(k^{\rm out}a)}{J_\nu(k^{\rm in}a)}$$

for $\nu = 0, 1, \cdots$. These values are evaluated from the acoustically transparent scattering result in subsection B.1.5 using $\alpha^{\rm out} = 1/(k^{\rm out}\eta^{\rm out})$ and $\alpha^{\rm in} = 1/(k^{\rm in}\eta^{\rm in})$.

For the H-polarization, the boundary condition translates to

$$\begin{aligned} H_z^{\rm out}(a,\theta) + H_{{\rm I},z}(a,\theta) =& H_z^{\rm in}(a,\theta) \\ E_\theta^{\rm out}(a,\theta) + E_{{\rm I},\theta}(a,\theta) =& E_\theta^{\rm in}(a,\theta) \end{aligned}$$

or

$$\begin{bmatrix} H_\nu^{(2)}(k^{\rm out}a) & -J_\nu(k^{\rm in}a) \\ \eta^{\rm out}H_\nu^{(2)'}(k^{\rm out}a) & -\eta^{\rm in}J_\nu'(k^{\rm in}a) \end{bmatrix} \begin{bmatrix} E_\nu \\ F_\nu \end{bmatrix} = \frac{2E_{\rm I}^0 j^\nu}{\eta^{\rm out}} \begin{bmatrix} J_\nu(k^{\rm out}a) \\ \eta^{\rm out}J_\nu'(k^{\rm out}a) \end{bmatrix},$$

and the solution is

$$E_\nu = \frac{2E_{\rm I}^0 j^\nu}{\eta^{\rm out}} \frac{\eta^{\rm out}\frac{J_\nu'(k^{\rm out}a)}{J_\nu(k^{\rm out}a)} - \eta^{\rm in}\frac{J_\nu'(k^{\rm in}a)}{J_\nu(k^{\rm in}a)}}{\eta^{\rm out}\frac{H_\nu^{(2)'}(k^{\rm out}a)}{H_\nu^{(2)}(k^{\rm out}a)} - \eta^{\rm in}\frac{J_\nu'(k^{\rm in}a)}{J_\nu(k^{\rm in}a)}} \frac{J_\nu(k^{\rm out}a)}{H_\nu^{(2)}(k^{\rm out}a)}$$

and

$$F_\nu = \frac{2E_{\rm I}^0 j^\nu}{\eta^{\rm out}} \frac{\eta^{\rm out}\frac{J_\nu'(k^{\rm out}a)}{J_\nu(k^{\rm out}a)} - \eta^{\rm out}\frac{H_\nu^{(2)'}(k^{\rm out}a)}{H_\nu^{(2)}(k^{\rm out}a)}}{\eta^{\rm out}\frac{H_\nu^{(2)'}(k^{\rm out}a)}{H_\nu^{(2)}(k^{\rm out}a)} - \eta^{\rm in}\frac{J_\nu'(k^{\rm in}a)}{J_\nu(k^{\rm in}a)}} \frac{J_\nu(k^{\rm out}a)}{J_\nu(k^{\rm in}a)}$$

for $\nu = 0, 1, \cdots$. Again, these values are evaluated from the acoustically transparent scattering results in subsection B.1.5 using $\alpha^{\rm out} = \eta^{\rm out}/k^{\rm out}$ and $\alpha^{\rm in} = \eta^{\rm in}/k^{\rm in}$ and scaling the result by $-E_{\rm I}^0/\eta^{\rm out}$.

Bibliography

[1] Rolf K. Mueller, Mostafa Kaveh, and Glen Wade. Reconstructive tomography and applications to ultrasonics. *Proceedings of the IEEE*, 67(4):567–587, 1979.

[2] Azriel Rosenfeld and Avinash C. Kak. *Digital Picture Processing, Volume 1.* Academic Press, second edition, 1982.

[3] B. D. Sleeman. The inverse problem of acoustic scattering. *IMA Journal of Applied Mathematics*, 29:113–142, 1982.

[4] S. X. Pan and Avinash C. Kak. A computational study of reconstruction algorithms for diffraction tomography: Interpolation versus filtered backpropagation. *IEEE Transactions on Acoustic, Speech, and Signal Processing*, 31(5):1262–1275, 1983.

[5] Avinash C. Kak and Malcolm Slaney. *Principles of Computerized Tomographic Imaging.* IEEE Press, 1988.

[6] Frank Natterer. *The Mathematics of Computerized Tomography.* Society for Industrial and Applied Mathematics, 2001.

[7] Philip Carrion. *Inverse Problems and Tomography in Acoustic and Seismology.* Penn Publishing, 1987.

[8] J. Trampert, J.-J. Leveque, and M. Cara. Inverse problems in seismology. In M. Bertero and E. R. Pike, editors, *Inverse Problems in Scattering and Imaging*, pages 131–145. 1991.

[9] J. J. Stamnes, L.-J. Gelius, I. Johansen, and N. Sponheim. Diffraction tomography applications in seismics and medicine. In M. Bertero and E. R. Pike, editors, *Inverse Problems in Scattering and Imaging*, pages 268–318. 1991.

[10] Douglas Gough. The success story of the transfer and development of methods from geophysics to helioseismology. In Bo Holm Jacobsen, Klaus Moosegard, and Paolo Sibani, editors, *Inverse Methods: Interdisciplinary Elements of Methodology, Computation, and Applications*, pages 1–31. 1996.

[11] John A. Scales. Uncertainties in seismic inverse calculations. In Bo Holm Jacobsen, Klaus Moosegard, and Paolo Sibani, editors, *Inverse Methods: Interdisciplinary Elements of Methodology, Computation, and Applications*, pages 79–97. 1996.

[12] Marwan Charara, Christophe Barnes, and Albert Tarantola. Constrained waveform inversion of seismic well data. In Bo Holm Jacobsen, Klaus Moosegard, and Paolo Sibani, editors, *Inverse Methods: Interdisciplinary Elements of Methodology, Computation, and Applications*, pages 98–112. 1996.

[13] Christophe Barnes, Marwan Charara, and Albert Tarantola. Geological information and the inversion of seismic data. In Bo Holm Jacobsen, Klaus Moosegard, and Paolo Sibani, editors, *Inverse Methods: Interdisciplinary Elements of Methodology, Computation, and Applications*, pages 113–121. 1996.

[14] Brett Borden. Mathematical problems in radar inverse scattering. *Inverse Problems*, 18:R1–R28, 2002.

[15] David Colton, Haussem Haddar, and Michele Piana. The linear sampling method in inverse electromagnetic scattering theory. *Inverse Problems*, 19:S105–S137, 2003.

[16] H. P. Kleinknecht and H. Meier. Linewidth measurement on IC masks and wafers by grating test patterns. *Applied Optics*, 19(4):525–533.

[17] C. J. Raymond, M. R. Murnane, S. L. Prins, S. Sohail, H. Naqvi, J. R. McNeil, and J. W. Hosch. Multiparameter grating metrology using optical scatterometry. *Journal of Vacuum Science & Technology B*, 15(2):361–368, 1997.

[18] Xinhui Niu, Nickhil Jakatdar, Junwei Bao, Costas Spanos, and Sanjay Yedur. Specular spectroscopic scatterometry in DUV lithography. *Proceedings of SPIE*, 3677:159–168, 1999.

[19] X. Niu, N. Jakatdar, J. Bao, and C. J. Spanos. Specular spectroscopic scatterometry. *IEEE Transactions on Semiconductor Manufacturing*, 14(2):97–111, 2001.

[20] J. A. Allgair, D. C. Benoit, M. Drew, R. R. Hershey, L. C. Litt, P. P. Herrera, U. K. Whitney, M. Guevremont, A. Levy, and S. Lakkapragada. Implementation of spectroscopic critical dimension (SCD) for gate CD control and stepper characterization. *Proceedings of SPIE, Metrology, Inspection, and Process Control for Microlithography XV*, 4344:462–471, 2001.

[21] A. Levy, S. Lakkapragada, W. Mieher, K. Bhatia, U. Whitney, and M Hankinson. Spectroscopic CD technology for gate process control. In *Semiconductor Manufacturing Symposium*, pages 141–144, 2001.

[22] J. Allgair, R. Hershey, L. Litt, D. Benoit, and A. Levy. Spectroscopic critical dimension (SCD) metrology for CD control and stepper characterization. *Yield Management Solutions*, pages 50–55, 2001.

[23] John A. Allgair and Benjamin D. Bunday. A review of scatterometry for three-dimensional semiconductor feature analysis. *Future Fab International*, 19:125–128, 2005.

[24] M. A. Fiddy. Linearized and approximate methods for inversion of scattered field data. In M. Bertero and E. R. Pike, editors, *Inverse Problems in Scattering and Imaging*, pages 23–46. 1991.

[25] Jin Au Kong. *Electromagnetic Wave Theory*. EMW Publishing, 2000.

[26] Martin Hanke and Martin Brühl. Recent progress in electrical impedance tomography. *Inverse Problems*, 19:S65–S90, 2003.

[27] Kendall E. Atkinson. *The Numerical Solution of Integral Equations of the Second Kind*. Cambridge University Press, 1997.

[28] Rainer Kress. *Linear Integral Equations*. Springer, second edition, 1999.

[29] J. L. Hess and A. M. O. Smith. Calculation of potential flow about arbitrary bodies. *Progress in Aeronautical Sciences*, 8:1–138, 1967.

[30] D. R. Wilton, S. M. Rao, A. W. Glisson, D. H. Schaubert, O. M. Al-Bundak, and C. M. Butler. Potential integrals for uniform and linear source distributions on polygonal and polyhedral domains. *IEEE Transactions on Antennas and Propagation*, 32:276–281, 1984.

[31] J. N. Newman. Distributions of sources and normal dipoles over a quadrilateral panel. *Journal of Engineering Mathematics*, 20:113–126, 1986.

[32] Silvia Carrasco, Magued B. Nasr, Alexander V. Sergienko, Bahaa E. A. Saleh, and Malvin C. Teich. Broadband light generation by noncollinear parametric downconversion. *Optics Letters*, 31(2):253–255, 2006.

[33] Husain Imam. Broad as a lamp, bright as a laser. *Nature Photonics*, 2:26–28, 2008.

[34] H. Moharam and T. Gaylord. Rigorous coupled-wave analysis of planar-grating diffraction. *Journal of the Optical Society of America*, 71(7), 1981.

[35] M. Moharam and T. Gaylord. Diffraction analysis of dielectric surface-relief gratings. *Journal of the Optical Society of America*, 72(10), 1982.

[36] T. Gaylord and M. Moharam. Analysis and applications of optical diffraction by gratings. *Proceedings of the IEEE*, 73(5), 1985.

[37] David Colton. The inverse scattering problem for time-harmonic acoustic waves. *SIAM Review*, 26(3):323–350, 1984.

[38] Roland Potthast. A fast new method to solve inverse scattering problems. *Inverse Problems*, 12:731–742, 1996.

[39] T. S. Angell, Xinming Jiang, and R. E. Kleinman. A distributed source method for inverse acoustic scattering. *Inverse Problems*, 13:531–545, 1997.

[40] J. J. Bowman, T. B. A. Senior, and P. L. E. Uslenghi. *Electromagnetic and Acoustic Scattering by Simple Shapes*. Hemisphere Publishing Corporation, 1987.

[41] J. W. Thomas. *Numerical Partial Differential Equations: Finite Difference Methods*. Springer, 1995.

[42] Allen Taflove and Susan C. Hagness. *Computational Electrodynamics: The Finite-Difference Time-Domain Method*. Artech House Publishers, third edition, 2005.

[43] Niels Ottosen and Hans Petersson. *Introduction to the Finite Element Method*. Prentice Hall, 1992.

[44] Jianming Jin. *The Finite Element Method in Electromagnetics*. Wiley, second edition, 2002.

[45] Roger F. Harrington. *Field Computation by Moment Methods*. The Macmillan Company, 1968.

[46] C. A. Brebbia, J. C. F. Telles, and L. C. Wrobel. *Boundary Element Techniques: Theory and Applications in Engineering*. Springer-Verlag, 1984.

[47] Mokhtar S. Bazaraa, Hanif D. Sherali, and C. M. Shetty. *Nonlinear Programming: Theory and Algorithms*. John Wiley and Sons, Inc., second edition, 1993.

[48] Stephen Boyd and Lieven Vandenberghe. *Convex Optimization*. Cambridge University Press, 2004.

[49] Andreas Kirsch. *An Introduction to the Mathematical Theory of Inverse Problems*. Springer, 1996.

[50] David Colton and Rainer Kress. *Inverse Acoustic and Electromagnetic Scattering Theory*. Springer, second edition, 1998.

[51] Per Christian Hansen. *Rank-Deficient and Discrete Ill-Posed Problems*. Society for Industrial and Applied Mathematics, 1998.

[52] Richard C. Aster, Brian Borchers, and Clifford Thurber. *Parameter Estimation and Inverse Problems*. Academic Press, 2004.

[53] Dimitri P. Bertsekas. *Nonlinear Programming*. Athena Scientific, second edition, 1999.

[54] Jorge Nocedal and Stephen Wright. *Numerical Optimization*. Springer, 1999.

[55] J. E. Dennis Jr. Non-linear least squares and equations. In *The State of the Art in Numerical Analysis*, pages 267–312. Academic Press, 1977.

[56] J. Haslinger and R. A. E. Mäkinen. *Introduction to Shape Optimization: Theory, Approximation, and Computation*. Society for Industrial and Applied Mathematics, 2003.

[57] G. Milton Wing. *A Primer on Integral Equations of the First Kind: The Problem of Deconvolution and Unfolding*. Society for Industrial and Applied Mathematics, 1991.

[58] Kun-Mu Chen. A mathematical formulation of the equivalence principle. *IEEE Transactions on Microwave Theory and Techniques*, 37(10):1576–1581, 1989.

[59] R. F. Harrington. Boundary integral formulation for homogeneous material bodies. *Journal of Electromagnetic Waves and Applications*, pages 1–15, 1989.

[60] R. F. Harrington. *Time-Harmonic Electromagnetic Fields*. Wiley (reprint of 1961 edition), 2001.

[61] Claus Müller. *Foundations of the Mathematical Theory of Electromagnetic Waves*. Springer-Verlag, 1969.

[62] Weng Cho Chew. *Waves and Fields in Inhomogeneous Media*. IEEE Press, 1995.

[63] L. N. Medgyesi-Mitschang, J. M. Putnam, and M. B. Gedera. Generalized method of moments for three-dimensional penetrable scatterers. *Journal of the Optical Society of America A*, pages 1383–1398, 1994.

[64] B. H. Jung, T. K. Sarkar, and Y. S. Chung. A survey of various frequency domain integral equations for the analysis of scattering from three-dimensional dielectric objects. *Progress in Electromagnetics Research*, pages 193–246, 2002.

[65] Donald G. Dudley. *Mathematical Foundations for Electromagnetic Theory*. IEEE Press, 1994.

[66] Lei Zhang. *A Fast 3D Full-Wave Solver for Nanophotonics*. PhD thesis, Massachusetts Institute of Technology, 2007.

[67] Robert E. Collin. *Field Theory of Guided Waves*. Wiley-IEEE Press, second edition, 1990.

[68] Hermann A. Haus and James R. Melcher. *Electromagnetic Fields and Energy*. Prentice Hall, 1989.

[69] W. D. Jackson. *Classical Electrodynamics*. John Wiley and Sons, Inc., third edition, 1999.

[70] J. A. Stratton. *Electromagnetic Theory*. McGraw-Hill, 1941.

[71] Krzysztof A. Michalski and Dalian Zheng. Electromagnetic scattering and radiation by surfaces of arbitrary shape in layered media, part I: Theory. *IEEE Transactions on Antennas and Propagation*, 38(3):335–344, 1990.

[72] Krzysztof A. Michalski and Dalian Zheng. Electromagnetic scattering and radiation by surfaces of arbitrary shape in layered media, part II: Implementation and results for contiguous half-spaces. *IEEE Transactions on Antennas and Propagation*, 38(3):345–352, 1990.

[73] Krzysztof A. Michalski and Juan R. Mosig. Multilayered media Green's functions in integral equation formulations. *IEEE Transactions on Antennas and Propagation*, 45(3):508–519, 1997.

[74] X. Hu, J. White, J. H. Lee, and L. Daniel. Analysis of full-wave conductor system impedance over substrate using novel integration techniques. In *Proceedings of DAC*, pages 147–152, 2005.

[75] R. Petit, editor. *Electromagnetic Theory of Gratings*. Springer-Verlag, 1980.

[76] John D. Joannopoulos, Robert D. Meade, and Joshua N. Winn. *Photonic Crystals: Molding the Flow of Light*. Princeton University Press, 1995.

[77] A. Rathsfeld, G. Schmidt, and B. H. Kleemann. On a fast integral equation method for diffraction gratings. *Communications in Computational Physics*, 1(6):984–1009, 2006.

[78] Ortwin Hess, Christian Hermann, and Andreas Klaedtke. Finite-difference time-domain simulations of photonic crystal defect structures. *Physica Status Solidi A, Applied Research*, 197(3):605–619.

[79] Shangping Guo, Feng Wu, and Sacharia Albin. Photonic band gap analysis using finite-difference frequency-domain method. *Optics Express*, 12(8):1741–1746.

[80] Thomas F. Eibert, John L. Volakis, Donald R. Wilton, and David R. Jackson. Hybrid FE/BI modeling of 3-D doubly periodic structures utilizing triangular prismatic elements and an MPIE formulation accelerated by the Ewald transformation. *IEEE Transactions on Antennas and Propagation*, 47(5):843–850, 1999.

[81] John L. Volakis, Thomas F. Eibert, and Kubilay Sertel. Fast integral methods for conformal antenna and array modeling in conjunction with hybrid finite element formulations. *Radio Science*, 35(2):537–546, 2000.

[82] Thomas F. Eibert, Yunus E. Erdemli, and John L. Volakis. Hybrid finite element-fast spectral domain multilayer boundary integral modeling of doubly periodic structures. *IEEE Transactions on Antennas and Propagation*, 51(9):2517–2520, 2003.

[83] John L. Volakis, Kubilay Sertel, and Brian C. Usner. *Frequency Domain Hybrid Finite Element Methods for Electromagnetics*. Morgan & Claypool Publishers, 2006.

[84] B. C. Usner, K. Sertel, and J. L. Volakis. Doubly periodic volume-surface integral equation formulation for modelling metamaterials. *IET Microwave, Antennas & Propagation*, 1(1):150–157, 2007.

[85] Jean-Pierre Berenger. A perfectly matched layer for the absorption of electromagnetic waves. *Journal of Computational Physics*, 114:185–200, 1994.

[86] Daniel S. Katz, Eric T. Thiele, and Allen Taflove. Validation and extension to three dimensions of the Berenger PML absorbing boundary condition for FD-TD meshes. *IEEE Microwave and Guided Wave Letters*, 4(8):268–270, 1994.

[87] Weng Cho Chew and William H. Weedon. A 3D perfectly matched medium from modified Maxwell's equations with stretched coordinates. *Microwave and Optical Technology Letters*, 7(13):599–604, 1994.

[88] Carey M. Rappaport. Perfectly matched absorbing boundary conditions based on anisotropic lossy mapping of space. *IEEE Microwave and Guided Wave Letters*, 5(3):90–92, 1995.

[89] Zachary S. Sacks, David M. Kingsland, Robert Lee, and Jin-Fa Lee. A perfectly matched anisotropic absorber for use as an absorbing boundary condition. *IEEE Transactions on Antennas and Propagation*, 43(12):1460–1463, 1995.

[90] R. Mittra and U. Pekel. A new look at the perfectly matched layer (PML) concept for the reflectionless absorption of electromagnetic waves. *IEEE Microwave and Guided Wave Letters*, 5(3):84–86, 1995.

[91] Stephen D. Gedney. An anisotropic perfectly matched layer-absorbing medium for the truncation of FDTD lattices. *IEEE Transactions on Antenna and Propagation*, 44(12):1630–1639, 1996.

[92] C. M. Linton. The Green's function for the two-dimensional Helmholtz equation in periodic domains. *Journal of Engineering Mathematics*, 33:377–402, 1998.

[93] Stephanos Venakides, Mansoor A. Haider, and Vassilis Papanicolaou. Boundary integral calculations of two-dimensional electromagnetic scattering by photonic crystal

Fabry-Perot structures. *SIAM Journal on Applied Mathematics*, 60(5):1686–1706, 2000.

[94] F. Capolino, D. R. Wilton, and W. A. Johnson. Efficient computation of the 3D Green's function for the Helmholtz operator for a linear array of point sources using the Ewald method. *Journal of Computational Physics*, 223:250–261, 2007.

[95] Y. Yan and I. H. Sloan. On integral equations of the first kind with logarithmic kernels. *Journal of Integral Equations and Applications*, 1(4):549–579, 1988.

[96] Kendall E. Atkinson and Ian H. Sloan. The numerical solution of first-kind logarithmic-kernel integral equations on smooth open arcs. *Mathematics of Computation*, 56(193):119–139, 1991.

[97] Roman Chapko and Rainer Kress. On a quadrature method for a logarithmic integral equation of the first kind. In *World Scientific Series in Applicable Analysis: Volume 2. Contributions in Numerical Mathematics*, pages 127–140. 1993.

[98] Rainer Kress. Inverse scattering from an open arc. *Mathematical Methods in the Applied Sciences*, 18:267–293, 1995.

[99] Lars Mönch. On the numerical solution of the direct scattering problem for an open sound-hard arc. *Journal of Computational and Applied Mathematics*, 71:343–356, 1996.

[100] Rainer Kress. Inverse elastic scattering from a crack. *Inverse Problems*, 12:667–684, 1996.

[101] Rainer Kress. On the numerical solution of a hypersingular integral equation in scattering theory. *Journal of Computational and Applied Mathematics*, 61:345–360, 1995.

[102] Rainer Kress and Ian H. Sloan. On the numerical solution of a logarithmic integral equation of the first kind for the Helmholtz equation. *Numerische Mathematik*, 66:199–214, 1993.

[103] Mansoor A. Haider, Stephen P. Shipman, and Stephanos Venakides. Boundary-integral calculations of two-dimensional electromagnetic scattering in infinite photonic crystal slabs: Channel defects and resonances. *SIAM Journal on Applied Mathematics*, 62(6):2129–2148, 2002.

[104] Filippo Capolino, Donald R. Wilton, and William A. Johnson. Efficient computation of the 2-D Green's function for 1-D periodic structures using the Ewald method. *IEEE Transactions on Antennas and Propagation*, 53(9):2977–2984, 2005.

[105] Leung Tsang, Jin Au Kong, Kung-Hau Ding, and Chi On Ao. *Scattering of Electromagnetic Waves: Numerical Simulations*. Wiley-Interscience, 2001.

[106] P. P. Ewald. Die berechnung optischer und elektrostatischer gitterpotentiale. *Annalen der Physik*, 369(3):253–287, 1921. in German.

[107] Vassilis Papanicolaou. Ewald's method revisited: Rapidly convergent series representations of certain Green's functions. *Journal of Computational Analysis and Applications*, 1(1):105–114, 1999.

[108] G. P. M. Poppe and C. M. J. Wijers. Algorithm 680: Evaluation of the complex error function. *ACM Transaction on Mathematical Software*, 16(1):47, 1990.

[109] M. Abramowitz and I. A. Stegun. *Handbook of Mathematical Functions with Formulas, Graphs, and Mathematical Tables*. National Bureau of Standards, 1964.

[110] Philip J. Davis and Philip Rabinowitz. *Methods of Numerical Integration*. Academic Press Inc., second edition, 1984.

[111] Gwynne Evans. *Practical Numerical Integration*. John Wiley & Sons, 1993.

[112] R. D. Graglia. On the numerical integration of the linear shape functions times the 3-D Green's function or its gradient on a plane triangle. *IEEE Transactions on Antennas and Propagation*, 41:1448–1455, 1993.

[113] S. Järvenpää, M. Taskinen, and P. Ylä-Oijala. Singularity extraction technique for integral equation methods with higher order basis functions on plane triangles and tetrahedra. *International Journal for Numerical Methods in Engineering*, 58:1149–1165, 2003.

[114] Lloyd N. Trefethen. Is Gauss quadrature better than Clenshaw-Curtis? *SIAM Review*, 50(1):67–87, 2008.

[115] Theodore J. Rivlin. *An Introduction to the Approximation of Functions*. Blaisdell Publishing Company, 1969.

[116] L. Fejér. Mechanische quadraturen mit positiven cotesschen zahlen. *Mathematische Zeitschrift*, 37:287–309, 1933.

[117] Leopold Fejér. On the infinite sequences arising in the theories of harmonic analysis, of interpolation, and of mechanical quadratures. *Bulletin of the American Mathematical Society*, 39(8):521–534, 1933.

[118] Robert Piessens. Modified Clenshaw-Curtis integration and applications to numerical computation of integral transforms. In P. Keast and G. Fairweather, editors, *Numerical Integrations: Recent Developments, Software and Applications*. Reidel, Dordrecht, 1987.

[119] Ya Yan Lu. A Chebyshev collocation method for computing the eigenvalues of the Laplacian. *International Journal for Numerical Methods in Engineering*, 38:231–243, 1995.

[120] W. Morven Gentleman. Implementing Clenshaw-Curtis quadrature, I methodology and experience. *Communications of the ACM*, (5):337–342, 1972.

[121] W. Morven Gentleman. Implementing Clenshaw-Curtis quadrature, II computing the cosine transformation. *Communications of the ACM*, (5):337–342, 1972.

[122] John P. Boyd. *Chebyshev and Fourier Spectral Methods*. Dover Publications, Inc., second edition, 2001.

[123] Lloyd N. Trefethen. *Spectral Methods in MATLAB*. Society for Industrial and Applied Mathematics, 2000.

[124] J. A. C. Weideman and L. N. Trefethen. The kink phenomenon in Fejér and Clenshaw-Curtis quadrature. *Numerische Mathematik*, 107(4):707–727, 2007.

[125] F. W. J. Olver. Numerical solution of second-order linear difference equations. *Journal of Research of the National Bureau of Standards*, 71B(2/3):111–129, 1967.

[126] P. Van der Cruyssen. A reformulation of Olver's algorithm for the numerical solution of second-order linear difference equations. *Numerische Mathematik*, 32:159–166, 1979.

[127] Charles Van Loan. *Computational Frameworks for the Fast Fourier Transform*. Society for Industrial and Applied Mathematics, 1992.

[128] Lloyd N. Trefethen and David Bau III. *Numerical Linear Algebra*. Society for Industrial and Applied Mathematics, 1997.

[129] U. Saad. *Interative Methods for Sparse Linear Systems*. Society for Industrial and Applied Mathematics, second edition, 2003.

[130] Tony F. Chan. An optimal circulant preconditioner for Toeplitz systems. *SIAM journal on scientific and statistical computing*, 9(4):766–771, 1988.

[131] Tony F. Chan and Julia A. Olkin. Circulant preconditioners for Toeplitz-block matrices. In *SIAM Conference on Linear Algebra in Signals, Systems, and Control*, pages 89–101, 1990.

[132] Harland G. Tompkins and William A. McGahan. *Spectroscopic Ellipsometry and Reflectometry: A User's Guide*. John Wiley and Sons, 1999.

[133] Helmuth Späth. *Two Dimensional Spline Interpolation Algorithms*. A K Peters, 1995.

[134] Andrew R. Conn, Nicholas I. M. Gould, and Philippe L. Toint. *Trust-Region Methods*. Society for Industrial Mathematics, 1987.

[135] J. E. Dennis Jr. and Robert B. Schnabel. *Numerical Methods for Unconstrained Optimization and Nonlinear Equations*. Society for Industrial and Applied Mathematics, 1996.

[136] S. M. Rao, D. R. Wilton, and A. W. Glisson. Electromagnetic scattering by surfaces of arbitrary shape. *IEEE Transactions on Antennas and Propagation*, pages 409–418, 1982.

[137] D. H. Schaubert, D. R. Wilton, and A. W. Glisson. A tetrahedral modeling method for electromagnetic scattering by arbitrary shaped inhomogeneous dielectric bodies. *IEEE Transaction on Antennas and Propagation*, pages 77–85, 1984.

[138] B. C. Usner, K. Sertel, M. A. Carr, and J. L. Volakis. Genrealized volume-surface integral equation for modeling inhomogeneous within high contrast composite structures. *IEEE Transactions on Antennas and Propagation*, pages 68–75, 2006.

[139] S. M. Rao, A. W. Glisson, D. R. Wilton, and B. S. Vidula. A simple numerical solution procedure for statics problems involving arbitrary-shaped surfaces. *IEEE Transactions on Antennas and Propagation*, 27:604–608, 1979.

[140] M. G. Duffy. Quadrature over a pyramid or cube of integrals with a singularity at a vertex. *SIAM Journal on Numerical Analysis*, 19:1260–1262, 1982.

[141] S. V. Yesantharao. EMPACK-a software toolbox of potential integrals for computational electromagnetics. Master's thesis, University of Houston, 1989.

[142] L. Knockaert. A general Gauss theorem for evaluating singular integrals over polyhedral domains. *Electromagnetics*, 11:269–280, 1991.

[143] K. Hayami. *A Projection Transformation Method for Nearly Singular Surface Boundary Element Integrals*. New York: Springer-Verlag, 1992.

[144] Luca Rossi and Peter J. Cullen. On the fully numerical evaluation of the linear-shape function times the 3-D Green's function on a plane triangle. *IEEE Transactions on Microwave Theory and Techniques*, 47(4), 1999.

[145] Z. Zhu, J. Huang, B. Song, and J. White. Improving the robustness of a surface integral formulation for wideband impedance extraction of 3D structures. In *Proceedings of ICCAD*, pages 592–597, 2001.

[146] S. Chakraborty and V. Jandhyala. Evaluation of Green's function integrals in conducting media. *IEEE Transactions on Antennas and Propagation*, pages 3357–3363, 2004.

[147] M. A. Khayat and D. R. Wilton. Numerical evaluation of singular and near-singular potential integrals. *IEEE Transactions on Antennas and Propagation*, 53:3180–3190, 2005.

[148] Shih-Hsien Kuo. *A Meshless, High-Order Integral Equation Method for Smooth Surfaces, with Application to Biomolecular Electrostatics*. PhD thesis, Massachusetts Institute of Technology, 2006.

[149] W. H. Tang and S. D. Gedney. An efficient evaluation of near singular surface integrals via the Khayat-Wilton transform. *Microwave and Optical Technology Letters*, 48(8):1583–1586, 2006.

[150] Jung Hoon Lee and Jacob White. Complex-domain mapping for evaluating troublesome integrals in fast full-wave integral equation solvers. In *IEEE MTT-S International Microwave Symposium Digest*, pages THP1B–01, Atlanta, Georgia, June 2008.

[151] O. D. Kellogg. *Foundations of Potential Theory*. Dover Publications, 1954.

[152] T. W. Tee and L. N. Trefethen. A rational spectral collocation method with adaptively transformed Chebyshev grid points. *SIAM Journal on Scientific Computing*, 28(5):1798–1811, 2006.

[153] Nicholas Hale and Lloyd N. Trefethen. New quadrature formulas from conformal maps. *SIAM Journal of Numerical Analysis*, 46(2):930–948, 2008.

[154] Ronald Cools and Philip Rabinowitz. Monomial cubature rules since "Stroud": a compilation. *Journal of Computational and Applied Mathematics*, 48:309–326, 1993.

[155] Ronald Cools. An encyclopaedia of cubature formulas. *Journal of Complexity*, 19:445–453, 2003.

[156] Jaydeep Porter Bardhan. *Efficient Numerical Algorithms for Surface Formulations of Mathematical Models for Biomolecule Analysis and Design*. PhD thesis, Massachusetts Institute of Technology, 2006.

[157] David Joe Willis. *An Unsteady, Accelerated, High Order Panel Method with Vortex Particle Wakes*. PhD thesis, Massachusetts Institute of Technology, 2006.

[158] Jaydeep P. Bardhan, Michael D. Altman, David J. Willis, Shaun M. Lippow, Bruce Tidor, and Jacob K. White. Numerical integration techniques for curved-element discretizations of molecule-solvent interfaces. *The Journal of Chemical Physics*, 127:014701–1–014701–18, 2007.

[159] Neil V Budko and Rob F Remis. Electromagnetic inversion using a reduced-order three-dimensional homogeneous model. *Inverse Problems*, 20:S17–S26, 2004.

[160] R. F. Remis. An effective inversion method based on the Padé via Lanczos process. In *Progress in Electromagnetics Research Symposium*, pages 206–209, Cambridge, Massachusetts, March 2006.

[161] Vladimir Druskin and Mikhail Zaslavsky. On combining model reduction and Gauss-Newton algorithms for inverse partial differential equation problems. *Inverse Problems*, 23:1599–1610, 2007.

[162] David Colton and Peter Monk. A novel method for solving the inverse scattering problem for time-harmonic acoustic waves in the resonance region. *SIAM journal on applied mathematics*, 45(6):1039–1053, 1985.

[163] David Colton and Peter Monk. A novel method for solving the inverse scattering problem for time-harmonic acoustic waves in the resonance region II. *SIAM journal on applied mathematics*, 46(3):506–523, 1986.

[164] David Colton and Peter Monk. The numerical solution of the three-dimensional inverse scattering problem for time harmonic acoustic waves. *SIAM journal on scientific and statistical computing*, 8(3):278–291, 1987.

[165] Andreas Kirsch and Rainer Kress. A numerical method for an inverse scattering problem. In H. W. Engl and C. W. Groetsch, editors, *Inverse and Ill-Posed Problems*. Academic Press, Inc., 1987.

[166] A. Kirsch and R. Kress. An optimization method in inverse acoustic scattering (invited contribution). In C. A. Brebbia, W. L. Wendland, and G. Kuhn, editors, *Boundary Elements IX*. Springer-Verlag, 1987.

[167] A. Kirsch, R. Kress, P. Monk, and A. Zinn. Two methods for solving the inverse acoustic scattering problem. *Inverse Problems*, 4:749–770, 1988.

[168] Luciano Misici and Francesco Zirilli. Three-dimensional inverse obstacle scattering for time harmonic acoustic waves: A numerical method. *SIAM journal on scientific computing*, 15(5):1174–1189, 1994.

[169] Jung Hoon Lee and Dimitri. Accelerated optical topography inspection using parameterized model order reduction. In *IEEE MTT-S International Microwave Symposium Digest*, pages 1771–1774, Long Beach, California, June 2005.

[170] D. S. Weile, E. Michielssen, E. Grimme, and K. Gallivan. A method for generating rational interpolant reduced order models of two-parameter linear systems. *Applied Mathematics Letters*, 12:93–102, 1999.

[171] Pavan Gunupudi and Michel Nakhla. Multi-dimensional model reduction of VLSI interconnects. In *Proceedings of IEEE Custom Integrated Circuits Conference*, pages 499–502, Orlando, Florida, May 2000.

[172] Luca Daniel, Chin Siong Ong, Sok Chay Low, Kwok Hong Lee, and Jacob White. Geometrically parameterized interconnect performance models for interconnect synthesis. In *Proceedings of the International Symposium on Physical Design*, San Diago, California, 2002.

[173] Pavan Gunupudi, Roni Khazaka, and Michel Nakhla. Analysis of transmission line circuits using multidimensional model reduction techniques. *IEEE Transactions on Advanced Packaging*, 25(2):174–180, 2002.

[174] L. Daniel and J. White. Automatic generation of geometrically parameterized reduced order models for integrated spiral RF-inductors. In *Proceedings of Behavioral Modeling and Simulation*, San Jose, California, 2003.

[175] Pavan K. Gunupudi, Roni Khazaka, Michel S. Nakhla, Tom Smy, and Dritan Celo. Passive parameterization time-domain macromodels for high-speed transmission-line networks. *IEEE Transactions on Microwave Theory and Techniques*, 51(12):2347–2354, 2003.

[176] L. Daniel, O. C. Siong, L. S. Chay, K. H. Lee, and J. White. A multiparameter moment matching model reduction approach for generating geometrically parameterized interconnect performance models. *IEEE Transactions on Computer Aided Design*, 23(5):678–693, May 2004.

[177] K. Gallivan, E. Grimme, and P. Van Dooren. Asymptotic Waveform Evaluation via a Lanczos Method. *Applied Mathematics Letters*, 7(5):75–80, 1994.

[178] P. Feldmann and R. W. Freund. Efficient linear circuit analysis by Padé approximation via the Lanczos process. *IEEE Trans. on Computer-Aided Design*, 14(5):639–649, 1995.

[179] E. Grimme. *Krylov Projection Methods for Model Reduction.* PhD thesis, Coordinated-Science Laboratory, University of Illinois at Urbana-Champaign, Urbana-Champaign, IL, 1997.

[180] L. T. Pillage and R. A. Rohrer. Asymptotic waveform evaluation for timing analysis. 9(4):352–366, 1990.

[181] C. P. Coelho, J. R. Phillips, and L. M. Silveira. Robust rational function approximation algorithm for model generation. In *Proceedings of the ACM/IEEE Design Automation Conference*, New Orleans, Louisiana, 1999.

[182] Kin Cheong Sou, Alexandre Megretski, and Luca Daniel. A quasi-convex optimization approach to parameterized model order reduction. In *Proceedings of the Design Automation Conference*, pages 933–938, Anaheim, California, June 2005.

[183] Kin Cheong Sou, Alexandre Megretski, and Luca Daniel. A quasi-convex optimization approach to parameterized model order reduction. *IEEE Transactions on Computer-Aided Design of Integrated Circuits and Systems*, 27(3):456–469, 2008.

[184] John Allgair, Dave Benoit, Rob Hershey, Lloyd C. Litt, Ibrahim Abduihalim, Bill Braymer, Michael Faeyrman, John C. Robinson, Umar Whitney, Yiping Xu, Piotr Zalicki, and Joel Seligson. Manufacturing considerations for implementation of scatterometry for process monitoring. In *Proceedings of SPIE*, volume 3998, pages 125–134, 2000.

[185] Zhenhai Zhu and Joel Phillips. Random sampling of moment graph: A stochastic Krylov-reduction algorithm. In *Proceedings of the Conference on Design, Automation and Test in Europe*, pages 1502–1507, Nice, France, April 2007.

[186] Peng Li, Frank Liu, Xin Li, Lawrence T. Pileggi, and Sani R. Nassif. Modeling interconnect variability using efficient parametric model order reduction. In *Proceedings of the Design, Automation and Test in Europe Conference and Exhibition*, pages 958–963, Münich, Germany, March 2007.

[187] Thomas J. Klemas, Luca Daniel, and Jacob K. White. Segregation by primary phase factors: a full-wave algorithm for model order reduction. *Proceedings of the Design Automation Conference*, pages 943–946, June 2005.

[188] Volker Barthelmann, Erich Novak, and Klaus Ritter. High dimensional polynomial interpolation on sparse grids. *Advances in Computational Mathematics*, 12:273–288, 2000.

[189] Rainer Kress. Boundary integral equations in time-harmonic acoustic scattering. *Mathematical and Computer Modelling*, 15(3-5):229–243, 1991.

[190] J. W. Strutt Rayleigh. On the dispersal of light by a dielectric cylinder. *The London, Edinburgh and Dublin philosophical magazine and journal of science*, 36:365–376, 1918.

[191] Philip M. Morse and K. Uno Ingard. *Theoretical Acoustics*. McGraw-Hill Book Company, 1968.

[192] G. B. Whitham. *Linear and Nonlinear Waves*. John Wiley and Sons, Inc., 1999.